

MODELLING, ANALYSIS AND CONTROL OF NON-ISOLATED MULTI PORT DC-DC BOOST CONVERTER

A DISSERTATION
SUBMITTED IN PARTIAL FULFILLMENT OF THE REQUIREMENTS
FOR THE AWARD OF THE DEGREE
OF

MASTER OF TECHNOLOGY
IN
CONTROL & INSTRUMENTATION

Submitted by:

SHREYANSH UPADHYAYA

2K17/C&I/17

Under the supervision of

PROF. DHEERAJ JOSHI



DEPARTMENT OF ELECTRICAL ENGINEERING
DELHI TECHNOLOGICAL UNIVERSITY

(Formerly Delhi College of Engineering)
Bawana Road, Delhi-110042

2019

DEPARTMENT OF ELECTRICAL ENGINEERING
DELHI TECHNOLOGICAL UNIVERSITY
(Formerly Delhi College of Engineering)
Bawana Road, Delhi-110042

CANDIDATE'S DECLARATION

I, Shreyansh Upadhyaya, Roll No. 2K17/C&I/17 student of M.Tech. (Control & Instrumentation), hereby declare that the dissertation titled “Modelling, Analysis and Control of Non-Isolated Multiport DC-DC Boost Converter” which is submitted by me to the Department of Electrical Engineering Department, Delhi Technological University, Delhi in partial fulfillment of the requirement for the award of the degree of Master of Technology, is original and not copied from any source without proper citation. This work has not previously formed the basis for the award of any Degree, Diploma Associateship, Fellowship or other similar title or recognition.

Place: Delhi

(SHREYANSH UPADHYAYA)

Date:

DEPARTMENT OF ELECTRICAL ENGINEERING
DELHI TECHNOLOGICAL UNIVERSITY
(Formerly Delhi College of Engineering)
Bawana Road, Delhi-110042

CERTIFICATE

This is to certify that this dissertation report entitled “**Modelling, Analysis and Control of Non-Isolated Multiport DC-DC Boost Converter**” being submitted by **Shreyansh Upadhyaya (Roll No. 2K17/C&I/17)** under the supervision of **Prof. Dheeraj Joshi**, Electrical Engineering Department, Delhi Technological University, New Delhi in partial fulfillment of the requirement for the award of the degree of Master of Technology.

Place: Delhi

(Dr. DHEERAJ JOSHI)

Date:

SUPERVISOR

Professor

Electrical Engineering Department

Delhi Technological University

Delhi-110042

ACKNOWLEDGEMENT

I would like to take this opportunity to extend my gratitude to all the loyal hands for helping me out during my assignment. To begin with, I would like to express my deep and sincere gratitude to my project supervisor, **Prof. Dheeraj Joshi**, Department of Electrical Engineering, Delhi Technological University, for giving me the opportunity to do project and providing invaluable guidance throughout this project. His dynamism, vision, sincerity and motivation have deeply inspired me. He has taught me the methodology to carry out the project and to present the project work as clearly as possible. It was a great privilege and honor to work and study under his guidance. I am extremely grateful for what he has offered me. I would also like to thank him for his friendship, empathy, and great sense of humor. Without the wise advice and able guidance, it would have been impossible to complete the dissertation in this manner.

I would like to thank the staff members (**Ms. Renu and Ms. Vandana**) of **Power Electronics Lab** for co-operating with me and providing me with the best possible working environment for the assignment. I would like to extend my thanks to **Mr. Kailash Rana**, PhD Scholar, Delhi Technological University, without the help of whom the dissertation would not have been completed. I would also like to thank all my friends for their help, moral support and encouragement provided by them during the completion of the dissertation work.

I am extremely grateful to my parents and family members for their love, prayers, caring and sacrifices for educating and preparing me for my future.

SHREYASH UPADHYAYA
M.Tech. (Control & Instrumentation)
Roll No. 2K17/C&I/17

ABSTRACT

A non-isolated multiport DC-DC boost converter is presented in this dissertation work. This converter has various applications related to hybridizing sustainable energy sources in electric vehicles. By integrating two or more energy sources, advantages of various sources are achievable. In this converter, two input sources flexibly distribute their power to the two output load resistances. Also, using this converter, charging and discharging of battery sources is possible and controllable. The converter has two different output voltage levels which makes it easier for integrating with multilevel inverters. For designing of controllers of the presented converter system, small-signal model using each state is evaluated and bode plots for stability analysis are extracted. The validity of the non-isolated multiport DC-DC boost converter and its performance is verified by simulated and experimental results for battery discharging mode. Various control algorithms viz. PI, PID, FOPID and ANN are implemented using ATmega328p (ARDUINO UNO) microcontroller. MATLAB/Simulink platform has been utilized for simulation purpose.

CONTENTS

Candidate's Declaration	i
Certificate	ii
Acknowledgement	iii
Abstract	iv
Contents	v
List of Figures	viii
List of Tables	xii
List of Symbols and Abbreviations	xiii
CHAPTER 1 Introduction	1
1.1 Motivation	1
1.2 Literature Review	4
1.3 Research Objectives	7
1.4 Composition of the dissertation	7
CHAPTER 2 Non-Isolated Multiport DC-DC Boost Converter Topology	9
2.1 Overview	9
2.2 Multiport Converter Topology	9
2.3 Analysis of the Multiport Boost Converter	12
2.3.1 Single Input Single Output (SISO)	12
2.3.2 Single Input Multiple Output (SIMO)	13
2.3.3 Multiple Input Multiple Output (MIMO)	13
2.3.3.1 First Operation Mode (Battery Discharging Mode)	14
2.3.3.2 Second Operation Mode (Battery Charging Mode)	17
CHAPTER 3 Dynamic Modelling of Non-Isolated Multiport DC-DC Boost Converter	21
3.1 Dynamic Modelling and Analysis	21
3.1.1 Dynamic Modelling of Battery Discharging Mode	21
3.1.2 Dynamic Modelling of Battery Charging Mode	25

CHAPTER 4	Control Strategies for Non-Isolated Multiport	29
	DC-DC Boost Converter	
4.1	Introduction	29
4.2	Stability Analysis of Multiport Converter	29
4.3	PI Controller	32
4.4	PID Controller	33
4.5	FOPID Controller	34
4.6	ANN Controller	36
4.7	Summary of the Chapter	38
CHAPTER 5	Results and Discussions	39
5.1	Introduction	39
5.2	Open Loop system	39
5.2.1	Performance of Open Loop on Input Variations	39
5.2.2	Performance of Open Loop on Load Variations	41
5.3	Closed Loop System	47
5.3.1	Performance of PI controller on Input Variations	47
5.3.2	Performance of PI controller on Load Variations	48
5.3.3	Performance of PID controller on Input Variations	52
5.3.4	Performance of PID controller on Load Variations	53
5.3.5	Performance of FOPID controller on Input Variations	57
5.3.6	Performance of FOPID controller on Load Variations	58
5.3.7	Performance of ANN controller on Input Variations	62
5.3.8	Performance of ANN controller on Load Variations	63
5.4	Comparative Analysis	67
5.4.1	Performance of various control algorithm subjected to input variations	67
5.4.2	Performance of various control algorithm subjected to load variations	72
5.4.3	Performance of simulated output voltages subjected to various control algorithms	79

5.4.4	Performance of simulated output voltages with varying control parameters	80
5.4.5	Performance of experimental output voltages subjected to various control algorithms	81
5.4.6	Performance of power and efficiency for multiport converter	82
5.5	Summary of the Chapter	84
CHAPTER 6 Conclusion and Future Scope		85
6.1	Conclusion	85
6.2	Future scope	86
References		
Appendices		

LIST OF FIGURES

No.	Title	Pg. No.
Figure 1.1	Example of residential low voltage DC power distribution system	1
Figure 1.2	Conventional DC distribution system with multiple SISO converters	2
Figure 1.3	Proposed DC distribution system with MIMO converter	3
Figure 2.1	Multiport converter structure	10
Figure 2.2	Single input single output converter structure	11
Figure 2.3	Single input Multiple output converter structure	11
Figure 2.4	Multiple input multiple output converter structure	12
Figure 2.5	Steady-state waveforms of MIMO converter in battery discharging mode	14
Figure 2.6	Equivalent circuit of battery discharging mode during (a) switching state 1, (b) switching state 2, (c) switching state 3, and (d) switching state 4	17
Figure 2.7	Steady-state waveforms of MIMO converter in battery charging mode	18
Figure 2.8	Equivalent circuit of battery charging mode during (a) switching state 1, (b) switching state 2, (c) switching state 3, and (d) switching state 4	20
Figure 3.1	Control block diagram of MIMO converter for (a) battery discharging mode, and (b) battery charging mode	25
Figure 4.1	Simulated bode plot of $g_{11}(s)$	30
Figure 4.2	Simulated bode plot of $g_{22}(s)$	31
Figure 4.3	Simulated bode plot of $g_{33}(s)$	32
Figure 4.4	PI Controller configuration	33
Figure 4.5	PID Controller configuration	34
Figure 4.6	Flowchart for PI, PID and FOPID control implementation	35
Figure 4.7	Basic ANN implementation structure	36
Figure 4.8	Flowchart for ANN control implementation	37
Figure 5.1	Simulated vs experimental results of open loop system for (a) V_T (b) V_{O1} (c) V_T and (d) V_{O1} with input voltage variations keeping V_{in2} as 12V and 24V respectively	40

Figure 5.2	Simulated vs experimental results of open loop system for (a) V_T (b) V_{01} (c) V_T (d) V_{01} (e) V_T and (f) V_{01} with load resistance variations	42
Figure 5.2.1	Simulated results for open loop of (a) Output Voltages (V_T and V_{01}) (b) Input Current I_{in1} (c) Input Current I_{in2} and (d) Inductor Current I_L	44
Figure 5.2.2	Experimental results for open loop of (a) Output Voltages (V_T and V_{01}) (b) Input Current I_{in1} (c) Input Current I_{in2} and (d) Inductor Current I_L	46
Figure 5.3	Simulated vs experimental results of closed loop PI control for (a) V_T (b) V_{01} (c) V_T and (d) V_{01} with input voltage variations keeping V_{in2} as 12V and 24V respectively	48
Figure 5.4	Simulated vs experimental results of closed loop PI control for (a) V_T (b) V_{01} (c) V_T (d) V_{01} (e) V_T and (f) V_{01} with load resistance variations	50
Figure 5.4.1	Output Voltage (V_T & V_{01}) plot for (a) simulated and (b) experimental results	51
Figure 5.5	Simulated vs experimental results of closed loop PID control for (a) V_T (b) V_{01} (c) V_T and (d) V_{01} with input voltage variations keeping V_{in2} as 12V and 24V respectively	52
Figure 5.6	Simulated vs experimental results of closed loop PID control for (a) V_T (b) V_{01} (c) V_T (d) V_{01} (e) V_T and (f) V_{01} with load resistance variations	55
Figure 5.6.1	Output Voltage (V_T & V_{01}) plot for (a) simulated and (b) experimental results	56
Figure 5.7	Simulated vs experimental results of closed loop FOPID control for (a) V_T (b) V_{01} (c) V_T and (d) V_{01} with input voltage variations keeping V_{in2} as 12V and 24V respectively	57
Figure 5.8	Simulated vs experimental results of closed loop FOPID control for (a) V_T (b) V_{01} (c) V_T (d) V_{01} (e) V_T and (f) V_{01} with load resistance variations	60
Figure 5.8.1	Output Voltage (V_T & V_{01}) plot for (a) simulated and (b) experimental results	61
Figure 5.9	Simulated vs experimental results of closed loop ANN control for (a) V_T (b) V_{01} (c) V_T and (d) V_{01} with input voltage variations	62

Figure 5.10	Simulated vs experimental results of closed loop ANN control for (a) V_T (b) V_{01} (c) V_T (d) V_{01} (e) V_T and (f) V_{01} with input voltage variations keeping V_{in2} as 12V and 24V respectively	65
Figure 5.10.1	Output Voltage (V_T & V_{01}) plot for (a) simulated and (b) experimental results.	66
Figure 5.11	Simulated output voltage vs input voltage (V_{in1}) variations keeping 12V as V_{in2}	67
Figure 5.12	Experimental output voltage vs input voltage (V_{in1}) variations keeping 12V as V_{in2}	68
Figure 5.13	Simulated output voltage vs input voltage (V_{in1}) variations keeping 24V as V_{in2}	69
Figure 5.14	Experimental output voltage vs input voltage (V_{in1}) variations keeping 24V as V_{in2}	69
Figure 5.15	Simulated output voltage (V_{01}) vs input voltage (V_{in1}) variations keeping 12V as V_{in2}	70
Figure 5.16	Experimental output voltage (V_{01}) vs input voltage (V_{in1}) variations keeping 12V as V_{in2}	71
Figure 5.17	Simulated output voltage (V_{01}) vs input voltage (V_{in1}) variations keeping 24V as V_{in2}	72
Figure 5.18	Experimental output voltage (V_{01}) vs input voltage (V_{in1}) variations keeping 24V as V_{in2}	72
Figure 5.19	Simulated output voltage vs load (R_1) variations	73
Figure 5.20	Experimental output voltage vs load (R_1) variations	73
Figure 5.21	Simulated output voltage vs load (R_2) variations	74
Figure 5.22	Experimental output voltage vs load (R_2) variations	74
Figure 5.23	Simulated output voltage vs load (R_1 and R_2) variations	75
Figure 5.24	Experimental output voltage vs load (R_1 and R_2) variations	75
Figure 5.25	Simulated output voltage (V_{01}) vs load (R_1) variations	76
Figure 5.26	Experimental output voltage (V_{01}) vs load (R_1) variations	76
Figure 5.27	Simulated output voltage (V_{01}) vs load (R_2) variations	77
Figure 5.28	Experimental output voltage (V_{01}) vs load (R_2) variations	77
Figure 5.29	Simulated output voltage (V_{01}) vs load (R_1 and R_2) variations	78
Figure 5.30	Experimental output voltage (V_{01}) vs load (R_1 and R_2) variations	78
















Figure 5.31	Simulated total output voltage waveform	79
Figure 5.32	Simulated total output voltage waveform with load switching	79
Figure 5.33	Simulated total output voltage waveform with varying PI controller parameters	80
Figure 5.34	Simulated total output voltage waveform with varying PID controller parameters	80
Figure 5.35	Experimental output voltage waveforms of (a) PI controller (b) PID controller (c) FOPID controller (d) ANN controller	81
Figure 5.36	Comparison of (a) input power (b) output power and (c) efficiency under various control strategies with input voltage (V_{in1}) variations keeping V_{in2} as 24V and load resistances as 100Ω each	83

LIST OF TABLES

No.	Title	Pg. No.
Table 4.1	Simulation and Experimental parameters	30
Table 5.1	Comparison of results under different control strategies for MIMO converter	84

LIST OF SYMBOLS AND ABBREVIATIONS

PV	Photo Voltaic
FC	Fuel Cell
DC	Direct Current
LED	Light Emitting Diode
SISO	Single Input Single Output
MIMO	Multiple Input Multiple Output
EV	Electric Vehicle
ESS	Energy Storage System
SC	Super Capacitor
AC	Alternating Current
PVSC	Pulsating Voltage Source Converters
PCSC	Pulsating Current Source Converters
PCB	Printed Circuit Board
PI	Proportional Integral
PID	Proportional Integral Derivative
FOPID	Fractional Order Proportional Integral Derivative
ANN	Artificial Neural Network
SMPS	Switched Mode Power Supply
SIMO	Single Input Multiple Output
HEV	Hybrid Electric Vehicle
DCM	Discontinuous Conduction Mode
MATLAB	Matrix Laboratory
L	Inductor
C_1, C_2	Capacitors
D_0, D_1, D_2, D_3	Diodes
S_1, S_2, S_3, S_4	Switches
R_1, R_2	Resistances
V_{in1}, V_{in2}	Average Input Voltages
V_{in1}, V_{in2}	Instantaneous Input Voltages
V_{01}, V_{02}, V_T	Average Output Voltages

V_{01}, V_{02}, V_T	Instantaneous Output Voltages
I_L	Average Inductor Current
i_L	Instantaneous Inductor Current
I_{in1}, I_{in2}, I_B	Average Input Currents
i_{in1}, i_{in2}, i_B	Instantaneous Input Currents
I_{01}, I_{02}	Average Output Currents
i_{01}, i_{02}	Instantaneous Output Currents
d_1, d_2, d_3, d_4	Duty Cycles
g_{11}, g_{22}, g_{33}	Transfer Functions
K_P, K_I, K_D	Controller Parameters
$e(t)$	Error Signal
f_s	Switching Frequency
T	Switching Period
I_{C1}, I_{C2}	Capacitor Charging Current
V	Volts
A	Ampere
W	Watts
Ω	Ohm
 $V_T E$	Experimental Total Output Voltage
 $V_T S$	Simulated Total Output Voltage
 $V_{01} E$	Experimental Output Voltage
 $V_{01} S$	Simulated Output Voltage
 $V_T S OL$	Simulated Open Loop Total Output Voltage
 $V_T E OL$	Experimental Open Loop Total Output Voltage
 $V_{01} S OL$	Simulated Open Loop Output Voltage
 $V_{01} E OL$	Experimental Open Loop Output Voltage
 $P_{in} OL$	Input Power of Open Loop
 $P_{out} OL$	Output Power of Open Loop
 $Eff OL$	Efficiency of Open Loop
 $V_T S PI$	Simulated PI Controlled Total Output Voltage
 $V_T E PI$	Experimental PI Controlled Total Output Voltage
 $V_{01} S PI$	Simulated PI Controlled Output Voltage
 $V_{01} E PI$	Experimental PI Controlled Output Voltage

—▲— Pin PI	Input Power using PI Controller
—▲— Pout PI	Output Power using PI Controller
—▲— Eff PI	Efficiency using PI Controller
—◆— VT S PID	Simulated PID Controlled Total Output Voltage
—◆— VT E PID	Experimental PID Controlled Total Output Voltage
—◆— V01 S PID	Simulated PID Controlled Output Voltage
—◆— V01 E PID	Experimental PID Controlled Output Voltage
—◆— Pin PID	Input Power using PID Controller
—◆— Pout PID	Output Power using PID Controller
—◆— Eff PID	Efficiency using PID Controller
—✕— VT S FOPID	Simulated FOPID Controlled Total Output Voltage
—✕— VT E FOPID	Experimental FOPID Controlled Total Output Voltage
—✕— V01 S FOPID	Simulated FOPID Controlled Output Voltage
—✕— V01 E FOPID	Experimental FOPID Controlled Output Voltage
—✕— Pin FOPID	Input Power using FOPID Controller
—✕— Pout FOPID	Output Power using FOPID Controller
—✕— Eff FOPID	Efficiency using FOPID Controller
—●— VT S ANN	Simulated ANN Controlled Total Output Voltage
—●— VT E ANN	Experimental ANN Controlled Total Output Voltage
—●— V01 S ANN	Simulated ANN Controlled Output Voltage
—●— V01 E ANN	Experimental ANN Controlled Output Voltage
—●— Pin ANN	Input Power using ANN Controller
—●— Pout ANN	Output Power using ANN Controller
—●— Eff ANN	Efficiency using ANN Controller

This chapter discusses multiport DC-DC converters, which plays a major role in applications like hybridizing alternate energy sources in electric vehicles and distributed generation from microgrids. This chapter also includes a description of dissertation, aim and objectives.

1.1 Motivation

Usage of renewable energy sources on various electronic loads has attracted various industrial and commercial applications due to their virtues of least pollution and sustainability. Since these energy resources are variable, storing them is necessary for backup. In order to improve supply security and lower pollution levels, an alternate hybrid power source is needed. As well multiple sources are needed for optimal power dispatch. Since many commercial or residential devices often need power supply with different voltage levels, therefore the need of power circuits for distributing power to various consumer loads with different voltage levels motivates the development of converter circuits to provide multiple voltage levels.

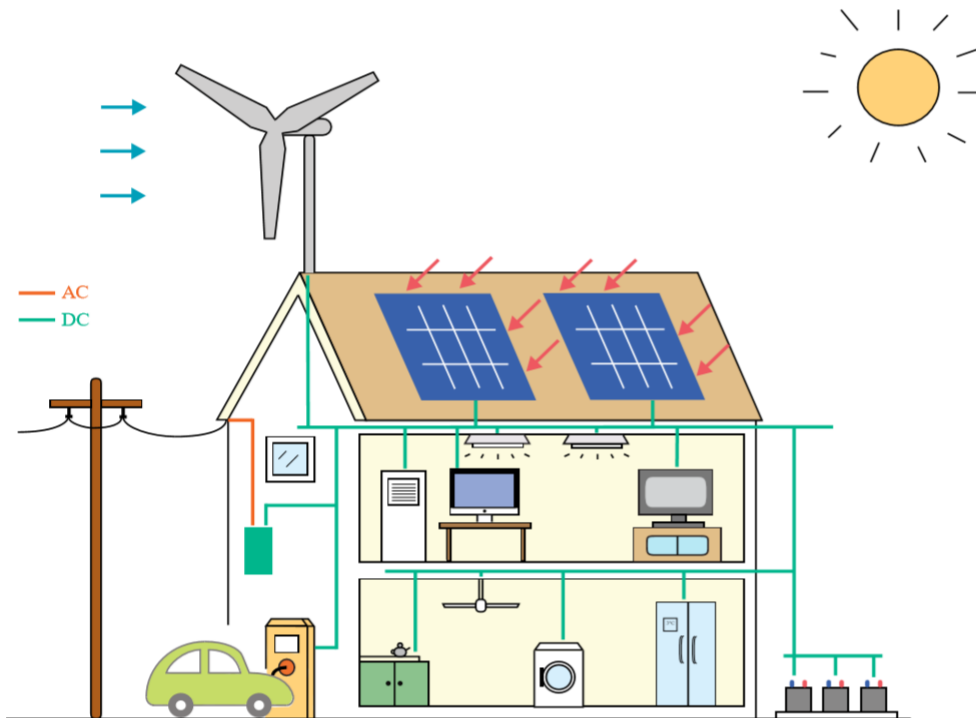


Fig. 1.1 Example of residential low voltage DC power distribution system[30]

Various sources other than PVs and FCs generates DC voltage, and numerous consumption loads are available nowadays which uses DC as input supply i.e. portable devices, LEDs, music players, etc. Therefore, DC system can become a medium of interaction between different energy sources, advanced electronic loads and storage units for simplicity and efficiency. Figure 1.1 shows a concept about how DC power distribution occurs for future applications where alternate renewable sources are interfaced and storage batteries or other devices are installed to provide power to different loads. Conceptually multiple ports can be formed using two approaches. Traditionally, single-input single-output (SISO) converters are used in parallel at a common DC bus to exchange power (fig. 1.2). In SISO systems, converters are controlled independently and each separate conversion stages are employed for every source and load. These systems are prevalent in recent developments but complex configuration results in larger modules and higher costs. In these if complexity increases, performance may degrade. Thus, a prominent solution is multiple-input, multiple-output (MIMO) converter. The complex configurations can be replaced by simplified set-up as in fig. 1.3. Integration of MIMO systems with sources and loads provides compact packaging, relatively easier control, and simultaneous power management and voltage regulation.

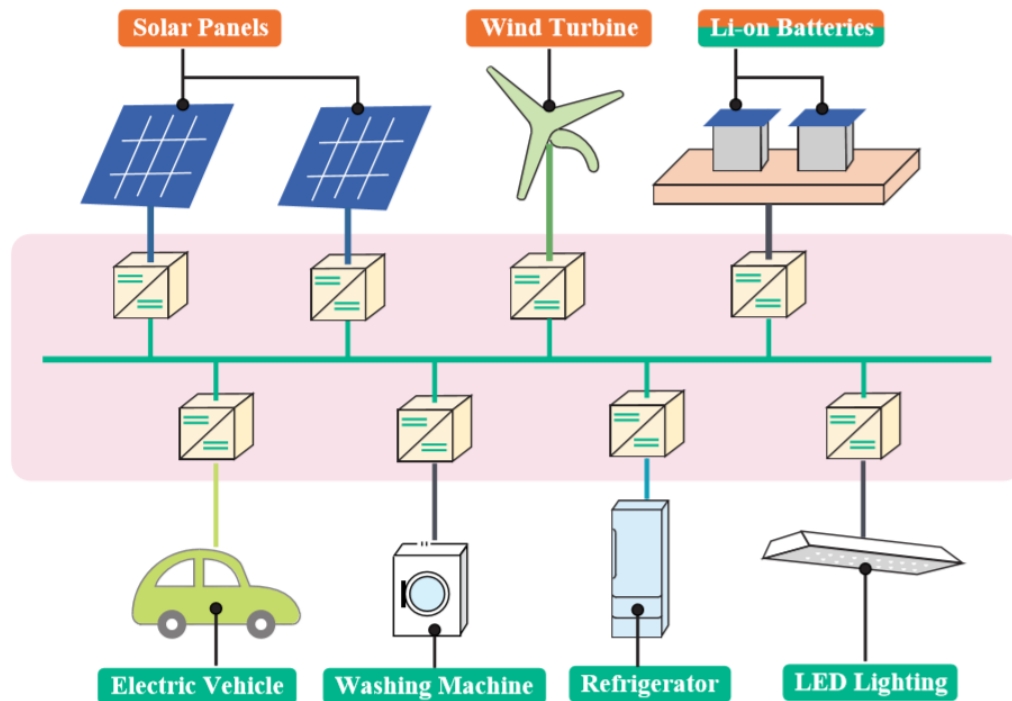


Fig. 1.2 Conventional DC distribution system with multiple SISO converters[30]

Development of MIMO converters had come into picture in most recent research, multiple-input single-output (MISO) converters and single-input multiple-output (SIMO) converters have been well researched. MISO architecture is cost-effective and modular tech for including more than one source. MISO converters find its applications in PV-utility systems, PV-wind systems, renewable generation system with battery storage and hybrid EVs. SIMO configurations are efficient power suppliers for several loads. SIMO converters find its applications in portable and electronic devices, fuel cell generation systems, and multilevel inverters.

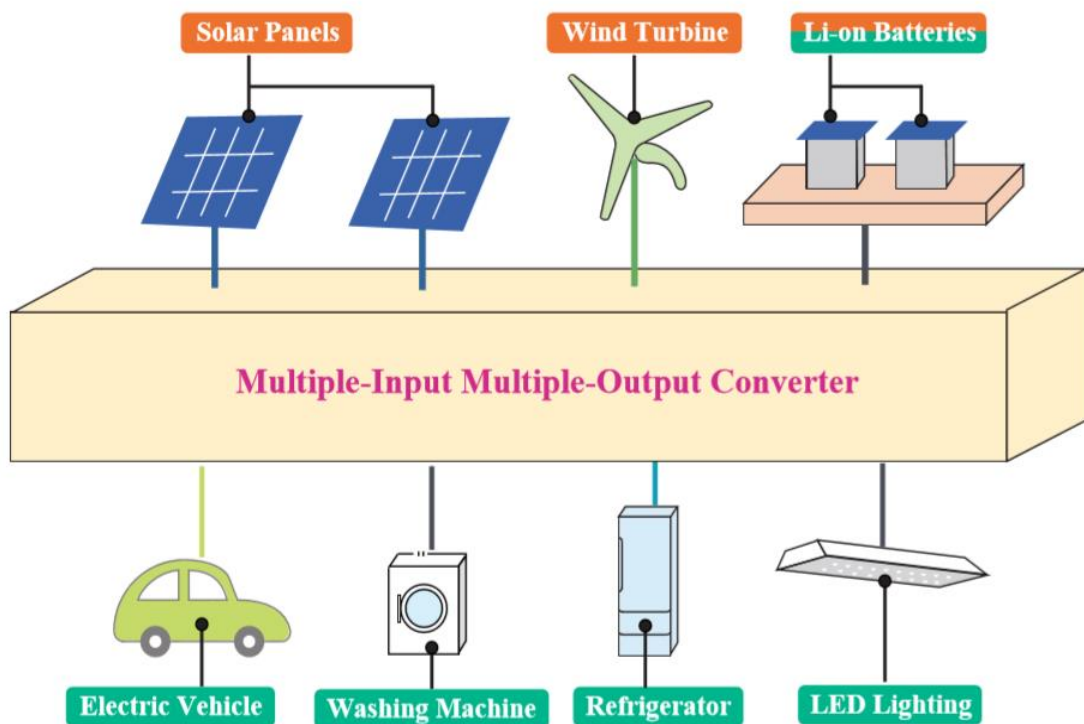


Fig. 1.3 Proposed DC distribution system with MIMO converter

The motivation of this dissertation is to design and fabricate MIMO converter, which can integrate the advantages of the MISO and SIMO configurations. The proposed non-isolated MIMO converters are advantageous on both conventional SISO converters and isolated MIMO converters as well. They have simple structure and provide easier power management. Thus, a non-isolated MIMO converter topology is discussed in this dissertation.

1.2 Literature Review

Depletion of fossil fuels due to more consumption of oil resources are results in increase in oil and natural gas prices. Increase in demand due to rapid rise in population results in more depletion of these oil reserves and thus acts as a justifiable reason for EVs to come into picture. The importance of integrating the electric vehicles with green and sustainable energy sources as a substitute for gas vehicles is consequently increasing. The electric vehicles are projected as an alternate future possibility for transportation applications in order to offer ecologically friendly operation with the utilization of green and sustainable energy sources[1]-[2]. In electric vehicles, FCs are usually used as alternate power source. The fuel cell is a power source that directly converts the chemical energy reaction into the electrical energy. Presently, fuel cells are accepted as one of the potential techs to meet the future power demands in EVs. Fuel cells generate electricity, rather than working as a battery for storage purpose it continues to supply power, until the fuel supply is maintained. However, there are some technical issues with fuel cells: they have slow power transfer rate in transition states, and a high cost per watt. This is the major reason behind non-usability of FCs as a single source in the electric vehicles in order to meet the load demands, generally during starting and transient periods. Therefore to meet the demand requirements, fuel cells are used with energy storage systems(ESSs) such as batteries or supercapacitors(SC). Moreover, the hybridization of FCs and ESSs leads to a reduction of the hydrogen consumption of the FC[3]-[7]. FC and ESSs, such as battery and SC have multiple voltage levels. So, to provide a particular voltage level for consumption by load and control the flow of power between input sources, a DC–DC converter for every input source is needed. Utilization of a dc–dc converter for every input source leads to increase of price, mass, and losses. Therefore, in hybridized power system, multi-input dc–dc converters are being used. Multi-input converters have two main types, isolated multi-input dc–dc converters and non-isolated multi-input dc–dc converters. In the following sections, two main types of multi-input converters are investigated.

In isolated multi-input DC–DC converters, high-frequency transformers are used for electric isolation. For impedance matching and electric isolation, these high frequency transformers are provided. Generally, isolated dc–dc converters use leakage inductance as storage for energy thereby transferring power amongst two sides of converter. Generally isolated dc–dc converters, in addition to high-frequency transformer, have high-frequency inverter and rectifier. The energy flow between input and output sides of converter is controlled by adjusting the phase shift angle between primary and secondary voltages of transformer [8]-

[10]. Isolated dc–dc converters have several types such as half-bridge isolated converters, full-bridge isolated converters, boost half-bridge isolated converters, and combinational multiport isolated converters [11]–[13]. As transformers are used, isolated dc–dc converters become heavy and bulky. These types of converters require inverter on the input side of the transformer for conversion of input dc to ac and they also need rectifier at the output of the transformer for conversion of ac to dc. As a result, at each input-output terminals of these converters, several switching devices are placed which leads to increment of cost and losses. Moreover, transformer itself has core and winding losses. Evaluating the abovementioned drawbacks of isolated multi-input dc–dc converters, usage of non-isolated multi-input dc–dc converters in electric vehicle applications seems more beneficial. In [14], a non-isolated multi-input dc–dc converter which is imitated from H-bridge structure has been proposed. Actually, by cascading two H-bridge with different dc-link voltages, multiple voltages due to addition or subtraction of H-bridges outputs are possible. In this negative voltage modes are eliminated as they are linked to bidirectional double-input converters, which are beyond the scope of this dissertation. By eliminating the abovementioned negative voltage modes, a simple version of double input dc–dc converter is obtained. The advantage of these converters are its less number of passive elements, and its drawback is inappropriate control on the power which is drawn from the input sources. In [15]–[17], a mimo dc–dc buck converter is proposed. In fact, this type of converter comprises of two buck converters parallel at their inputs. One switch is in series to each input source to avert short circuiting of the sources. The benefit from this converter is reduction in the number of inductors(L) and capacitors(C) which eventually leads to reduction in the cost, size, and weight of converter. The proposed converter is flawed due to its lack of proper energy flow amongst the sources. In [18], mimo z-source dc–dc converter is introduced. The converters structure is changed such that the number of inductors(L) and capacitors(C) are equal to a single input z-source converter. Still, two inductors and capacitors are utilized in the proposed converter. In [19], multi-phase converter is presented. The converter proposed hereby has four input at multiple different voltages. In this converter, each of the power sources can absorb or deliver power from load and other sources. This converter is flawed as each separate input source required separate inductor. In [20], a three-input converter for hybridization of battery, PV cells, and FC is presented by the researcher. By providing appropriate switching to the converter, charging and discharging of battery from other sources and load is possible, respectively. In [21], a logical approach for derivation of non-isolated multi-input converter topologies by combination of buck, boost, cuk, and sepic is introduced. According to this paper, abovementioned converters were categorized in two ways, one is pulsating voltage source

converters (PVSC) and other is pulsating current source converters (PCSC). As PVSC is used here as voltage source, it can put series with current buffer (inductor) branch or output of other converter in order to form a dual input converter. Also, because PCSC is considered as a current source, it may be placed in parallel with a capacitor branch or output of the other converter to form a dual input converter. In [22], a new converter for power and energy management between battery, SC, and electric motor in an EV is presented. In this converter, a coupled inductor is used as a substitute for two separate inductors as energy storing element. The paper claims that utilization of coupled inductor leads to 22%–26% reduction in volume when compared with two separated inductors. However, volume of coupled inductor is more than a single inductor. Also, regeneration of brake energy to battery and SC is possible with this converter. In [23], a mimo converter with only one inductor(L) is proposed which is used to allocate load power among input sources. Moreover, in the proposed mimo converter, transferring energy amongst sources is made possible. In [24], a new extendable single stage multi-input dc–dc/ac boost converter presented by the researcher. Low-torque ripple is highly essential in EVs. Torque ripple is directly related to voltage harmonics in an ac motor. Multilevel inverters are therefore utilized to reduce voltage harmonics. To generate different level voltages by multilevel inverters, DC sources with different or equal voltage level is essential. One such way to generate is to use mimo dc–dc converters. In [25] and [26], a single inductor(L) mimo DC–DC converter is presented which can be used to generate various different multiple voltage levels at the output. The converter regulates the output voltages at the required values despite the load variation or input voltage variation by controlling it. In [27], a new control scheme is introduced providing satisfactory dynamic performance for mimo converter. But the drawback of this converter is its single input source. In other words, in applications such as electric vehicles requiring several input energy sources like FC and battery are employed, this converter is not compatible. One way to rectify this problem is using of mimo converters. In [28] and [29], a non-isolated multi-input multi-output converter is presented which has only one inductor(L). Since it used more number of switches this becomes its major drawback which results in low efficiency of the converter. Impossibility of power transferring between input sources is the other shortcomings of the presented converter. In this dissertation, a multi-input multi-output non-isolated converter based on combination of a multiple inputs and multiple outputs is presented. The presented converter compared to similar converters requires less number of elements. The power flow in the converter can be controlled between each source and the load. The presented converter has several outputs for having

different voltage levels. Different control schemes were also implemented to maintain output voltage constant under input as well as load variations.

1.3 Research Objectives

The aim of this dissertation is to develop a compact and cost-effective power electronic converter for efficient power conversion for application in future low-voltage DC-DC systems. The work presented in this dissertation is first simulated and then experimentally implemented using ATmega328p microcontroller.

In view of current scenario in EV systems, multiport DC-DC converters are used efficiently, but the presented MIMO converter is able to provide efficient power and multiple voltages to the load. Specifically, this work includes:

- 1) Structure design and detailed analysis of non-isolated MIMO converters including one inductor only. Priorities are to have a compact design and effective cost of the converter. Therefore, non-isolated MIMO converter topology is demonstrated.
- 2) Dual input sources are connected to the converter and output voltage regulation at two levels is achieved. Controller design and tuning for MIMO system is also investigated.
- 3) Small signal model has been derived for controller design implemented on MIMO converter.
- 4) Fabrication of MIMO converter and driver circuit have been achieved through PCB design. Feasible design for compact structure has been incorporated.
- 5) Different control strategies viz. PI, PID, FOPID and ANN are developed and implemented using ATmega328p microcontroller.

1.4 Composition of the dissertation

The dissertation is organized in four parts. The first part consists of Chapter 1, which gives an outline about the literature review on the developments related to multiport DC-DC converters. The motivation, aim and objectives for pursuing the research has been described here.

The second part of this dissertation, comprising of Chapter 2 and Chapter 3, outlining the topology, analysis and dynamic modelling of the converters. Chapter 2 presents an overview of DC-DC converters followed by analysis of different topologies of multiport converters. Chapter 3 gives a detailed mathematical modelling and dynamic state space

analysis of MIMO converter. Small signal modelling technique is used to form a dynamic model of MIMO converter.

The third part of the dissertation comprises of Chapter 4, presenting the controller design concepts. Converter design specifications are also introduced here. Control strategies used to generate gate pulses are hereby discussed and structure of microcontroller used to generate those control signals are hereby presented.

Fourth part of the dissertation contains Chapter 5 and Chapter 6 which discusses the results obtained from various converter topologies with control strategies implemented. Simulated as well as experimental results are integrated in Chapter 5 with implementation of various control algorithms. Chapter 6 gives conclusions by summarizing the major finding and contribution of this work. Scope for future work is also highlighted here. Design of non-isolated multiport DC-DC Boost Converter and its component details are shown in appendices.

NON-ISOLATED MULTIPORT DC-DC BOOST CONVERTER TOPOLOGY

This chapter introduces various multiport DC-DC converter topologies based on boost converter. The converter structure, operating principle and different modes of operation are presented and analyzed in detail.

2.1 Overview

Switched mode DC-DC boost converter is used for stepping up the voltage (simultaneously stepping down current) from the input supply to its load output. It is classified in switched-mode power supply (SMPS) consisting of atleast two semiconductor devices (a transistor and a diode) and atleast one energy storing element i.e. either a capacitor or an inductor or may be a combination of both. Voltage ripples can be reduced by using capacitor filter at both input and output.

Basic working of boost converter relies on the principle of storing of energy in inductor from the supply side (dc or rectified ac) and then transferring it to the capacitor (or load itself). Therefore, output voltage steps up, resulting it to be greater than the input supply voltage. The basic circuit topology can be enhanced to give other variants of the boost converter. Here we are discussing non-isolated DC-DC converters which can be classified into three parts:

- i. Single Input Single Output (SISO)
- ii. Single Input Multiple Output (SIMO)
- iii. Multiple Input Multiple Output (MIMO)

Detailed analysis of these DC-DC converters will be done later in this chapter.

2.2 Multiport Converter Topology

In [25], a multi-output converter is proposed. The presented converter is a single input converter. On the other hand, use of one input energy source in electric vehicles cannot provide load requirements because the load is dynamic and the power varies. Therefore, hybridization of different sources is vital. In [23], a non-isolated multi-input dc–dc converter

for hybridization of energy sources is proposed having just one inductor. In this thesis, a non-isolated multi-input multi-output dc–dc converter based on the integration of these two converters is proposed. The structure of the proposed converter is presented in Fig. 1. As seen from the figure, the converter interfaces m input power sources $V_{in1}, V_{in2}, V_{in3}, \dots, V_{inm}$ such that $V_{in1} < V_{in2} < V_{in3} \dots < V_{inm}$. The presented converter has just one inductor, n capacitors in its outputs and $m + n$ switches. The $R_1, R_2, R_3, \dots, R_n$ are the load resistances, which can represent the loads which can be taken as equivalent to power feeding a multilevel inverter. By proper switching of switches, control of power flow between input sources in addition to boost up input sources voltages is possible. Outputs are capable to have equal or different voltage level which is suitable for a connection to a multilevel inverter. The proposed converter is appropriate alternative for hybridizing of FC, battery, or SC.

In a hybrid electric vehicle (HEV), hybridization of different alternate sources is vital and therefore FC and battery can be considered here as input sources. Outputs can be resistive loads or loads present in HEVs like entertainment system, lightning system, charging ports, etc. as shown in Fig. 2.1

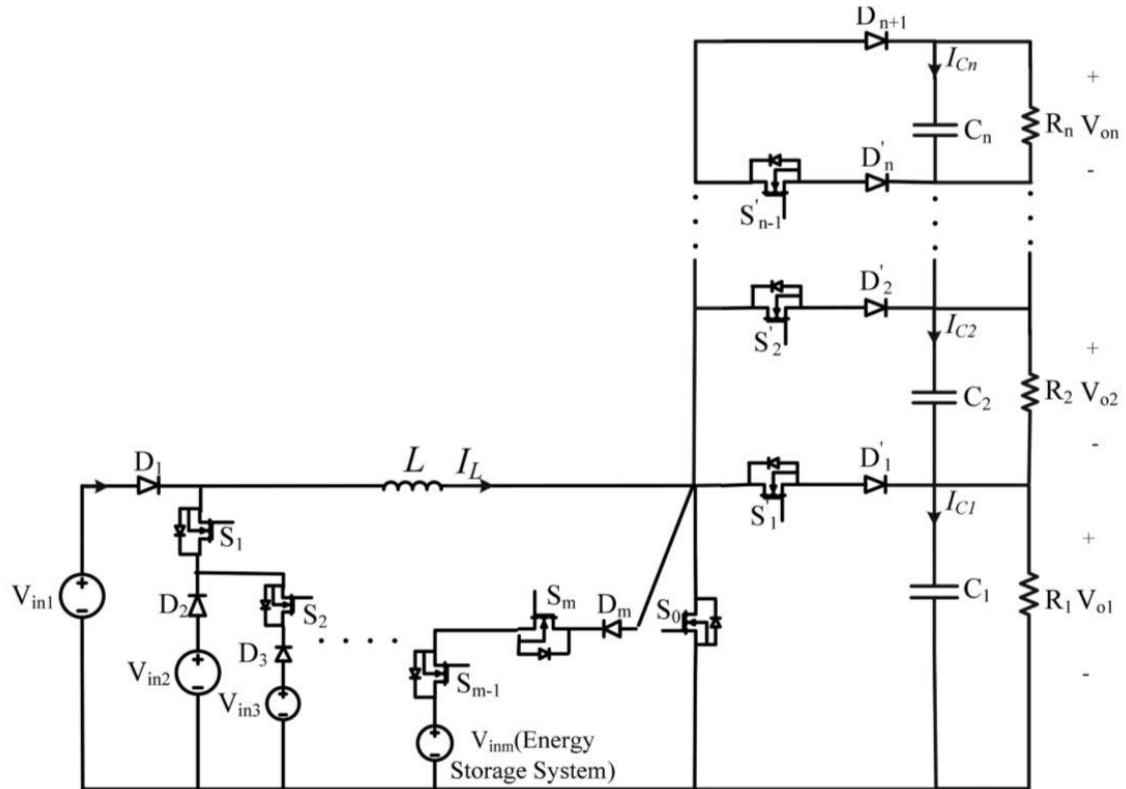


Fig. 2.1 Multiport converter structure

In single input single output (SISO) mode supply is from one input and here resistive load is taken as single output. This is a conventional form of DC-DC boost converter. Power transfer takes place between input supply (here a charged battery) and output load (resistive type).

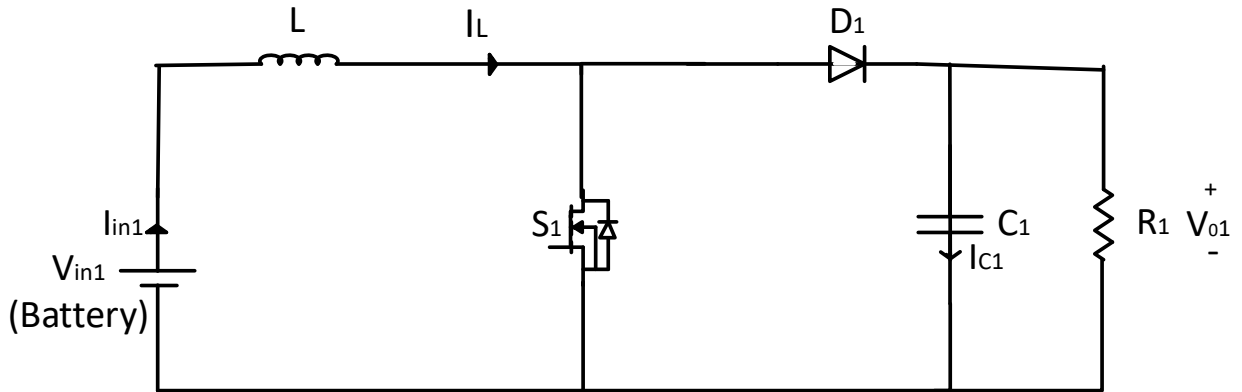


Fig. 2.2 Single input single output converter structure

In single input multiple output (SIMO) mode single charged battery act as input supply and two or more resistive loads as output. This is a non-isolated SIMO converter topology and here power transfer occurs between one input supply and two resistive loads.

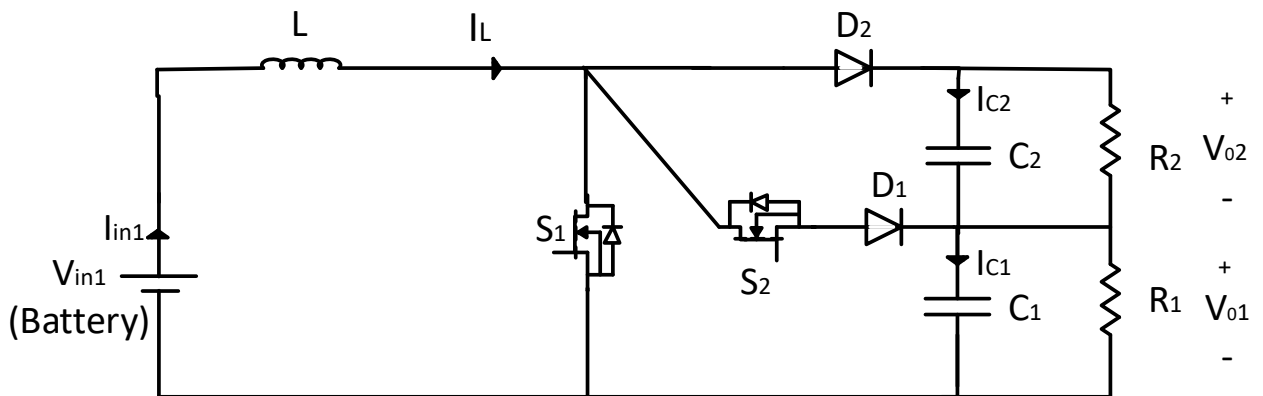


Fig. 2.3 Single input Multiple output converter structure

In multiple input multiple output (MIMO) mode two or more input supply are used to transfer power to two or more output loads. Here FC and battery is used to supply power to two resistive loads. The non-isolated structure is compact in design and cost-effective in nature.

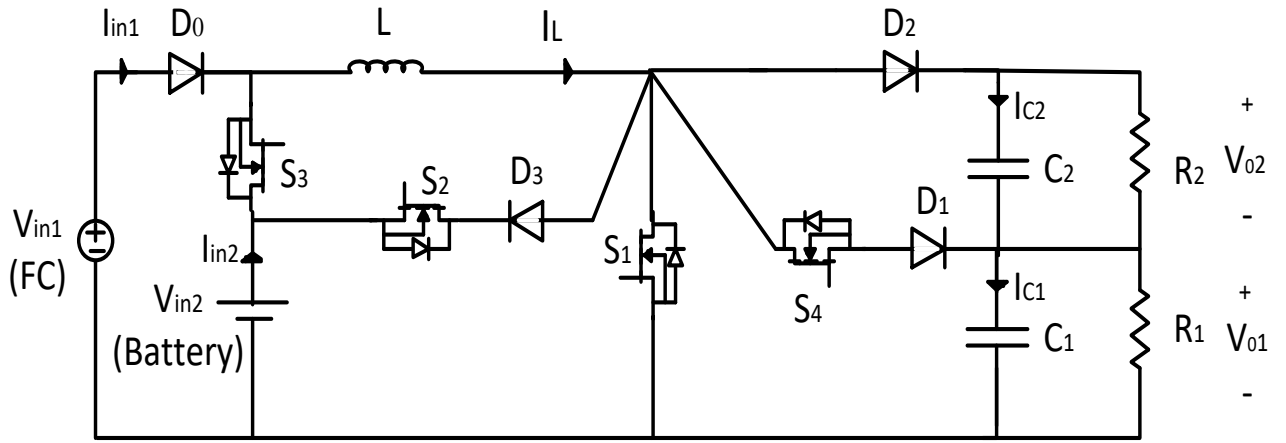


Fig. 2.4 Multiple input multiple output converter structure

2.3 Analysis of the Multiport Boost Converter

In a boost converter topology as discussed earlier, conventional boost converters are merged for providing new topologies to get multiport converter. If we consider hybridizing alternate energy sources to be used as input sources for the converter which includes FC and ESS (here battery) then usage of each source accordingly can result in development of different topologies. Here we discuss detailed structure of each topology (i.e. conventional and proposed), its operating modes and useful mathematical equations. Classification of DC-DC Boost topology for non-isolated structure is as follows:

- i. Single Input Single Output (SISO)
- ii. Single Input Multiple Output (SIMO)
- iii. Multiple Input Multiple Output (MIMO)

2.3.1 Single Input Single Output (SISO)

Single input single output converter topology is the conventional converter topology. The converter structure is shown in Fig. 2.2. It considers just one input supply and one resistive load at the output. In this structure inductor stores energy in one cycle from the input supply and in the next cycle it delivers the energy stored to the loads at the output. The cycle period is decided by the duty of the switch used in the converter.

2.3.2 Single Input Multiple Output (SIMO)

The multiport converter topology discussed above in Fig. 2.3 can be converted into SIMO converter structure. Considering just one input supply and two resistive loads as outputs we can simulate the structure of SIMO DC-DC converter. In the fig. 2.3, the SIMO converter has one-input two-output structure. In this figure, R_1 and R_2 are model equivalent resistances to denote either HEV system components or a multilevel inverter. Different types of multilevel inverters can be used in connection to this converter. HEVs have various DC-DC loads such as lightning or music system which can directly be feed from the converter output. But HEVs are difficult to operate with just one input supply as discussed earlier.

2.3.3 Multiple Input Multiple Output (MIMO)

In this thesis, the presented converter has two-input two-output structure. In Fig. 2.4, the converter with two-input two-output is shown. In this figure, R_1 and R_2 are the model of load resistances that can denote the equivalent power feeding an HEV system or a multilevel inverter. Different types of multilevel inverters can be used in connection to this converter. HEVs have various DC-DC loads such as lightning or music system which can directly be feed from the converter output. Four power switches S_1 , S_2 , S_3 , and S_4 in the converter structure are the major controlling elements that control the output voltages and power flow of the converter. In the presented converter, source V_{in1} can deliver power to source V_{in2} but not vice versa due to presence of diode D_3 . So, in EVs, FC which cannot be charged, so it is located in place of V_{in1} in circuit. Also, generally where V_{in2} is placed, ESSs such as battery or Super Capacitor (SC) which are chargeable are placed.

In this thesis, FC is used as a generating power source (V_{in1}) and the battery is used as an ESS (V_{in2}). Depending on the operation of the battery, two modes of operation are defined for the presented converter. In every mode, only three of the four switches are active, while one switch is inactive. When high power load is present, both input sources deliver power to the load, in such a state, S_2 is inactive and switches S_1 , S_3 , and S_4 are active. Also, when low power load is present and V_{in2} is needed to be charged, V_{in1} supplies power to loads and can also charge the battery i.e. V_{in2} . In this situation, switches S_1 , S_2 , and S_4 are active and S_3 is inactive. In FCs, as output voltage depends on the current drawn and to make equal power balance among the input powers and the load, ripples of the current drawn should be minimized. Therefore, in this thesis, steady state and dynamic behavior of the converter have been investigated in CCM. However, in battery charging mode, the load power and battery charging

current have small values, it is likely that the converter works in discontinuous conduction mode (DCM). So, the condition in which the converter goes in DCM is discussed later in next chapter. It should be noted that each of input sources can be used separately making it the case of SIMO converter type. Two main operation modes of the converter have been studied as follows:

2.3.3.1 First Operation Mode (Battery Discharging Mode)

In this mode of operation, two input sources V_{in1} and V_{in2} (battery) are responsible for supplying power to the loads. In this mode, S_2 is completely OFF and S_1 , S_3 , and S_4 are ON. For each switch, a specific duty is required. Here, S_1 is active to regulate supply source 2 (battery) current to desired value. In fact, S_1 controls battery current to desired value by regulating inductor current. The total output voltage $V_T = V_{O1} + V_{O2}$ is controlled to a desired value by the switch S_3 . Also, output voltage V_{O1} is regulated by S_4 . It is apparent that by regulation of V_T and V_{O1} , the output voltage V_{O2} is regulated accordingly. Gate signals of switches with voltage and current waveforms of inductor are shown in Fig. 2.5.

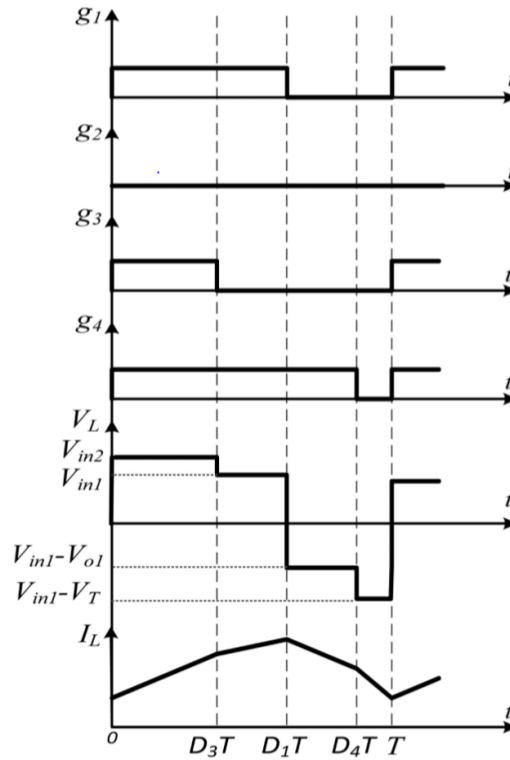


Fig. 2.5 Steady-state waveforms of MIMO converter in battery discharging mode

According to switching states of the switches, there are four different operating modes in one switching period as follows:

1) Switching State 1 ($0 < t < D_3T$):

In this state, switches S_1 and S_3 are made active by giving gate pulses. Since S_1 is ON, diodes D_1 and D_2 are made reverse biased, so switch S_4 is turned OFF. Since S_3 is active and $V_{in1} < V_{in2}$, diode D_0 is reverse biased. Equivalent circuit of the proposed converter in this state is shown in Fig. 2.6(a). In this switching state, V_{in2} charges inductor L , so inductor current increases. Simultaneously, in this state, capacitors C_1 and C_2 are discharged and deliver their stored energy to load resistances R_1 and R_2 , respectively.

The inductor and capacitors equations in this mode are as follows:

$$\begin{cases} L \frac{di_L}{dt} = v_{in2} \\ C_1 \frac{dv_{01}}{dt} = -\frac{v_{01}}{R_1} \\ C_2 \frac{dv_{02}}{dt} = -\frac{v_{02}}{R_2} \end{cases} \quad (2.1)$$

2) Switching State 2 ($D_3T < t < D_1T$):

In this switching state, switch S_1 is still active and S_3 is turned inactive. Since S_1 is ON, diodes D_1 and D_2 are made reverse biased, so switch S_4 is still inactive. Equivalent circuit diagram of proposed converter in this state is shown in Fig. 2.6(b). In this state, V_{in1} charges inductor L , so inductor current furthermore increases. Simultaneously, capacitors C_1 and C_2 are discharged and delivers its stored energy to load resistances R_1 and R_2 , respectively. The inductor and capacitors equations in this state are as follows:

$$\begin{cases} L \frac{di_L}{dt} = v_{in1} \\ C_1 \frac{dv_{01}}{dt} = -\frac{v_{01}}{R_1} \\ C_2 \frac{dv_{02}}{dt} = -\frac{v_{02}}{R_2} \end{cases} \quad (2.2)$$

3) Switching State 3 ($D_1T < t < D_4T$):

In this state, switch S_1 is turned inactive and switch S_3 is still inactive. Also, switch S_4 is turned ON. Diode D_2 is reversed biased. Equivalent circuit of proposed converter in this state is shown in Fig. 2.6(c). In this state, discharging on inductor L occurs and power is delivered to C_1 and

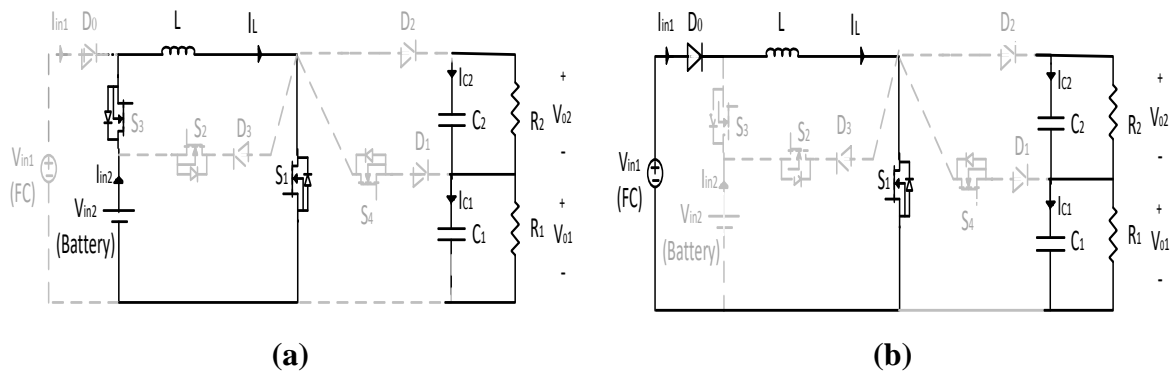
R_1 , so inductor current decreases. In this state, C_1 is charged and C_2 is discharged and delivers its stored energy to load resistance R_2 . The energy storing elements L , C_1 , and C_2 equations in this mode are as follows:

$$\begin{cases} L \frac{di_L}{dt} = v_{in1} - v_{01} \\ C_1 \frac{dv_{01}}{dt} = i_L - \frac{v_{01}}{R_1} \\ C_2 \frac{dv_{02}}{dt} = -\frac{v_{02}}{R_2} \end{cases} \quad (2.3)$$

4) Switching State 4 ($D_4T < t < T$):

In this mode, all of three switches are inactive. So, diode D_2 is made forward biased. In this state, inductor L discharges and delivers its stored energy to capacitors C_1 , C_2 , and load resistances R_1 and R_2 . Simultaneously in this mode, capacitors C_1 and C_2 are charged. Equivalent circuit of proposed converter in this state is shown in Fig. 2.6(d). The inductor L and capacitors C_1 and C_2 equations for this mode are as follows:

$$\begin{cases} L \frac{di_L}{dt} = v_{in1} - (v_{01} + v_{02}) \\ C_1 \frac{dv_{01}}{dt} = i_L - \frac{v_{01}}{R_1} \\ C_2 \frac{dv_{02}}{dt} = i_L - \frac{v_{02}}{R_2} \end{cases} \quad (2.4)$$



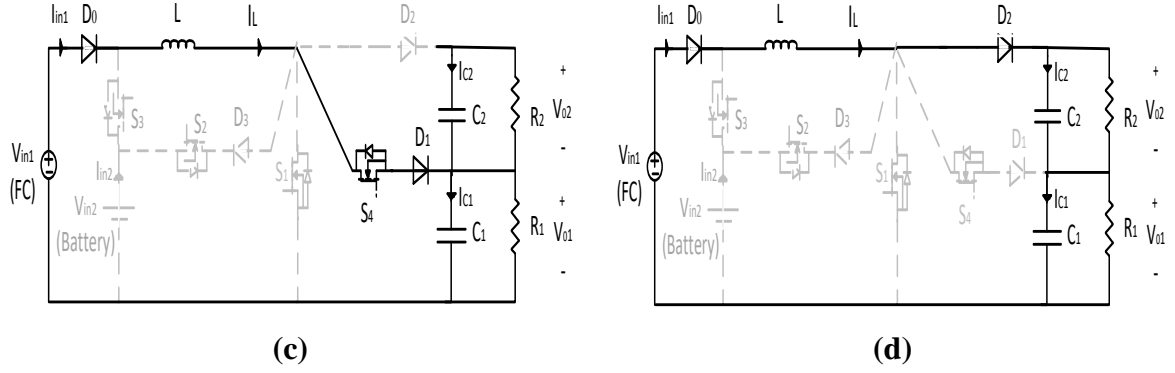


Fig. 2.6 Equivalent circuit of battery discharging mode during (a) switching state 1, (b) switching state 2, (c) switching state 3, and (d) switching state 4.

2.3.3.2 Second Operation Mode (Battery Charging Mode)

In this operating mode, V_{in1} not only supplies loads but also delivers power to V_{in2} (battery) for charging purpose. The implementation on this mode on experimental setup is out of the scope of this thesis. This condition occurs when load power is small and battery requirements are to be charged. In this operating mode, switches S_1 , S_2 , and S_4 are ON and switch S_3 is entirely inactive. Like previous operating mode of the converter in this mode, for each switch, a specific duty for controlling is vital. S_1 is switched to regulate total output voltage $V_T = V_{O1} + V_{O2}$ to a required value.

Controlling of the battery charging current (I_b) to a required value is the duty of switch S_2 , controlling the output voltage V_{O1} is duty of switch S_4 . It is known that by regulating V_T and V_{O1} , the output voltage V_{O2} is regulated accordingly. In Fig. 2.7, gate pulse signals of switches and voltage and current waveforms of inductor are shown.

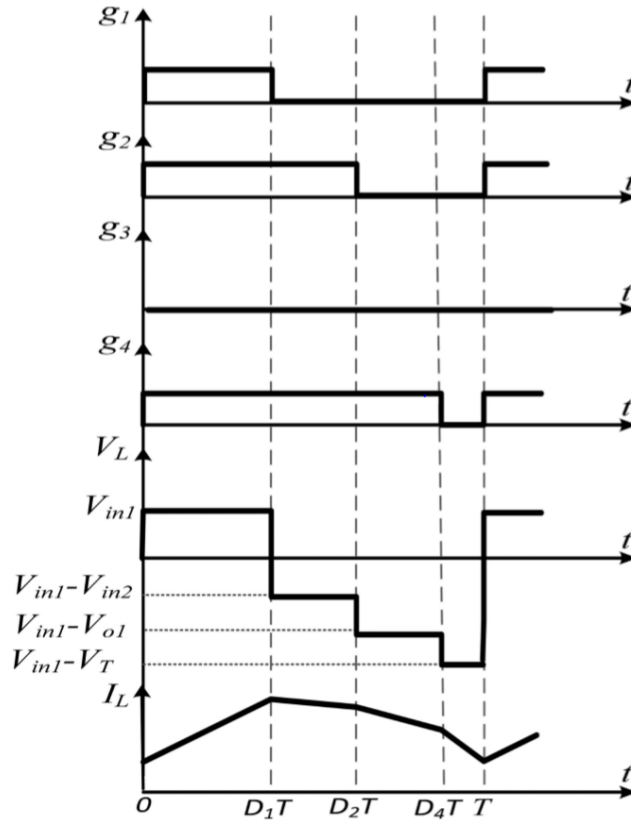


Fig. 2.7 Steady-state waveforms of MIMO converter in battery charging mode

According to different switching states, there are four different operating modes in one switching period which is discussed as follows:

1) Switching State 1 ($0 < t < D_1T$):

In this state, switch S_1 is turned ON, so S_2 and S_4 are reversed biased and cannot be turned ON. Also, diode D_2 is reversely biased and could not conduct. Equivalent circuit of proposed converter in this state is shown in Fig. 2.8(a). In this state, V_{in1} charges the inductor L , so inductor current increases. Also, in this state, capacitors C_1 and C_2 are discharged and delivers their stored energy to load resistances R_1 and R_2 , respectively. The inductor L and capacitors C_1 and C_2 equations in this mode are as follows:

$$\begin{cases} L \frac{di_L}{dt} = v_{in1} \\ C_1 \frac{dv_{01}}{dt} = -\frac{v_{01}}{R_1} \\ C_2 \frac{dv_{02}}{dt} = -\frac{v_{02}}{R_2} \end{cases} \quad (2.5)$$

2) Switching State 2 ($D_1T < t < D_2T$):

In this mode, switch S_1 is turned OFF and switch S_2 is turned ON. Diodes D_1 and D_2 are reversely biased, subsequently, S_4 is still inactive. Equivalent circuit of proposed converter in this switching state is shown in Fig. 2.8(b). Since $V_{in1} < V_{in2}$, therefore, in this period of time, inductor current decreases and inductor transfers its stored energy to battery (V_{in2}). Also, in this switching mode, capacitors C_1 and C_2 are discharged and deliver their stored energy to load resistances R_1 and R_2 respectively. The inductor L and capacitors C_1 and C_2 equations in this mode are as follows:

$$\begin{cases} L \frac{di_L}{dt} = v_{in1} - v_{in2} \\ C_1 \frac{dv_{01}}{dt} = -\frac{v_{01}}{R_1} \\ C_2 \frac{dv_{02}}{dt} = -\frac{v_{02}}{R_2} \end{cases} \quad (2.6)$$

3) Switching State 3 ($D_2T < t < D_4T$):

In this switching mode, switch S_1 is still OFF and switch S_2 is turned OFF and switch S_4 is turned ON. Also, diode D_2 is reversely biased. In Fig.2.8(c), equivalent circuit of proposed converter in this state is shown. In this state, inductor L is delivers its stored energy to C_1 and R_1 and gets discharged, so inductor current is decreased. In this state, capacitors C_1 is charged and capacitor C_2 is discharged and delivers its stored energy to load resistance R_2 . The energy storage elements L , C_1 , and C_2 equations in this mode are as follows:

$$\begin{cases} L \frac{di_L}{dt} = v_{in1} - v_0 \\ C_1 \frac{dv_{01}}{dt} = i_L - \frac{v_{01}}{R_1} \\ C_2 \frac{dv_{02}}{dt} = -\frac{v_{02}}{R_2} \end{cases} \quad (2.7)$$

4) Switching State 4 ($D_4T < t < T$):

In this mode, all the three switches are OFF. Therefore, diode D_2 is forward biased. In Fig. 2.8(d), an equivalent circuit of the proposed converter in this switching state is shown. In this state, inductor L discharges and delivers its stored energy to capacitors C_1 , C_2 , and load

resistances R_1 and R_2 . Also, in this mode, capacitors C_1 and C_2 are charged. The inductor L and capacitors C_1 and C_2 equations in this mode are as follows:

$$\begin{cases} L \frac{di_L}{dt} = v_{in1} - (v_{o1} + v_{o2}) \\ C_1 \frac{dv_{o1}}{dt} = i_L - \frac{v_{o1}}{R_1} \\ C_2 \frac{dv_{o2}}{dt} = i_L - \frac{v_{o2}}{R_2} \end{cases} \quad (2.8)$$

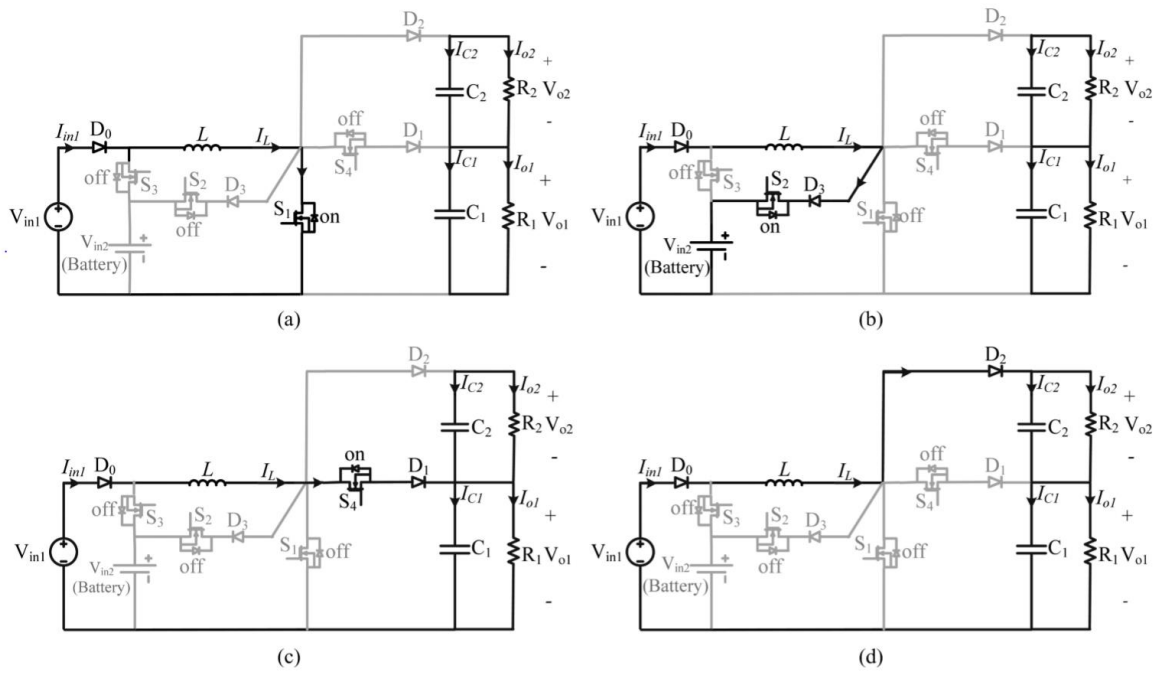


Fig. 2.8 Equivalent circuit of battery charging mode during (a) switching state 1, (b) switching state 2, (c) switching state 3, and (d) switching state 4.

DYNAMIC MODELLING OF NON-ISOLATED MULTI-PORT DC-DC BOOST CONVERTER

In this chapter, small signal modelling is discussed and the parameters of the converter circuit are introduced. For designing the best optimal controller, small signal modelling plays a vital role. Multiport converters are of higher order and so it is a tough task to get the dynamics of such converters. Thus, design of such model is needed in order to optimize converter dynamics and also helps in realizing the closed-loop control. The dynamic modelling of only MIMO converter is explained here in detail. By system mathematical equations, and by considering state equations for each mode, small signal transfer function is developed. Inductor and capacitor design are also discussed in this chapter.

3.1 Dynamic Modelling and Analysis

As mentioned in previous chapter, the presented MIMO converter is controlled by switches S_1 , S_2 , S_3 , and S_4 . Each switch needs some gate signal with specific duty in order to provide control to the converter. On controlling the duty of the switches, voltage and current values can be regulated. In order to control the converter and design specific controller, initially dynamic modelling must be achieved. As discussed in previous chapter, presented converter has two main operating modes which is battery discharging mode in which two input sources supply power to load and battery charging mode in which source V_{in1} supplies both the load power and battery (V_{in2}) for charging purpose. This mode is theoretically explained here but not implemented on experimental setup. Each operation modes have different dynamics and so each mode is differently modelled. Accordingly, for each operating mode, different controllers are needed to be designed separately. Dynamic modelling of both modes is presented in this thesis but controllers were designed for battery discharging mode only.

3.1.1 Dynamic modelling of Battery Discharging Mode

The basis for optimized controller design is small signal modelling. Especially, for such a multi-input multi-output converter, an effective dynamic modelling of converter structure will be helpful to realize closed-loop control, and moreover, to optimize the converter dynamics. Unlike conventional SISO converter, the MIMO converter is higher order system, and it is even

more problematic to derive the plant transfer functions making it more difficult to obtain values of zeros and poles for the purpose of analysis. As an alternative, matrix representation of plant dynamics is obtained and computer simulation software is used to plot graphs of different transfer functions. In small signal modelling method [30], the state variables, duty ratios, and input voltages contain two components, dc values (X , D , V) and perturbations (\hat{x} , \hat{d} , \hat{v}). It is assumed that the perturbations are quite small and do not vary significantly during one switching period. So, the following equations for proposed converter are:

$$\begin{cases} i_L(t) = I_L + \hat{i}_L(t) \\ v_{o1}(t) = V_{o1} + \hat{v}_{o1}(t) \\ v_{o2}(t) = V_{o2} + \hat{v}_{o2}(t) \\ d_1(t) = D_1 + \hat{d}_1(t) \\ d_2(t) = D_2 + \hat{d}_2(t) \\ d_3(t) = D_3 + \hat{d}_3(t) \\ d_4(t) = D_4 + \hat{d}_4(t) \end{cases} \quad (3.1)$$

where inductor current $i_L(t)$ and capacitor voltages $v_{o1}(t)$ and $v_{o2}(t)$ are state variables. If we substitute (3.1) into (2.1)–(2.4), apply the averaging to four state equations multiplied with corresponding duty cycle value, and subsequently neglecting second-order terms, we find small-signal model equations that are presented as follows:

$$\begin{cases} L \frac{d\hat{i}_L(t)}{dt} = (V_{in2} - V_{in1})\hat{d}_3(t) + D_3\hat{v}_{in2}(t) + (1 - D_3)\hat{v}_{in1}(t) \\ \quad - (1 - D_1)\hat{v}_{o1}(t) + (D_4 - 1)\hat{v}_{o2}(t) + V_{o1}\hat{d}_1(t) + V_{o2}\hat{d}_4(t) \\ C_1 \frac{d\hat{v}_{o1}(t)}{dt} = -I_L\hat{d}_1(t) + (1 - D_1)\hat{i}_L(t) - \frac{\hat{v}_{o1}(t)}{R_1} \\ C_2 \frac{d\hat{v}_{o2}(t)}{dt} = -I_L\hat{d}_4(t) + (1 - D_4)\hat{i}_L(t) - \frac{\hat{v}_{o2}(t)}{R_2} \end{cases} \quad (3.2)$$

Thus, the system can be represented in a matrix form using a state-space model such taking $i_L(t)$, $v_{o1}(t)$, and $v_{o2}(t)$ as state variables. The state-space model is as follows:

$$\begin{cases} \frac{dX}{dt} = AX + BU \\ Y = CX + DU \end{cases} \quad (3.3)$$

where X represent state variable matrix, U represent control input matrix having $d_1(t)$, $d_3(t)$ and $d_4(t)$, and Y represents system output matrix having $v_{o1}(t)$, $v_T(t)$, and $i_b(t)$. Thus, matrices X , Y and U are as follows:

$$X = \begin{bmatrix} \hat{i}_L(t) \\ \hat{v}_{o1}(t) \\ \hat{v}_{o2}(t) \end{bmatrix}, Y = \begin{bmatrix} \hat{v}_{o1}(t) \\ \hat{v}_T(t) \\ \hat{v}_{o2}(t) \end{bmatrix}, U = \begin{bmatrix} \hat{d}_4(t) \\ \hat{d}_3(t) \\ \hat{d}_1(t) \end{bmatrix} \quad (3.4)$$

Substitute the A, B, C, and D matrices using equations (3.2) and state equations (3.3), and following results is obtained:

$$\begin{aligned} A &= \begin{bmatrix} 0 & \frac{(D_1 - 1)}{L} & \frac{(D_4 - 1)}{L} \\ \frac{(1 - D_1)}{C_1} & -\frac{1}{R_1 C_1} & 0 \\ \frac{(1 - D_4)}{C_2} & 0 & -\frac{1}{R_2 C_2} \end{bmatrix} \\ B &= \begin{bmatrix} \frac{V_{O2}}{L} & \frac{V_{O2}}{L} & \frac{(V_{in2} - V_{in1})}{L} \\ 0 & -\frac{I_L}{C_1} & 0 \\ -\frac{I_L}{C_2} & 0 & 0 \end{bmatrix} \\ C &= \begin{bmatrix} 0 & 1 & 0 \\ 0 & 1 & 1 \\ D_3 & 0 & 0 \end{bmatrix} \\ D &= \begin{bmatrix} 0 & 0 & 0 \\ 0 & 0 & 0 \\ 0 & I_L & 0 \end{bmatrix} \end{aligned} \quad (3.5)$$

where V_{in1} and V_{in2} are input supply voltages. Also, V_{O1} & V_{O2} are load voltages at the output. In the A, B, C, and D matrices, each parameter value except duty cycle of switches D_1 , D_3 , D_4 , and dc value of inductor current I_L , is known. The following equation evaluates inductor current value:

$$I_L = \frac{I_b}{D_3} \quad (3.6)$$

where I_b is the battery current. So, now the unknown parameters of abovementioned matrices are D_1 , D_3 , and D_4 . The values of duty applied to the switches is obtained by steady-state analysis which is shown in following equation:

$$\begin{bmatrix} V_{O1} & V_{in2} - V_{in1} & V_{O2} \\ R_1 I_b & V_{O1} & 0 \\ 0 & V_{O2} & R_2 I_b \end{bmatrix} \begin{bmatrix} D_1 \\ D_3 \\ D_4 \end{bmatrix} = \begin{bmatrix} V_{O2} + V_{O1} - V_{in1} \\ R_1 I_b \\ R_2 I_b \end{bmatrix} \quad (3.7)$$

So, from the above-mentioned matrix equation, duty to the switches is achieved and is substituted in A, B, C, and D matrices. As represented in the system small-signal models, state variables are controlled by three control variables $d_1(t)$, $d_3(t)$, and $d_4(t)$. The transfer function matrix of the converter is obtained from the small signal model as follows:

$$G = C(SI - A)^{-1}B + D \quad (3.8)$$

where

$$y = Gu \quad (3.9)$$

The rank of transfer function matrix denotes the number of control variables. In this thesis, according to the number of control variables and from (3.4), rank of transfer function matrix G is 3×3

$$\begin{bmatrix} y_1 \\ y_2 \\ y_3 \end{bmatrix} = \begin{bmatrix} g_{11} & g_{12} & g_{13} \\ g_{21} & g_{22} & g_{23} \\ g_{31} & g_{32} & g_{33} \end{bmatrix} \begin{bmatrix} u_1 \\ u_2 \\ u_3 \end{bmatrix} \quad (3.10)$$

where y and u are the system output and input vectors, and component g_{ij} represents the transfer function between y_i and u_j . So, there are three transfer functions as follows:

$$\begin{cases} \frac{\hat{v}_{O1}(s)}{\hat{d}_4(s)} = g_{11} \\ \frac{\hat{v}_T(s)}{\hat{d}_3(s)} = g_{22} \\ \frac{\hat{i}_b(s)}{\hat{d}_1(s)} = g_{33} \end{cases} \quad (3.11)$$

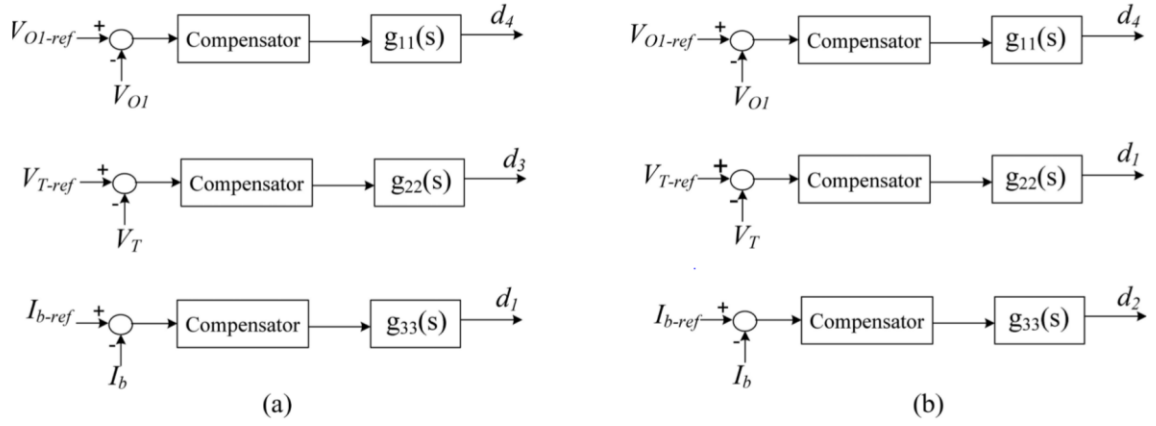


Fig. 3.1 Control block diagram of MIMO converter for (a) battery discharging mode, and (b) battery charging mode.

3.1.2 Dynamic Modelling of Battery Charging Mode

In this operation mode of presented converter, which V_{in1} delivers energy to loads and V_{in2} (battery), switches S_1 , S_2 , and S_4 are active and switch S_3 is inactive. Like battery discharging mode, first small signal modelling must be done by substituting (3.1) into (2.5)–(2.8), applying the averaging to four state equations multiplied with corresponding duty cycle value, and neglecting second-order terms, we obtain the small-signal model equations that are presented as follows:

$$\left\{ \begin{array}{l} L \frac{d\hat{i}_L(t)}{dt} = \hat{v}_{in1}(t) + V_{in2}\hat{d}_1(t) + (D_1 - D_2)\hat{v}_{in2}(t) + (V_{O1} - V_{in2})\hat{d}_2(t) \\ \quad + V_{O2}\hat{d}_4(t) + (D_2 - 1)\hat{v}_{O1}(t) - (1 - D_4)\hat{v}_{O2}(t) \\ C_1 \frac{d\hat{v}_{O1}(t)}{dt} = -I_L\hat{d}_2(t) + (1 - D_2)\hat{i}_L(t) - \frac{\hat{v}_{O1}(t)}{R_1} \\ C_2 \frac{d\hat{v}_{O2}(t)}{dt} = -I_L\hat{d}_4(t) + (1 - D_4)\hat{i}_L(t) - \frac{\hat{v}_{O2}(t)}{R_2} \end{array} \right. \quad (3.12)$$

These equations can be expressed as state space equations. In this operation mode similar to battery discharging mode $i_L(t)$, $v_{O1}(t)$, and $v_{O2}(t)$ are the state variables. State variables, input, and output matrices are shown below:

$$y = \begin{bmatrix} \hat{v}_{O1}(t) \\ \hat{v}_T(t) \\ \hat{i}_b(t) \end{bmatrix}, X = \begin{bmatrix} \hat{i}_L(t) \\ \hat{v}_{O1}(t) \\ \hat{v}_{O2}(t) \end{bmatrix}, u = \begin{bmatrix} \hat{d}_4(t) \\ \hat{d}_1(t) \\ \hat{d}_2(t) \end{bmatrix} \quad (3.13)$$

where $v_T(t) = v_{O1}(t) + v_{O2}(t)$. Finally, for this operation mode of converter, similar to previous mode, there are A, B, C, and D matrices as follows:

$$\begin{aligned}
 A &= \begin{bmatrix} 0 & \frac{(D_2 - 1)}{L} & \frac{(D_4 - 1)}{L} \\ \frac{(1 - D_2)}{C_1} & -\frac{1}{R_1 C_1} & 0 \\ \frac{(1 - D_4)}{C_2} & 0 & -\frac{1}{R_2 C_2} \end{bmatrix} \\
 B &= \begin{bmatrix} \frac{V_{in2}}{L} & \frac{(V_{O2} - V_{in2})}{L} & \frac{V_{O2}}{L} \\ 0 & -\frac{I_L}{C_1} & 0 \\ 0 & 0 & -\frac{I_L}{C_2} \end{bmatrix} \\
 C &= \begin{bmatrix} 0 & 1 & 0 \\ 0 & 1 & 1 \\ D_2 - D_1 & 0 & 0 \end{bmatrix} \\
 D &= \begin{bmatrix} 0 & 0 & 0 \\ 0 & 0 & 0 \\ -I_L & I_L & 0 \end{bmatrix}
 \end{aligned} \tag{3.14}$$

In the aforementioned matrices, all parameters except duty cycle of switches D_1 , D_2 , D_4 , and dc value of inductor current I_L are known. The following equation evaluates inductor current:

$$I_L = \frac{I_b}{D_2 - D_1} \tag{3.15}$$

where I_b is desired value of battery current. So, the unknown parameters of abovementioned matrices are D_1 , D_2 , and D_4 . The duty ratio values of the switches are obtained by steady-state equations as follows:

$$\begin{bmatrix} V_{in2} & V_{O2} - V_{in2} & V_{O2} \\ -V_{O1} & V_{O1} + R_1 I_b & 0 \\ -V_{O2} & V_{O2} & R_2 I_b \end{bmatrix} \begin{bmatrix} D_1 \\ D_3 \\ D_4 \end{bmatrix} = \begin{bmatrix} V_{O2} + V_{O1} - V_{in1} \\ R_1 I_b \\ R_2 I_b \end{bmatrix} \tag{3.16}$$

The transfer function matrix of the converter is obtained from the small signal model which is as follows:

$$G = C(SI - A)^{-1}B + D \quad (3.17)$$

where

$$y = Gu \quad (3.18)$$

where y and u are the system output and input vectors, so the three transfer functions are as follows:

$$\begin{cases} \frac{\hat{v}_{O1}(s)}{\hat{d}_4(s)} = g_{11} \\ \frac{\hat{v}_T(s)}{\hat{d}_1(s)} = g_{22} \\ \frac{\hat{i}_b(s)}{\hat{d}_2(s)} = g_{33} \end{cases} \quad (3.19)$$

It is important to note that in battery charging mode when the loads power and battery current have low values, the converter may possibly go to DCM mode. It is known that DC–DC converters will work in DCM if their inductor dc current be less than their inductor current ripple. So, for the presented converter in battery charging mode by averaging of the inductor voltage and capacitors current during a switching period, the dc equations can be obtained as follows:

$$\begin{cases} V_{in2}D_1 + (V_{O1} - V_{in2})D_2 + V_{O2}D_4 = V_{O1} + V_{O2} - V_{in1} \\ -I_L D_2 + I_L = \frac{V_{O1}}{R_1} \\ -I_L D_4 + I_L = \frac{V_{O2}}{R_2} \end{cases} \quad (3.20)$$

also, the inductor current ripple in battery charging mode can be expressed as

$$\Delta I_L = \frac{V_{in2}D_1T_s}{L} \quad (3.21)$$

So, from (3.15), (3.20), and (3.21), the converter will work in DCM if the following conditions be satisfied:

$$\begin{cases} R_1 > \frac{V_{O1}Lf_s}{D_1(1-D_4)V_{in1}} \\ R_2 > \frac{V_{O2}Lf_s}{D_1(1-D_4)V_{in1}} \\ I_b < \frac{V_{in1}D_1(D_2-D_1)}{Lf_s} \end{cases} \quad (3.22)$$

In fact, (3.22) confirms that the presented converter will work in DCM when the output loads are light and the battery charging current has low value. Since this mode is not implemented experimentally controller design is not performed on this operating mode.

CHAPTER 4

CONTROL STRATEGIES FOR NON-ISOLATED MULTI-PORT DC-DC BOOST CONVERTER

4.1 Introduction

Small signal modelling of the multiport converter is done using the perturbations as the state variables for the state space analysis. Using this state space structure, transfer functions are derived for controlling parameters of the multiport converter as discussed in the previous chapter.

In this chapter, the transfer functions for both the operations modes, i.e. battery discharging and battery charging mode, can be derived. Since battery discharging mode is presented in this work, only this mode will be further investigated for controller design purpose. In this work, battery charging mode is limited to theoretical knowledge only and controller design and implementation for this mode will be available for future scope. ATmega328p (Arduino UNO) microcontroller have been used to practically implement various control strategies on the experimental setup.

The following section describes different control algorithms for non-isolated multi-input multi-output DC-DC boost converter i.e. Proportional-Integral (PI) control, Proportional-Integral-Derivative (PID) control, Fractional Order Proportional-Integral-Derivative (FOPID) control, and Artificial Neural Network (ANN) control. The following section also includes brief description of ATmega328p (Arduino UNO) microcontroller and computational modelling of the above control strategies. Bode plot analysis have also been presented in this chapter for stability analysis.

4.2 Stability Analysis of Multiport Converter

According to the three transfer functions obtained for battery discharging mode of the multiport converter shown in equations(4.1)-(4.3), these are used to design the controller for the MIMO converter. For all three transfer functions, frequency-domain bode plot analysis is obtained by using MATLAB/Simulink software to design the system controllers. System controllers provides desired steady-state error and sufficient phase margin, high bandwidth and high stability. Using A, B, C, and D matrices which are shown in previous chapter and transfer

function matrix G , transfer function of g_{11} is (4.1) shown below. Using MATLAB/Simulink software, the open loop bode plot of g_{11} for converter simulation parameters which is shown in table (4.1) is achieved. Bode plot for open loop is shown in Fig. (4.1). Investigating the obtained bode plot, it can be understood that the crossover frequency phase of g_{11} is -178.0° . So, the phase margin is not sufficient and closed loop system is unstable. In order to increase phase margin and improve system stability, various controllers are designed which is discussed later in this chapter. It is obvious that using these controllers will provide system stability.

Table 4.1 Simulation and Experimental parameters

Components	Symbols	Simulation & Experimental parameters
Inductor	L	1.3 mH
Capacitors	C_1	200 μ F
	C_2	200 μ F
Resistors	R_1	100 Ω
	R_2	100 Ω
Voltage Sources	V_{in1}	18 V
	$V_{Battery} (V_{in2})$	24 V
Frequency	f_s	31 kHz

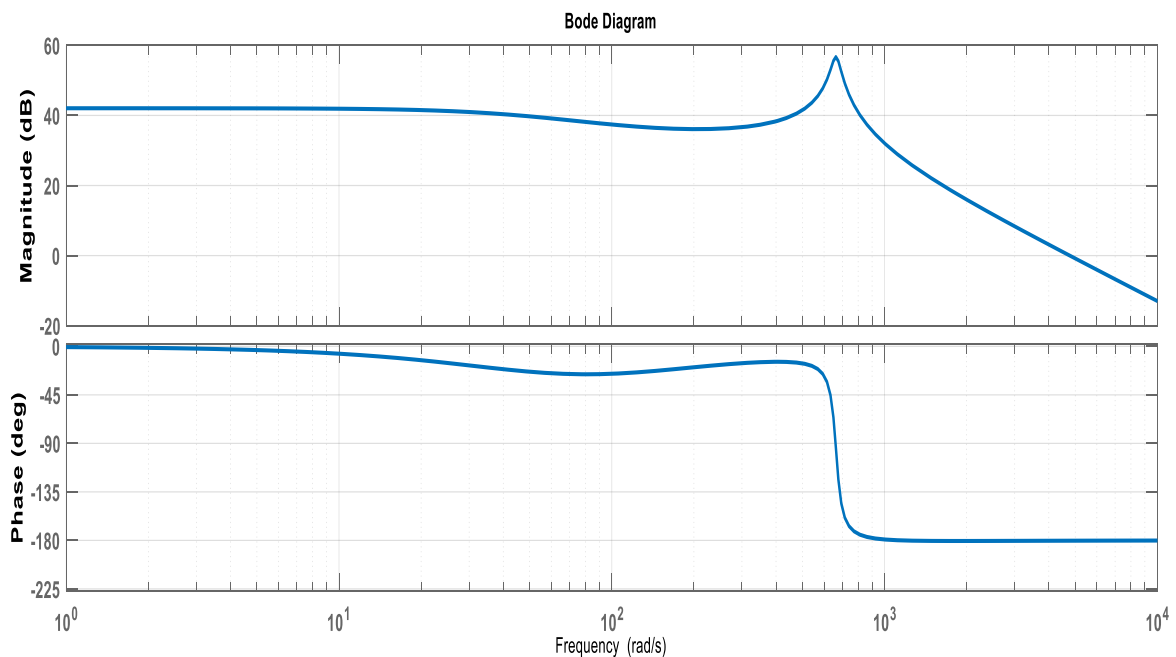


Fig. 4.1 Simulated bode plot of $g_{11}(s)$

$$g_{11} = \frac{\hat{v}_{o1}(s)}{\hat{d}_4(s)}$$

$$= \frac{\left(\frac{V_{o2}(1-D_1)}{LC_1}\right)S + \left(\frac{(1-D_1)V_{o2}}{LR_2C_1C_2} - \frac{(1-D_1)(D_4-1)I_L}{LC_1C_2}\right)}{S^3 + \left(\frac{R_1C_1+R_2C_2}{R_1R_2C_1C_2}\right)S^2 + \left(\frac{L + (1-D_1)^2R_1R_2C_2 + (D_4-1)^2R_1R_2C_1}{LR_1R_2C_1C_2}\right)S + \left(\frac{R_1(1-D_1)^2 + (D_4-1)^2R_2}{LR_1R_2C_1C_2}\right)} \quad (4.1)$$

In Fig. 4.2, bode diagram for g_{22} is shown. It can be observed from the bode plot that the phase margin of g_{22} (in 4.2) is inadequate, so controller is needed to stabilize it. Using the controller reduces dc gain and thus increase steady state error.

$$g_{22} = \frac{\hat{v}_T(s)}{\hat{d}_3(s)}$$

$$= \frac{\left(\frac{V_{in2}-V_{in1}}{L}\right)\left(\frac{(1-D_1)}{C_1} - \frac{(D_4-1)}{C_2}\right)S + \left(\frac{(1-D_1)}{R_2C_1C_2} - \frac{(D_4-1)}{R_1C_1C_2}\right)\left(\frac{V_{in2}-V_{in1}}{L}\right)}{S^3 + \left(\frac{R_1C_1+R_2C_2}{R_1R_2C_1C_2}\right)S^2 + \left(\frac{L + (1-D_1)^2R_1R_2C_2 + (D_4-1)^2R_1R_2C_1}{LR_1R_2C_1C_2}\right)S + \left(\frac{R_1(1-D_1)^2 + (D_4-1)^2R_2}{LR_1R_2C_1C_2}\right)} \quad (4.2)$$

As mentioned in previous chapter, the current I_{in2} (from battery) is controlled from S_1 . So, accordingly inductor current is controlled and its transfer function is shown in (4.3). Bode plot of g_{33} is shown in Fig. 4.3. Phase margin is seen to be inadequate, as a result system is stable but dc gain is low. So, in order to compensate the system, controller design is necessary.

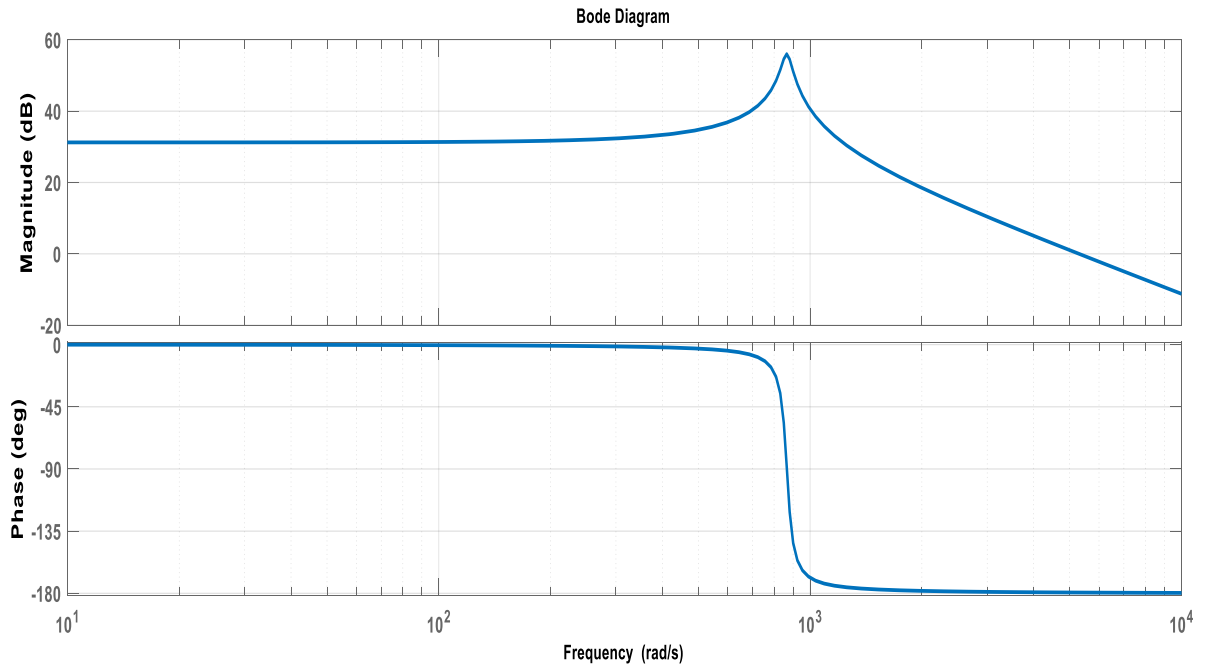


Fig. 4.2 Simulated bode plot of $g_{22}(s)$

$$\begin{aligned}
g_{33} &= \frac{i_b(s)}{\hat{d}_1(s)} \\
&= \frac{\left(\frac{V_{o1} - D_3}{L}\right)S^2 + \left(\frac{D_3 V_{o1}}{L}\left(\frac{1}{R_1 C_1} + \frac{1}{R_2 C_2}\right) + \frac{I_L(1-D_1)D_3}{LC_1}\right)S + \left(\frac{D_3 V_{o1}}{LR_1 R_2 C_1 C_2} + \frac{I_L(1-D_1)D_3}{LR_1 R_2 C_1 C_2}\right)}{S^3 + \left(\frac{R_1 C_1 + R_2 C_2}{R_1 R_2 C_1 C_2}\right)S^2 + \left(\frac{L + (1-D_1)^2 R_1 R_2 C_2 + (D_4 - 1)^2 R_1 R_2 C_1}{LR_1 R_2 C_1 C_2}\right)S + \left(\frac{R_1(1-D_1)^2 + (D_4 - 1)^2 R_2}{LR_1 R_2 C_1 C_2}\right)} \quad (4.3)
\end{aligned}$$

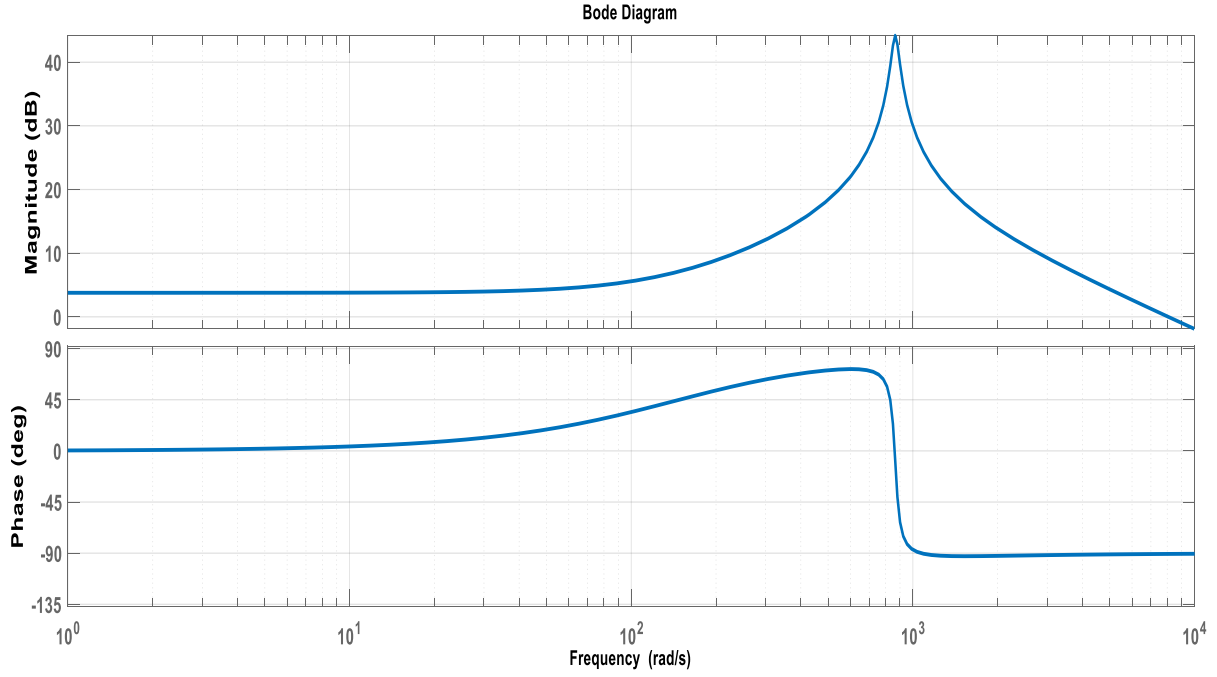


Fig. 4.3 Simulated bode plot of $g_{33}(s)$

These bode plots are thus required to design controllers. The controllers helps to increase gain and tends to stabilize the system.

4.3 PI controller

Proportional-Integral (PI) controller consists of two components i.e. proportional and integral gain parts. This is generally used to establish the system stability and to reduce steady state error. The integral part helps in attaining the desired setpoint diminishing the value of steady state error. The control signal generated from the PI controller is determined using the weighted sum of:

$$u(t) = K_p e(t) + K_I \int_0^t e(\tau) d\tau \quad (4.4)$$

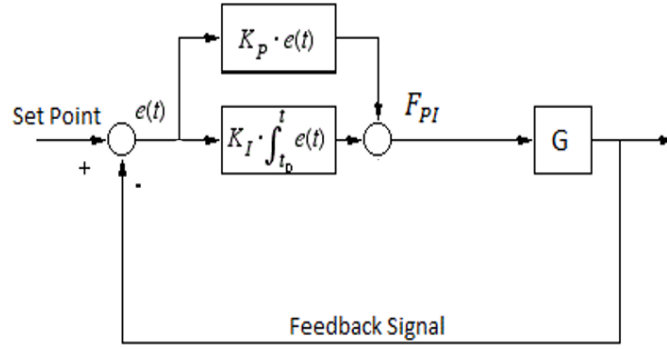


Fig. 4.4: PI Controller configuration

where K_p ,and K_I are all non-negative, denoting the coefficients for the proportional and integral terms, respectively, and $e(t)$ denotes the error signal generated from difference evaluated between setpoint and actual sensed output voltage. The K_p and K_I values obtained from controller design are 50 and 0.8 respectively. The implementation flowchart for PI controller is shown in fig. 4.6.

4.4 PID controller

Proportional–Integral–Derivative (PID) controllers has wide range of applications. These are designed mainly using frequency response and on the hypothesis of linearity. Therefore, they work well if this hypothesis is close to the actual behaviour of the system. If not so, performance tends to deteriorate. It helps to improve transient response as well as steady state response of the MIMO converter.

The actual response of a PID-controlled system depends on how close the linear model represents the actual behaviour of the real system. A PID controller continuously evaluate error (difference between setpoint and sensed output feedback voltage) and generate control signal in our case pwm is generated. The controller attempts to minimize the error over time by adjustment of a control variable, such as the output voltage, to a new value determined by a weighted sum:

$$u(t) = K_p e(t) + K_I \int_0^t e(\tau) d\tau + K_D \frac{de(t)}{dt} \quad (4.5)$$

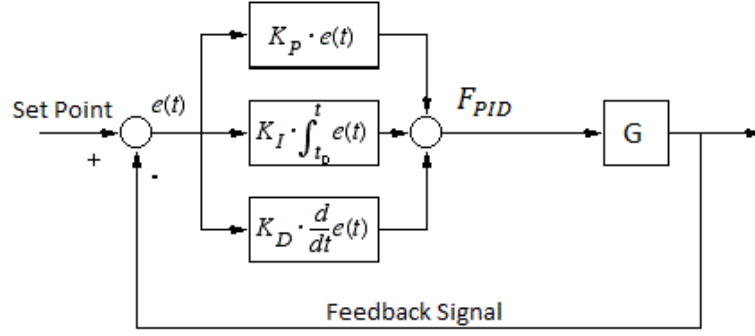


Fig. 4.5: PID Controller configuration

where K_P , K_I , and K_D all non-negative, denote the coefficients for the proportional, integral, and derivative terms, respectively, $e(t)$ is error signal and G is a LTI model with transfer function configuration. From the output the output voltages are sensed back as feedback and error signal is generated which finally result in obtaining the duty ratio for the switches. The K_P , K_I and K_D values obtained from controller design are 50, 0.8 and 0.1 respectively. The implementation flowchart for PID controller is shown in fig. 4.6.

4.5 FOPID controller

The simplest form of fractional order PID (FOPID) controller is the $PI^\lambda D^\mu$ controller, having an integrator of order λ and a differentiator of order μ here λ and μ can be any real numbers. The control signal $u(t)$ can be expressed in the time domain as

$$u(t) = K_P e(t) + K_I D^{-\lambda} e(t) + K_D D^\mu e(t) \quad (4.6)$$

where K_P , K_I , and K_D all non-negative, denote the coefficients for the proportional, integral, and derivative terms, respectively, and $e(t)$ is error signal. By selecting $\lambda=1$ and $\mu=1$, a conventional PID controller is obtained whereas by setting $\lambda=1$ and $\mu=0$, and $\lambda=0$ and $\mu=1$ respectively corresponding classical PI and PD controllers can be recovered. All these can be termed as special cases of FOPID controllers. The K_P , K_I and K_D values obtained from controller design are 50, 0.874 and 0.631 respectively. The λ is taken as 0.6 and μ as 0.2. The implementation flowchart for FOPID controller is shown in fig. 4.6.

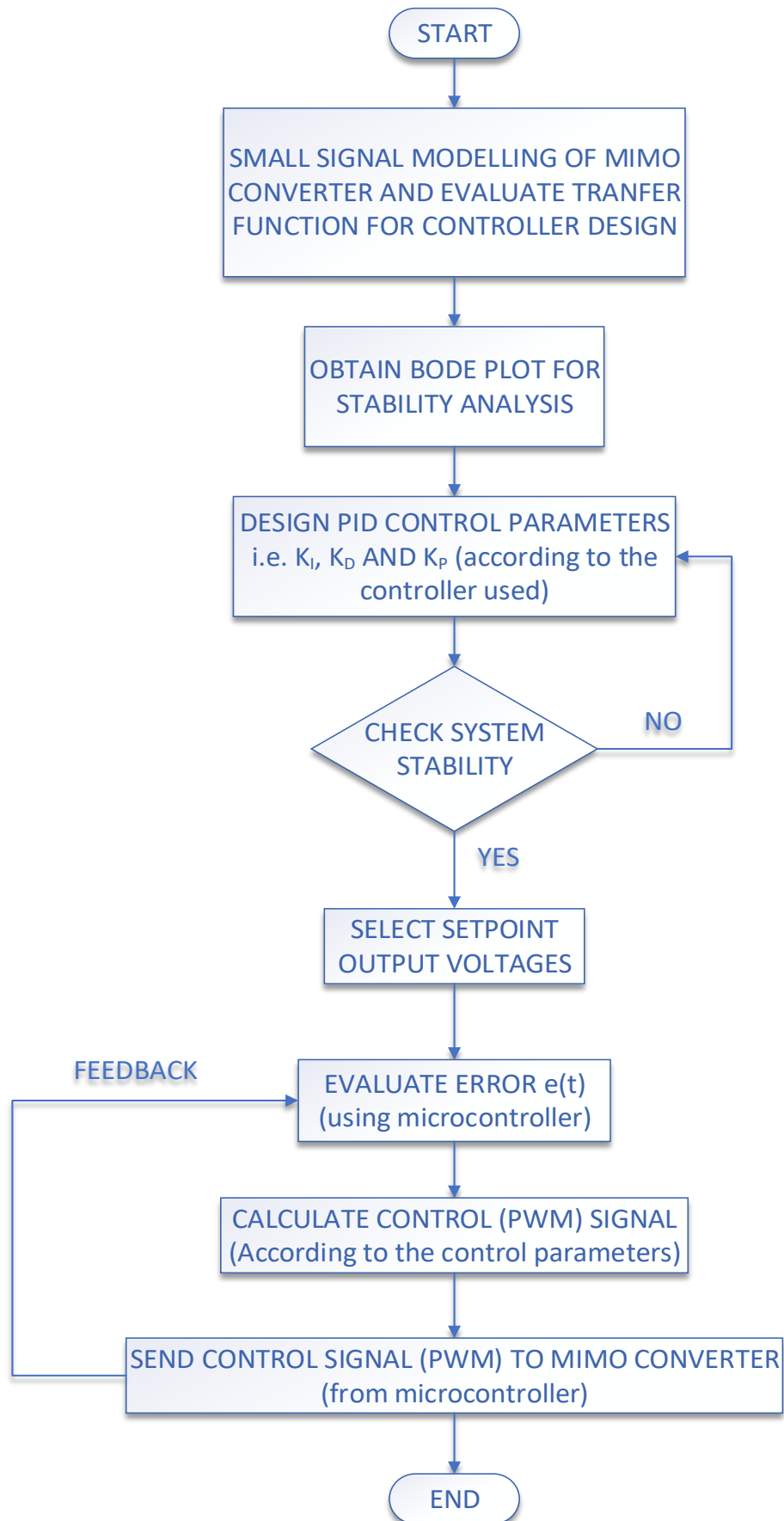


Fig. 4.6 Flowchart for PI, PID and FOPID control implementation

4.6 ANN controller

Artificial Neural Networks are used as a complex structure to solve various control problems. One such problem arises in our converter and it tends to solve it. These networks do not require any detailed information about the system. They intake a set of input data and target data and using various training algorithms, the network is trained. They learn the input output relationship from training dataset and using backpropagation develop a mathematical model to give a desired output. Now a new validation and testing dataset helps to test the network. Another benefit of ANN is its capability to handle large and complex systems with many consistent parameters. The basic structure of ANN is shown in fig. 4.7. The ANN is implemented using nnstart MATLAB toolbox.

The ANN has various layers termed as input layer, hidden layer and output layer. Here the training of network is done using Levenberg-Marquardt algorithm using 4 inputs and 3 target outputs. Each of the 4 input dataset contains 648 samples and similarly each of the 3 target dataset consists of 648 samples. The hidden layer has 4 nodes and using the training algorithm weights are evaluated. The ANN control implementation flowchart is shown in fig. 4.8.

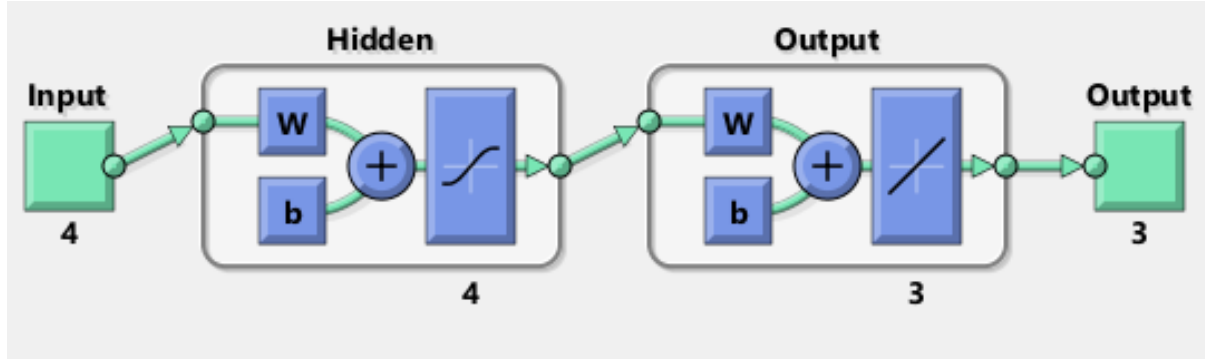


Fig. 4.7 Basic ANN implementation structure.

The W denotes the weight matrix evaluated during training b denotes the bias used to compensate any error between target and actual output. Hidden layer uses bipolar sigmoidal function as activation function whereas output layer uses pure linear function as activation function. Min-max mapping is internally used for the duty constraints i.e. the duty ratio be assured in between 0 and 1.

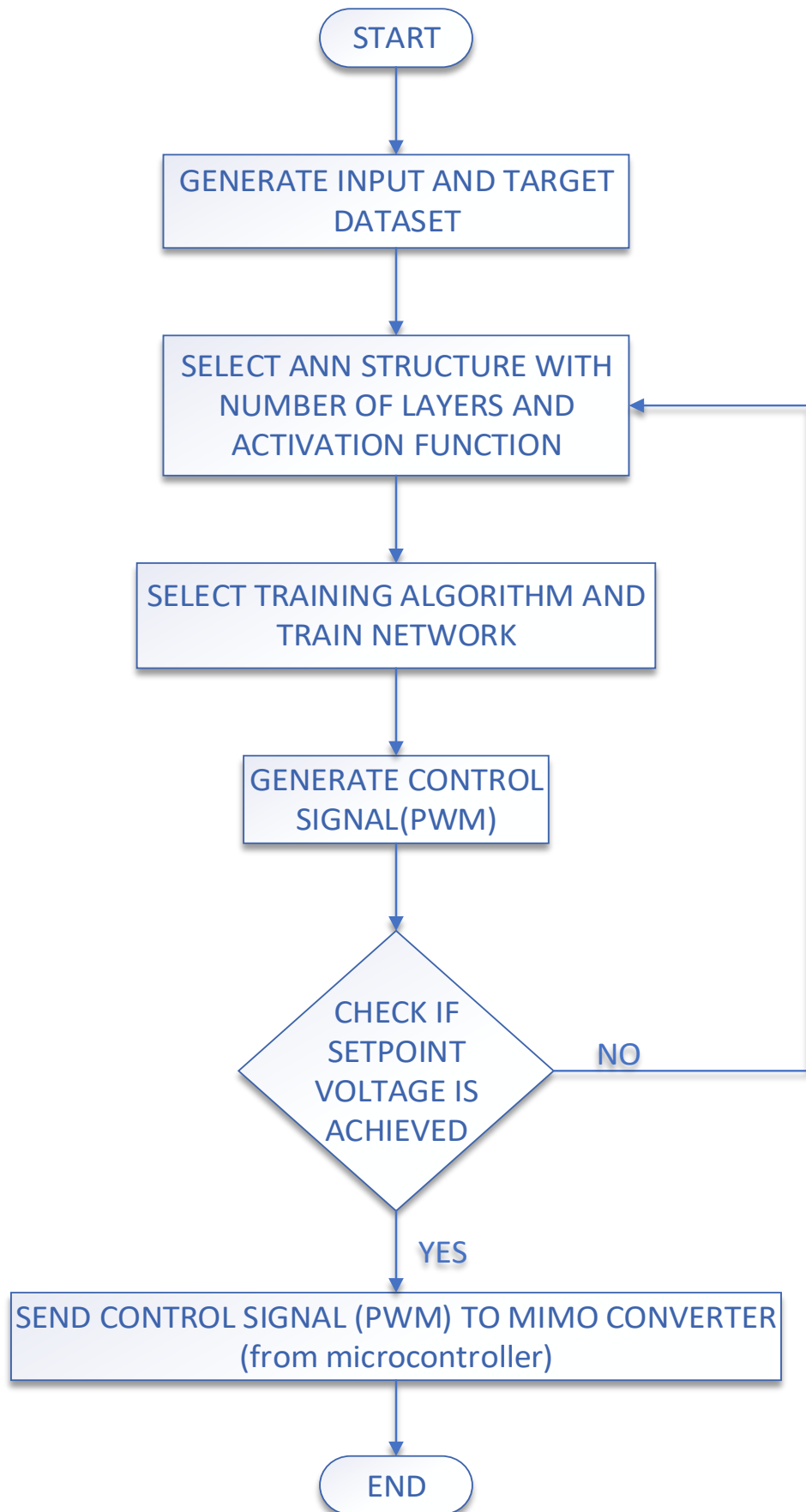


Fig. 4.8 Flowchart for ANN control implementation

4.7 Summary of the Chapter

The various controllers used in the pwm generation for the MIMO converter have been discussed in this chapter. PI, PID and FOPID controllers are discussed with flowchart of working and implementation of these controllers on the MIMO converter. ANN controller is also discussed with flowchart to give an insight of its working with the MIMO converter. The results obtained on implementing these algorithms are discussed in the next chapter.

CHAPTER 5

RESULTS AND DISCUSSIONS

5.1 Introduction

The previous chapters have discussed the mathematical modelling and controller design for the non-isolated multi-input multi-output DC-DC boost converter. Different control strategies were discussed in the previous chapter for implementation on the MIMO converter. These control strategies help to control desired output voltages by providing required duty to the switches. Different controllers have been considered such as PI, PID, FOPID and ANN control.

In this chapter, the numerical investigation of the performance of the different control strategies on MIMO converter are analysed. Effects of input voltage variations and load variations on output load voltages are shown in this chapter. Input voltage V_{in1} is varied for two different V_{in2} values i.e. 12 V and 24 V keeping in mind the constraint that $V_{in1} < V_{in2}$. 12V and 24V signify one battery and two battery system respectively. Load variations are shown in three ways. Each variation of load include decrease in R_1 and R_2 values individually and then decreasing both the loads simultaneously and proportionally. Simulated data and experimental results for input as well as load variations are compiled to evaluate the performance of the control strategies implemented on MIMO converter. The experimental results are also compared with the simulated data for giving a wider overview of the performance of the MIMO converter. Finally, simulated data and hardware results are individually compared for finding best control strategy considering input variations and load variations. Power and efficiency variation curves are also presented in this chapter.

5.2 Open Loop System

The switches of the non-isolated multi-input multi-output DC-DC boost converter has been subjected to duty cycles of constant value directly feeded from the microcontroller as discussed in the previous chapter. Simulation and experimental results are hereby compiled graphically subjected to input voltage variations, load variations and controller parameter variations.

5.2.1 Performance of Open Loop on Input Variations

The performance of the non-isolated multi-input multi-output DC-DC boost converter in open loop subjected to input variations is discussed in this section. Duty ratio of each switch is

provided through the microcontroller. Input voltage V_{in1} is varied keeping V_{in2} as 12 V and 24 V respectively. Load R_1 and R_2 are kept at 100Ω each.

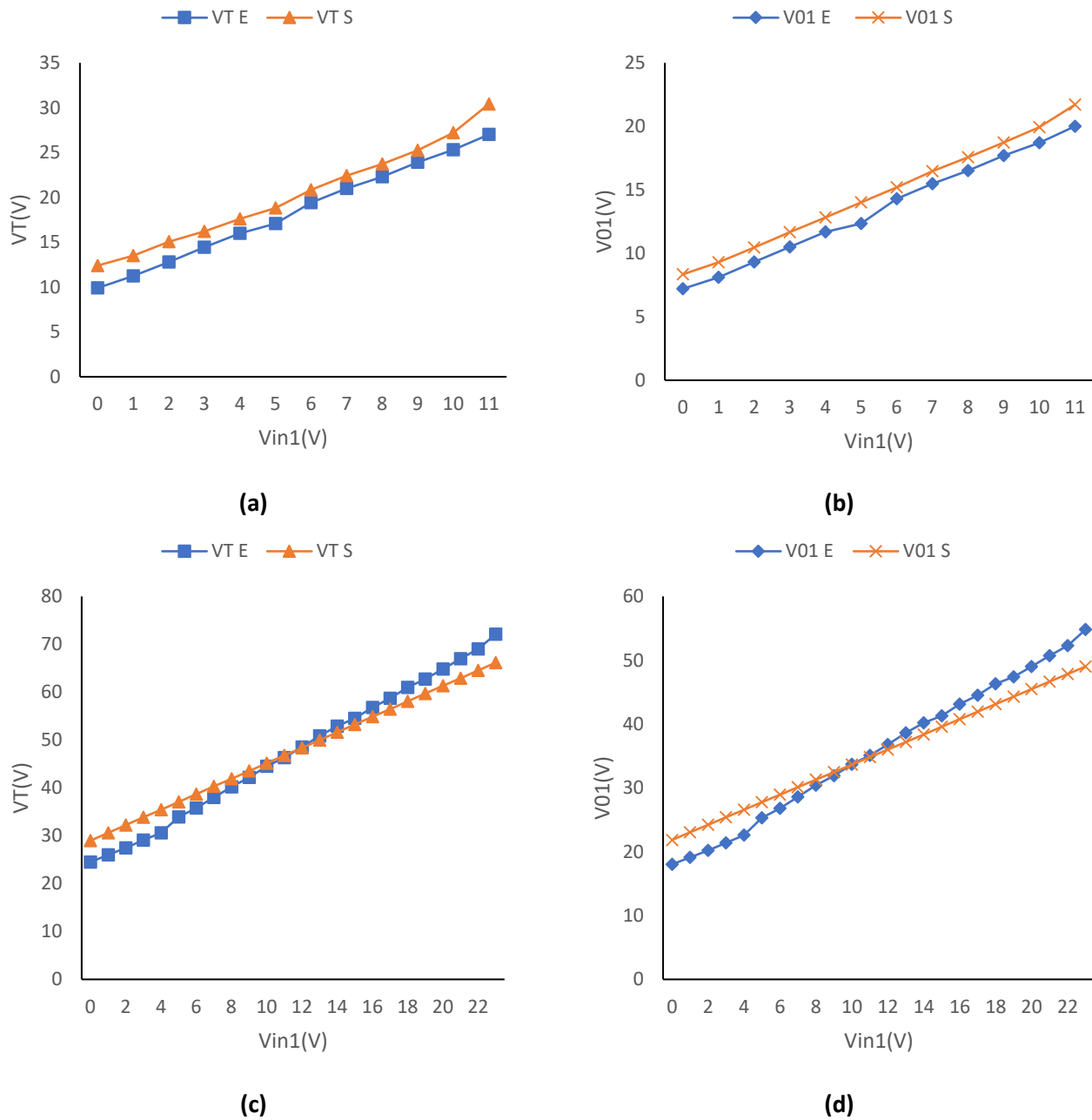


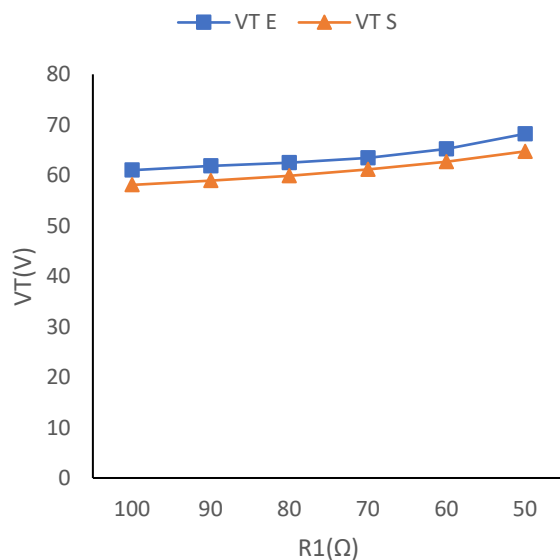
Fig. 5.1 Simulated vs experimental results of open loop system for (a) V_T (b) V_{01} (c) V_T and (d) V_{01} with input voltage variations keeping V_{in2} as 12V and 24V respectively.

Fig. 5.1 shows output voltage variation as input voltage (V_{in1}) is varied. Fig. 5.1(a-b) shows output voltage variation for 12V battery as V_{in2} . In open loop, as the input voltage is increasing from 0 to 11V (keeping in mind the constraint $V_{in1} < V_{in2}$) output voltages keep on increasing since duty ratios are constant. V_T increases from 12.4 V to 30.4V in simulation whereas experimental results show increase in V_T from 9.9V to 27V. V_{01} increases from 8.34V to 21.7V

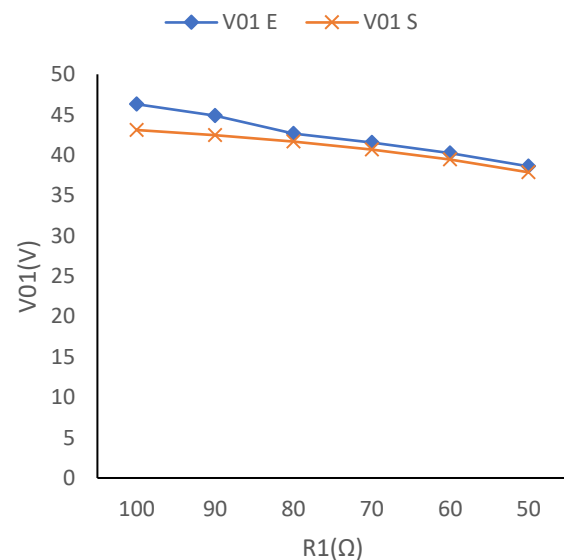
for simulation while experimental results show its variation from 7.2V to 20V. Fig. 5.1(c-d) shows output voltage variation for 24V battery as V_{in2} . In open loop, as the input voltage is increasing from 0 to 23V (keeping in mind the constraint $V_{in1} < V_{in2}$) output voltages keep on increasing. V_T increases from 28.99 V to 66.16V in simulation whereas experimental results show increase in V_T from 24.52V to 72.1V. V_{01} increases from 21.84V to 49.01V for simulation while experimental results show its variation from 18.02V to 54.8 V. The experimental results show slight variation from simulation data resulting due to drop in internal resistance of each component used.

5.2.2 Performance of Open Loop on Load Variations

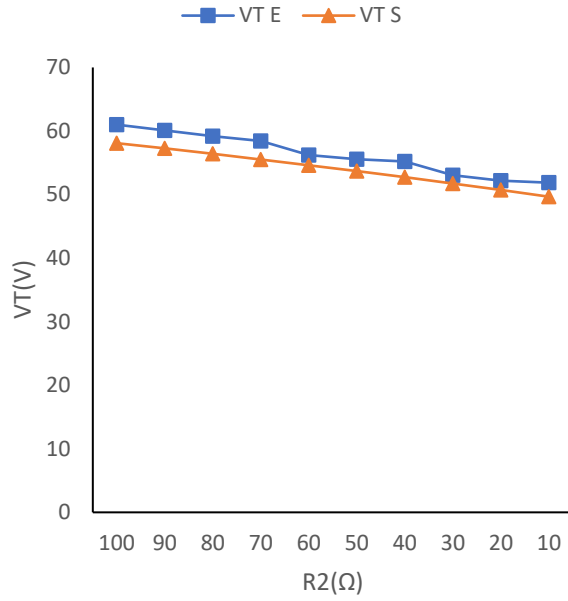
The performance of the non-isolated multi-input multi-output DC-DC boost converter in open loop subjected to load variations is discussed in this section. Duty ratio of each switch is provided through the microcontroller. The load variations are performed in three parts. Firstly, load R_1 is varied and results are accumulated. Then load R_2 is varied and data is collected. Finally, both the loads R_1 and R_2 are varied simultaneously and proportionally. During the whole procedure of simulation and experimental data acquisition, the input voltages V_{in1} and V_{in2} are kept at 18V and 24V respectively. The loads R_1 and R_2 varies from 100Ω to 10Ω with a difference of 10Ω each.



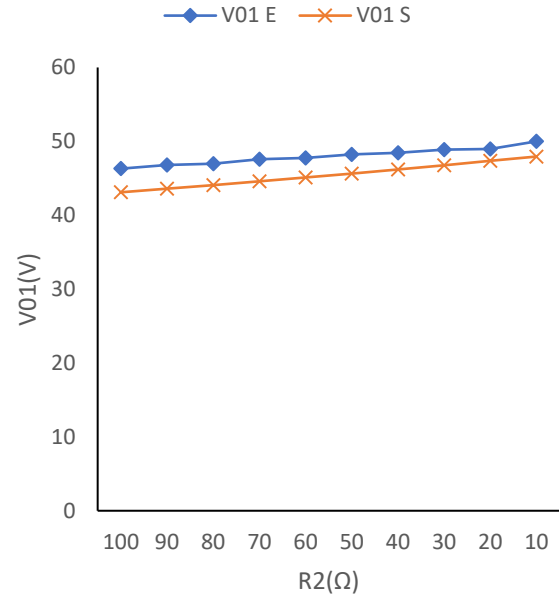
(a)



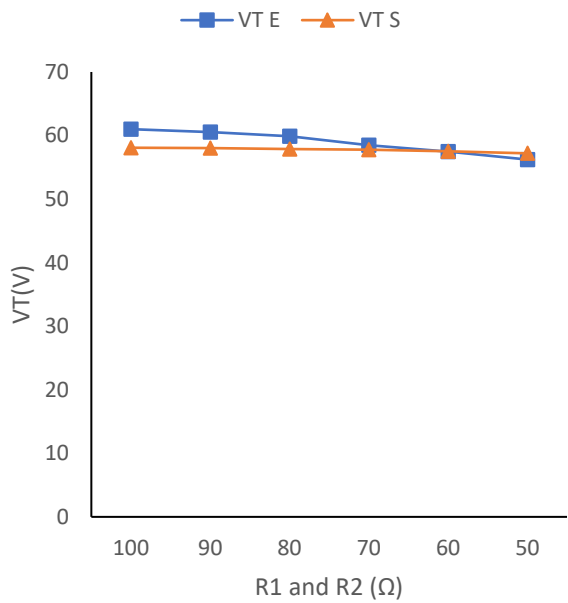
(b)



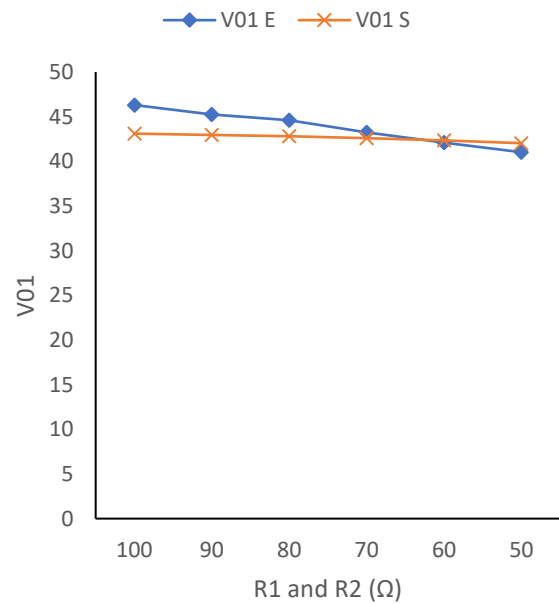
(c)



(d)



(e)

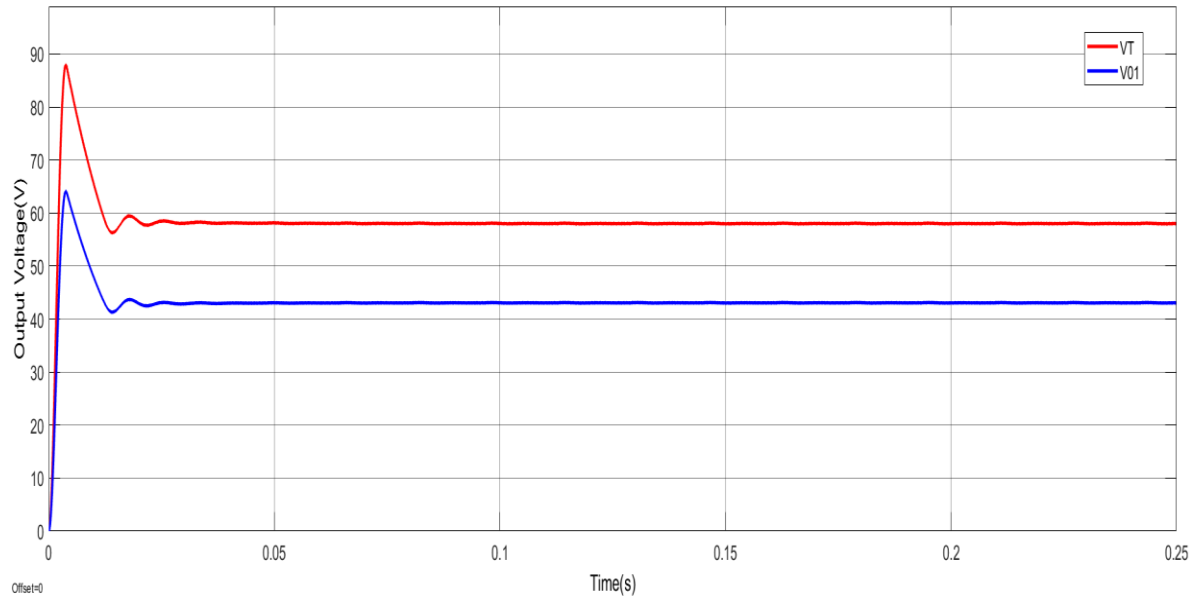


(f)

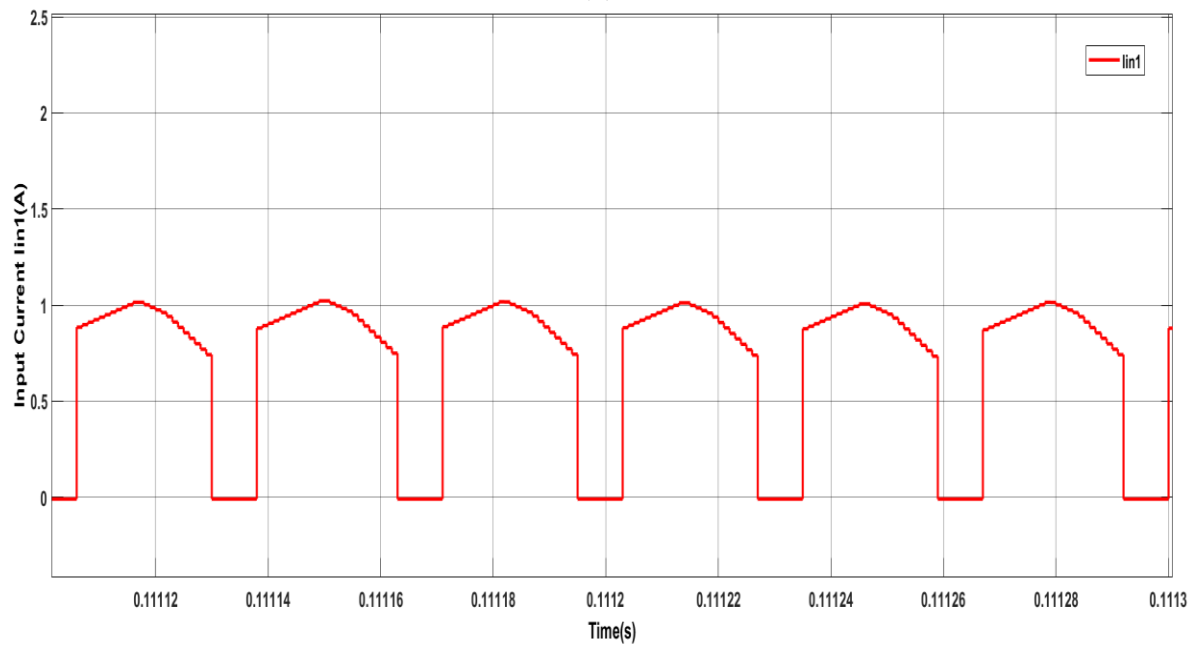
Fig. 5.2 Simulated vs experimental results of open loop system for (a) V_T (b) V_{01} (c) V_T (d) V_{01} (e) V_T and (f) V_{01} with load resistance variations.

Fig. 5.2 shows output voltage variation as load resistance is varied. Fig. 5.2(a-b) shows output voltage variation with change in load resistance R_1 from 100Ω to 10Ω with an interval of 10Ω . In open loop, as R_1 value decreases, V_T increases whereas V_{01} decreases continuously. Fig. 5.2(c-d) shows output voltage variation with change in load resistance R_2 from 100Ω to 10Ω with an interval of 10Ω . In open loop, as R_2 value decreases, V_T decreases whereas V_{01} increases continuously. Fig. 5.2(e-f) shows output voltage variation with change in load resistance R_1 and R_2 simultaneously and proportionally from 100Ω to 10Ω with an interval of

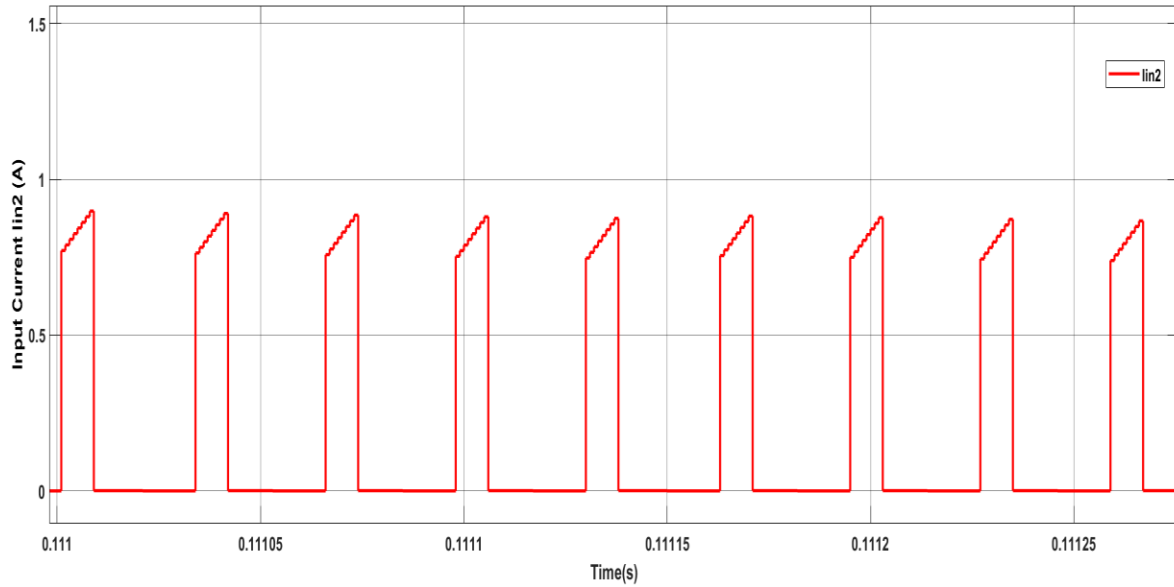
10 Ω . In open loop, as R_1 and R_2 value decreases, V_T decreases as well as V_{O1} also decreases continuously. The experimental results show slight variation from simulation data resulting due to drop in internal resistance of each component used.



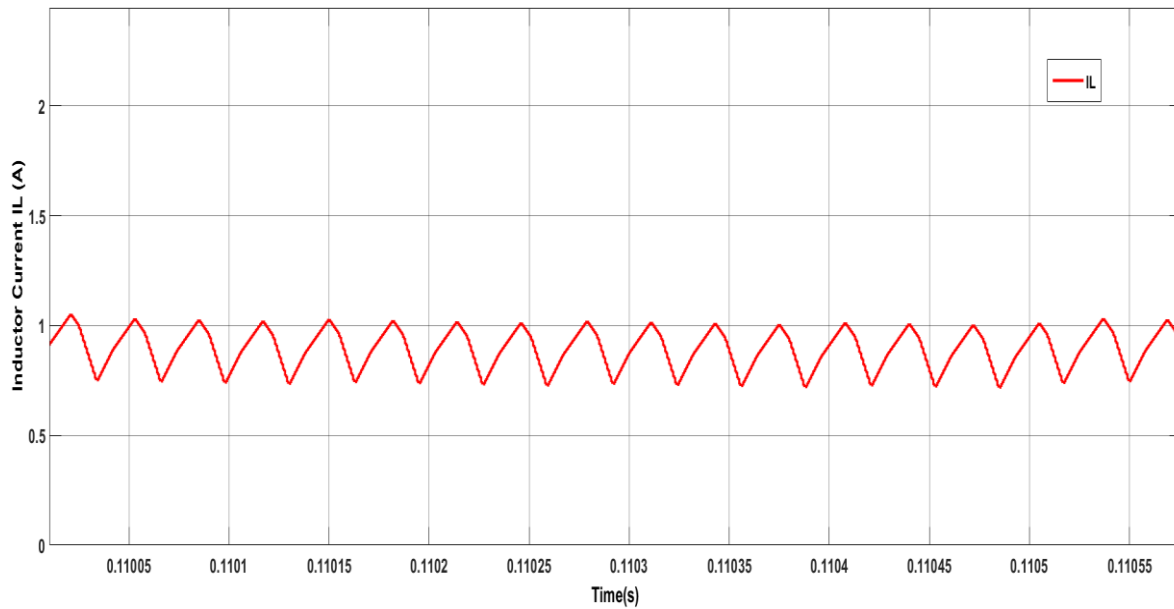
(a)



(b)



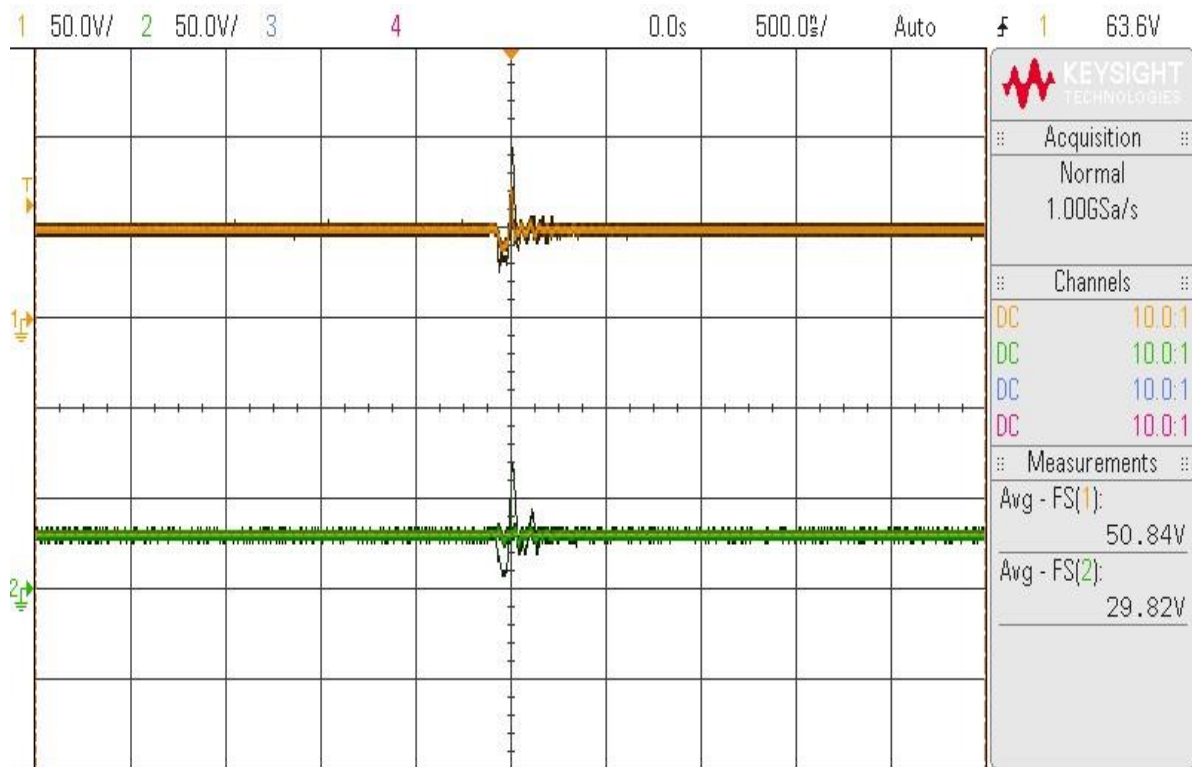
(c)



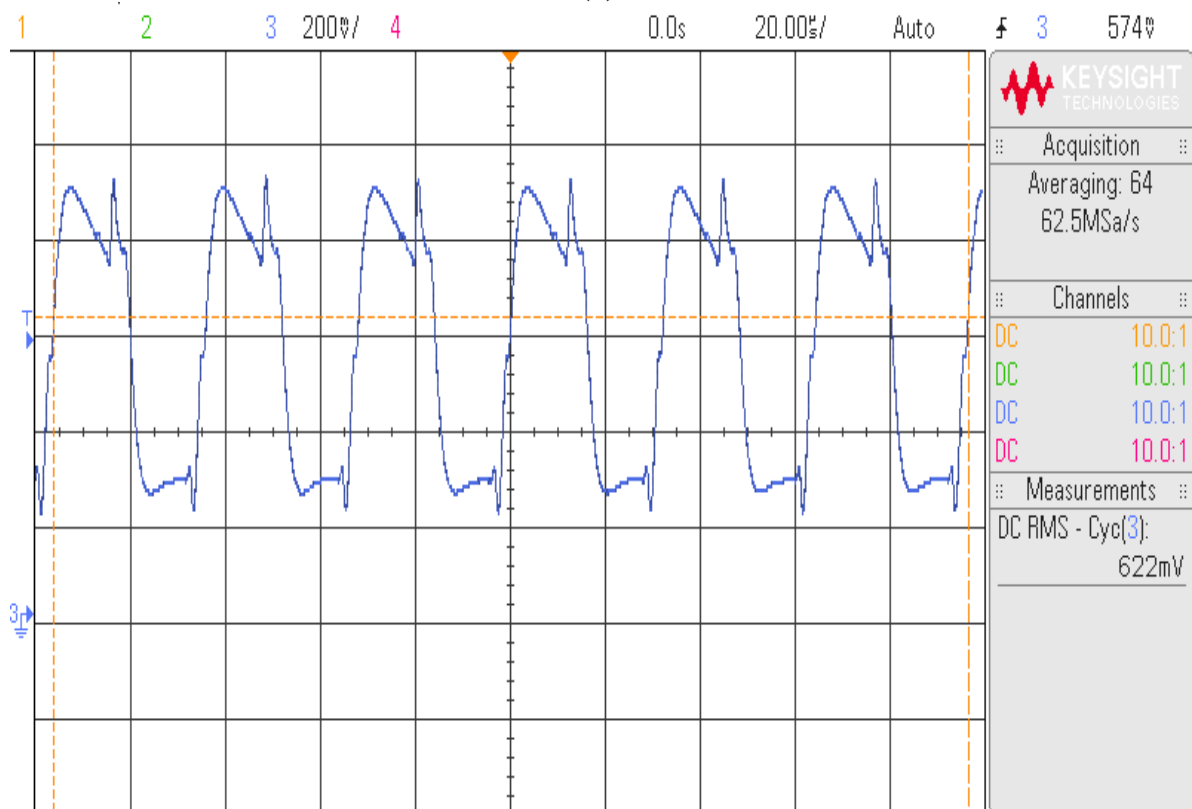
(d)

Fig. 5.2.1 Simulated results for open loop of (a) Output Voltages (V_T and V_{01}) (b) Input Current I_{in1} (c) Input Current I_{in2} and (d) Inductor Current I_L

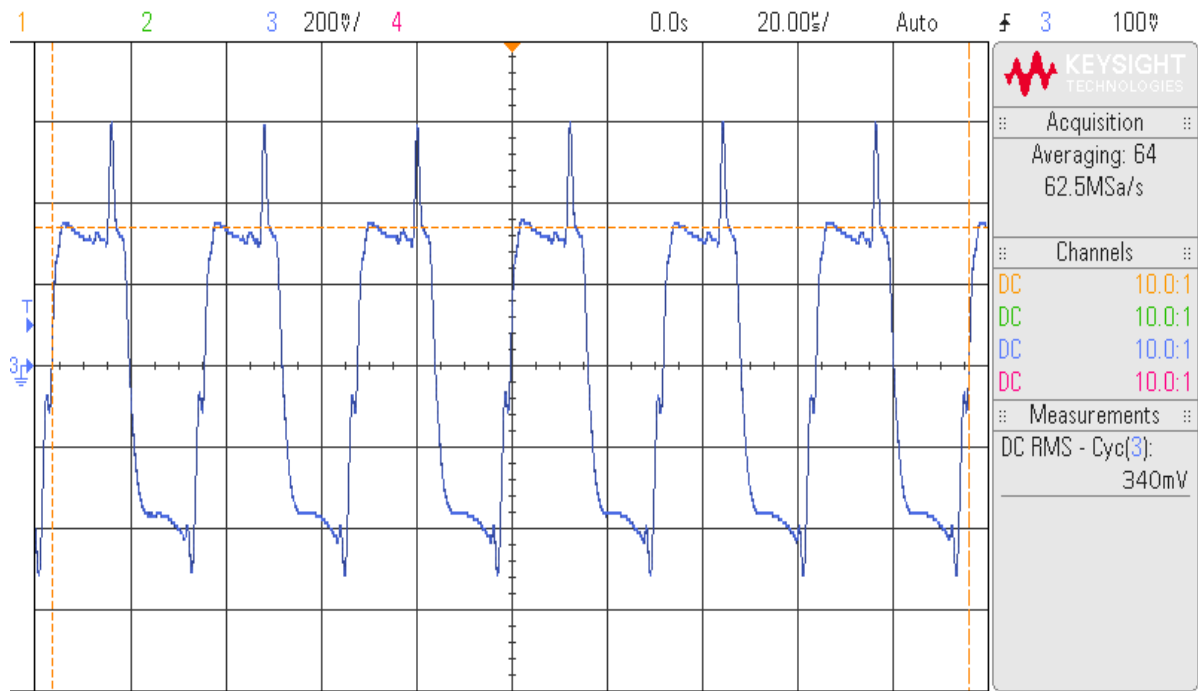
Fig. 5.2.1 shows simulated results obtained using MATLAB environment. Fig. 5.2.1(a) shows output voltage waveforms, Fig. 5.2.1(b-c) indicates input current waveforms from sources V_{in1} and V_{in2} respectively. 5.2.1(d) shows the inductor current waveform. The waveforms are established for 18V and 24V as input sources respectively with 100Ω resistance at load. The average I_{in1} value is 0.5A whereas average I_{in2} value is 0.3A. The inductor average current can be observed as 0.8A.



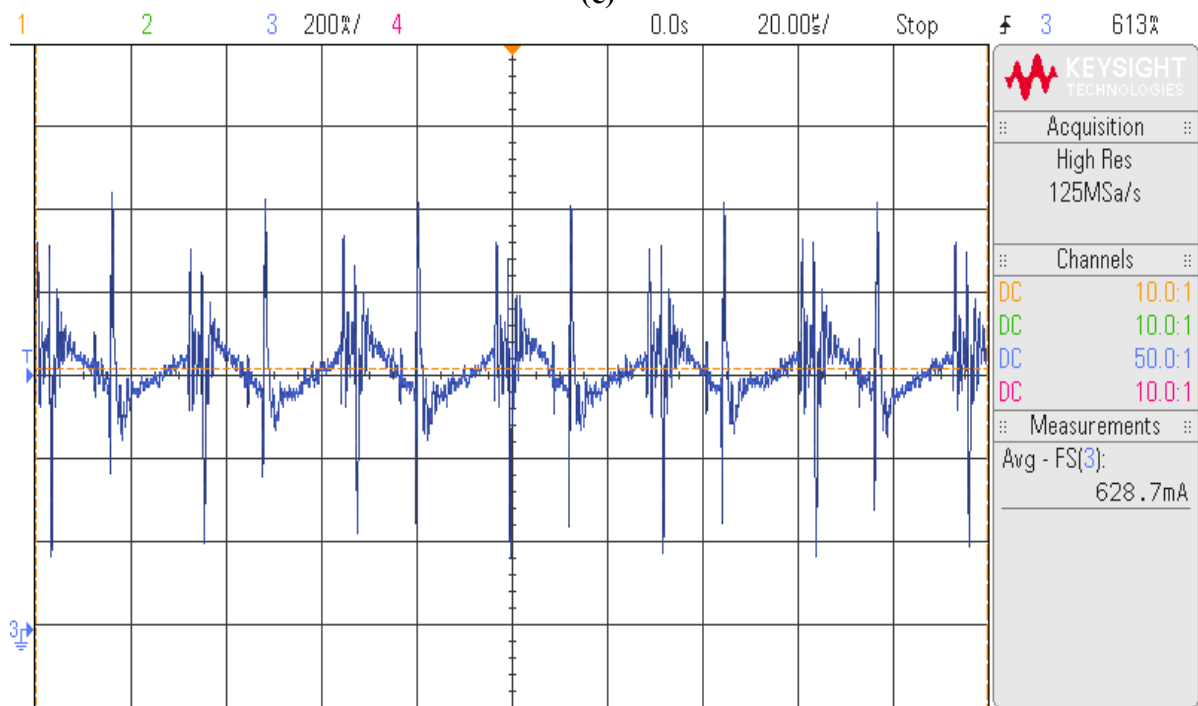
(a)



(b)



(c)



(d)

Fig. 5.2.2 Experimental results for open loop of (a) Output Voltages (V_T and V_{O1}) (b) Input Current I_{in1} (c) Input Current I_{in2} and (d) Inductor Current I_L

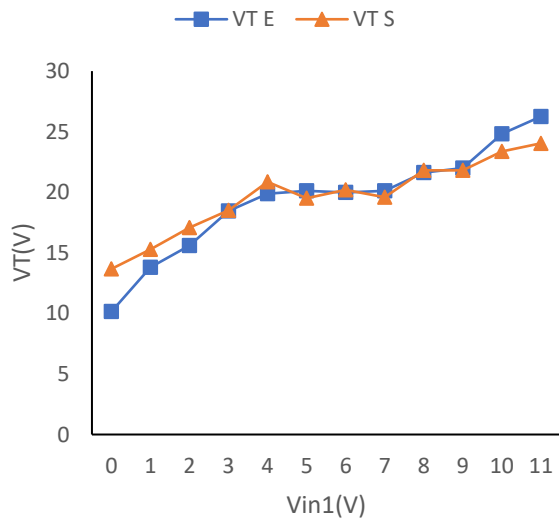
Fig. 5.2.2 shows experimental results obtained from DSO. Fig. 5.2.2(a) shows output voltage waveforms obtained on DSO, Fig. 5.2.2(b-c) indicates input current waveforms from sources V_{in1} and V_{in2} respectively obtained on DSO. 5.2.1(d) shows the inductor current waveform captured on DSO.

5.3 Closed Loop System

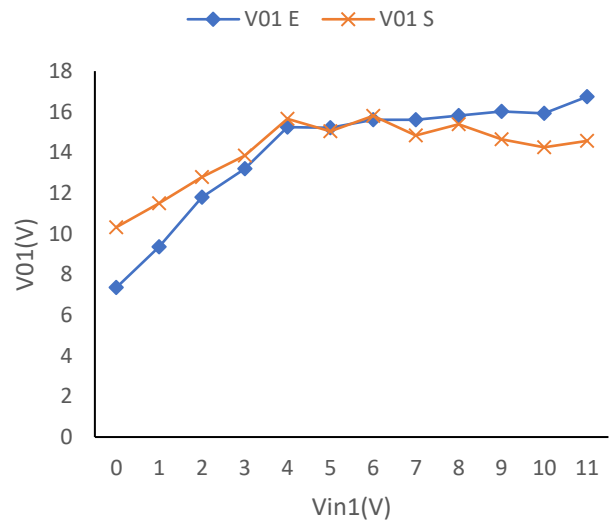
The duty of the switches for the non-isolated multi-input multi-output DC-DC boost converter has been evaluated on basis of the control algorithms viz. PI, PID, FOPID and ANN implemented using the microcontroller and the duty is variable in order to maintain output voltage constant. It is the duty of switch S_1 to maintain V_T , switch S_3 to maintain I_B and switch S_4 to maintain V_{O1} which has been discussed in the previous chapters. Simulated and experimental results are graphically compared subjected to input voltage variations as well as load variations.

5.3.1 Performance of PI controller on Input Variations

The performance of the non-isolated multi-input multi-output DC-DC boost converter with closed loop PI controller subjected to input variations is discussed in this section. Duty ratio of each switch is evaluated using the control algorithm programmed in the microcontroller. Input voltage V_{in1} is varied keeping V_{in2} as 12V and 24V respectively. Load R_1 and R_2 are kept at 100Ω each.



(a)



(b)

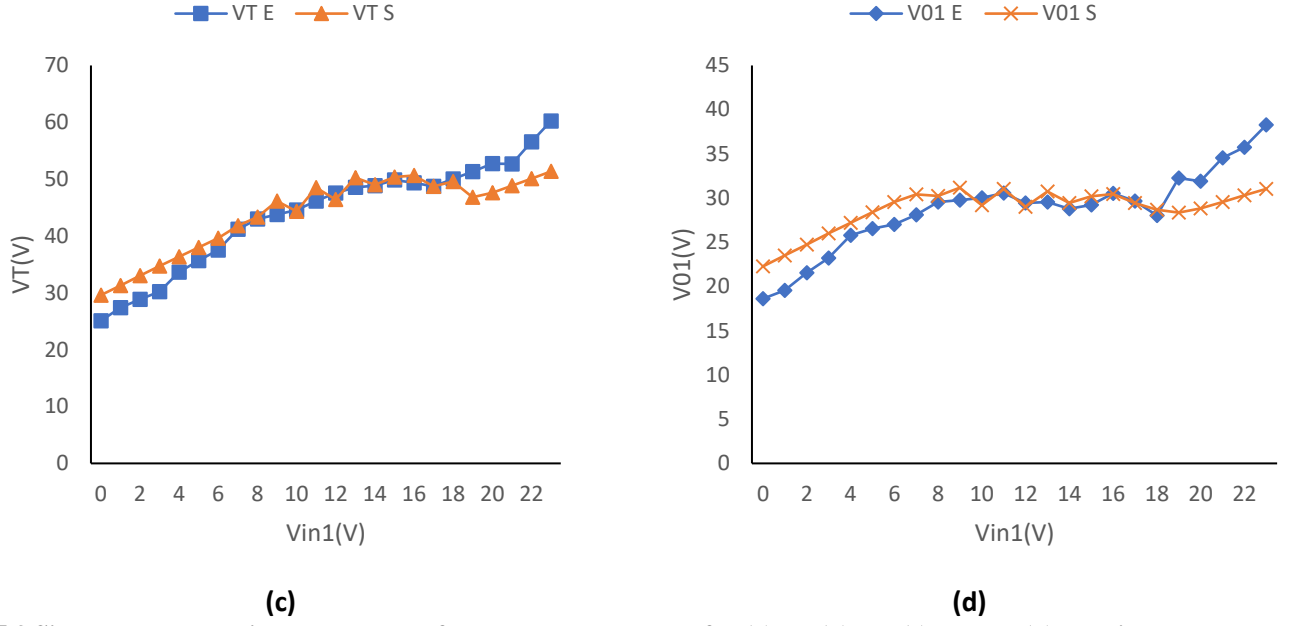


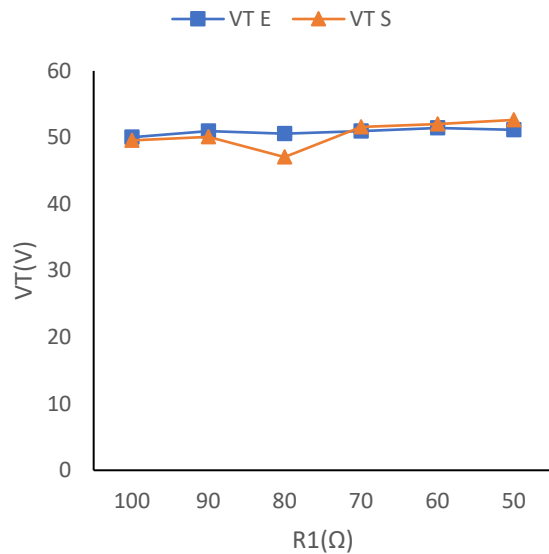
Fig. 5.3 Simulated vs experimental results of closed loop PI control for (a) V_T (b) V_{01} (c) V_T and (d) V_{01} with input voltage variations keeping V_{in2} as 12V and 24V respectively.

Fig. 5.3 shows output voltage variation as input voltage (V_{in1}) is varied. Fig. 5.3(a-b) shows output voltage variation for 12V battery as V_{in2} . In closed loop PI control, as the input voltage is increasing from 0 to 11V (keeping in mind the constraint $V_{in1} < V_{in2}$) output voltages tries to maintain the desired setpoint voltages. The desired V_T is 20V whereas desired V_{01} is 15V. V_T tries to maintain 20V at output as V_{in1} varies from 3V to 9V in simulation whereas V_{in1} varies from 3V to 9V during experimentation. V_{01} tries to maintain 15V as V_{in1} varies from 3V to 11V in simulation whereas V_{in1} varies from 4V to 10V during experimentation. Fig. 5.3(c-d) shows output voltage variation for 24V battery as V_{in2} . Using PI control, as the input voltage is increasing from 0 to 23V (keeping in mind the constraint $V_{in1} < V_{in2}$) output voltages tries to maintain the desired setpoint voltages. The desired V_T is 50V whereas desired V_{01} is 30V. V_T tries to maintain 50V at output as V_{in1} varies from 11V to 23V in simulation whereas V_{in1} varies from 13V to 21V during experimentation. V_{01} tries to maintain 30V as V_{in1} varies from 5V to 23V in simulation whereas V_{in1} varies from 7V to 20V during experimentation. The constraints of duty ratios make it hard to maintain desired setpoints during initial and final V_{in2} values. Internal resistance of each component also adds to slight variation in simulation and experimental data.

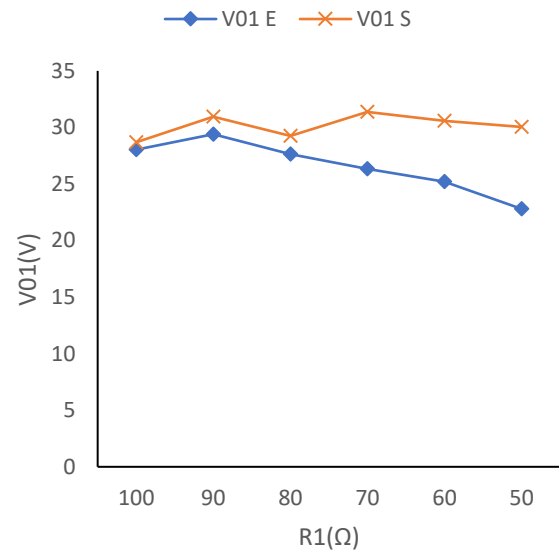
5.3.2 Performance of PI controller on Load Variations

The performance of the non-isolated multi-input multi-output DC-DC boost converter with closed loop PI controller subjected to load variations is discussed in this section. Duty ratio of each switch is evaluated using the control algorithm programmed in the microcontroller. The

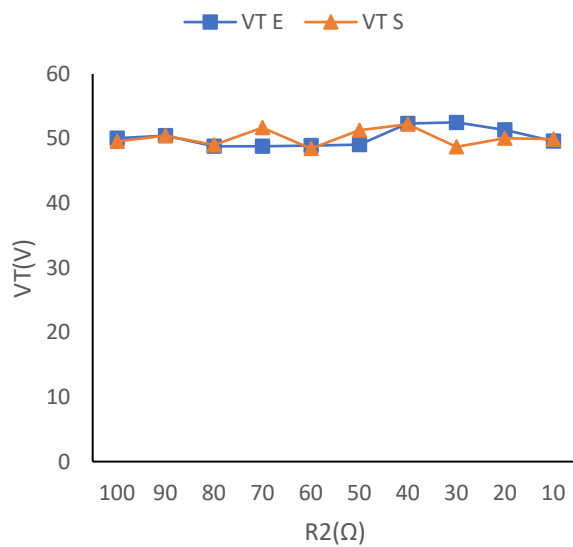
load variations are performed in three parts. Firstly, load R_1 is varied and results are accumulated. Then load R_2 is varied and data is collected. Finally, both the loads R_1 and R_2 are varied simultaneously and proportionally. During the whole procedure of simulation and experimental data acquisition, the input voltages V_{in1} and V_{in2} are kept at 18V and 24V respectively. The loads R_1 and R_2 varies from 100Ω to 10Ω with an interval of 10Ω each.



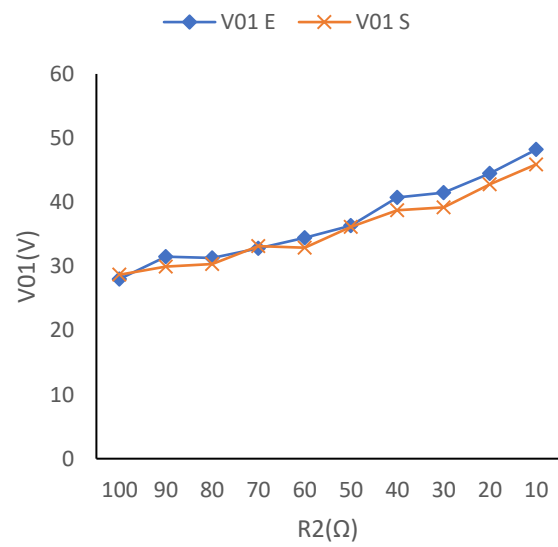
(a)



(b)



(c)



(d)

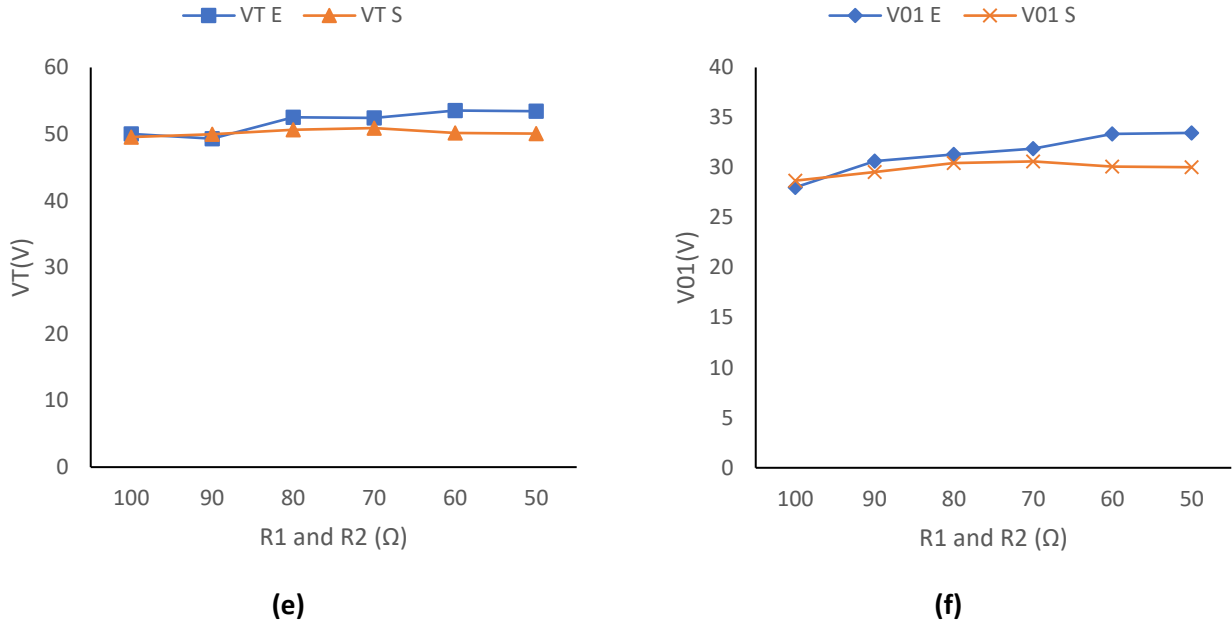


Fig. 5.4 Simulated vs experimental results of closed loop PI control for (a) V_T (b) V_{01} (c) V_T (d) V_{01} (e) V_T and (f) V_{01} with load resistance variations.

Fig. 5.4 shows output voltage variation as load resistance is varied. Fig. 5.4(a-b) shows output voltage variation with change in load resistance R_1 from 100Ω to 10Ω with an interval of 10Ω. In closed loop PI control, as R_1 value decreases, desired V_T and V_{01} i.e. 50V and 30V is maintained respectively. Desired V_T is maintained from 100Ω to 50Ω during simulation whereas from 100Ω to 50Ω during experimentation. Desired V_{01} is maintained from 100Ω to 60Ω during simulation whereas from 100Ω to 50Ω during experimentation. Fig. 5.4(c-d) shows output voltage variation with change in load resistance R_2 from 100Ω to 10Ω with an interval of 10Ω. In closed loop PI control, as R_2 value decreases, desired V_T and V_{01} i.e. 50V and 30V is maintained respectively. Desired V_T is maintained from 100Ω to 10Ω during simulation whereas from 100Ω to 10Ω during experimentation. Desired V_{01} is maintained from 100Ω to 60Ω during simulation whereas from 100Ω to 70Ω during experimentation. Fig. 5.4(e-f) shows output voltage variation with change in load resistance R_1 and R_2 from 100Ω to 10Ω with an interval of 10Ω simultaneously and proportionally. In closed loop PI control, as R_1 and R_2 value decreases, desired V_T and V_{01} i.e. 50V and 30V is maintained respectively. Desired V_T is maintained from 100Ω to 50Ω during simulation whereas from 100Ω to 50Ω during experimentation. Desired V_{01} is maintained from 100Ω to 50Ω during simulation whereas from 100Ω to 50Ω during experimentation. The constraints of duty ratios and inductor saturation point make it hard to maintain desired setpoints during low load resistance values. Internal resistance of each component also adds to slight variation in simulation and experimental data.

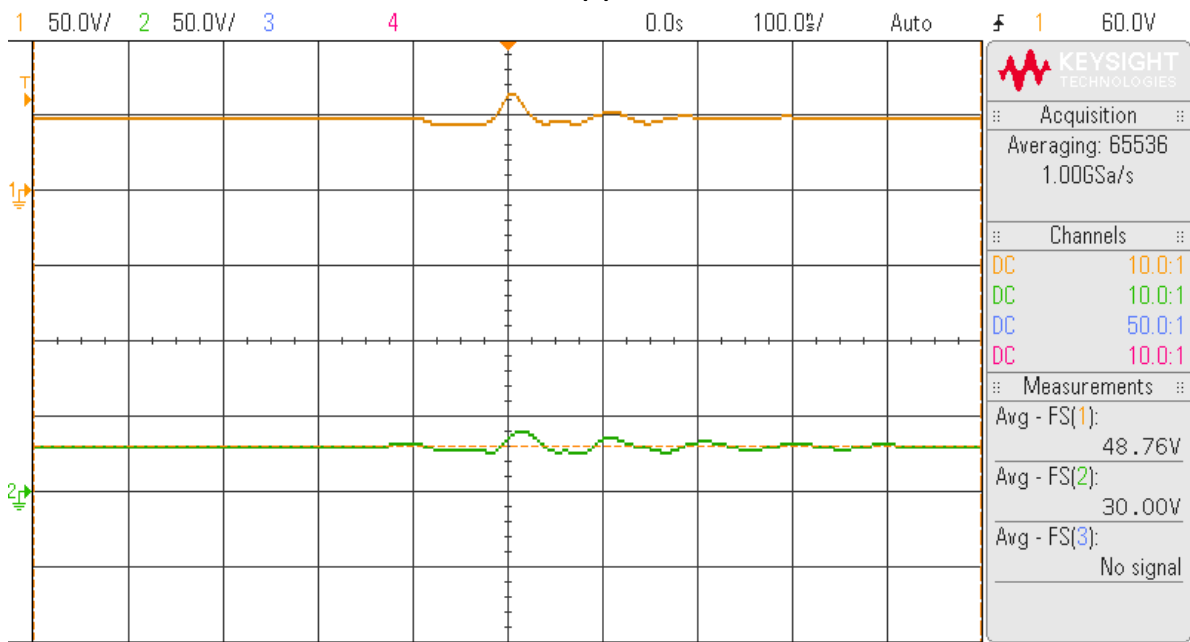
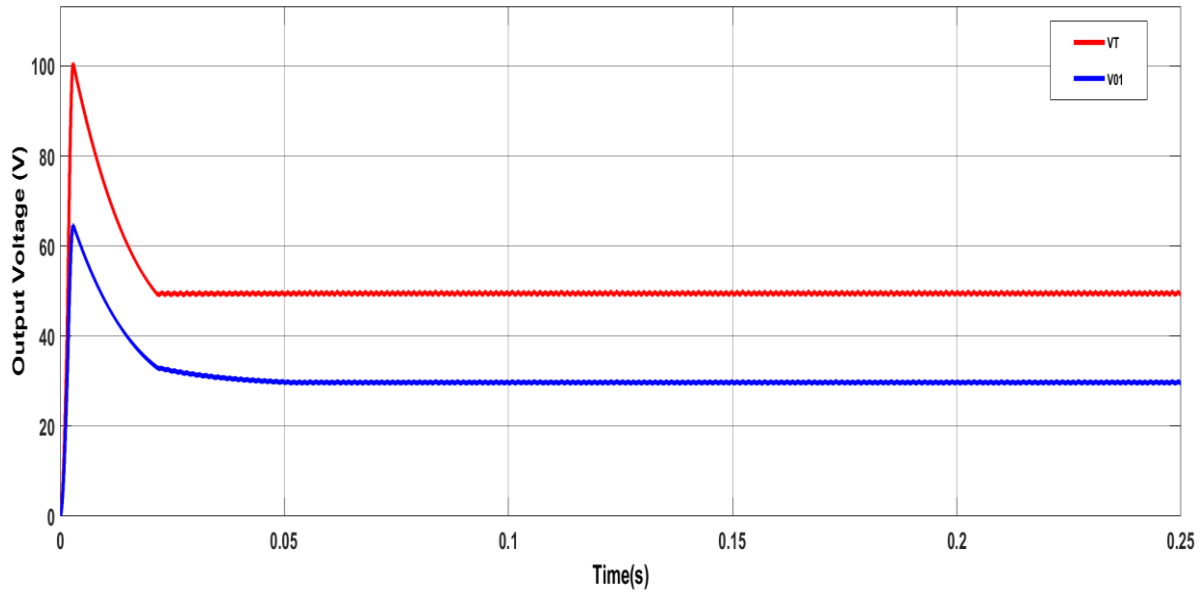


Fig. 5.4.1 Output Voltage (V_T & V_{01}) plot for (a) simulated and (b) experimental results.

Fig. 5.4.1 shows the output voltage waveforms obtained from simulation and experimental results. Fig. 5.4.1(a) shows output voltage waveforms obtained during simulation whereas Fig. 5.4.1(b) indicates output voltage waveform during experimental results obtained on DSO. These waveforms are obtained for PI control strategy implemented on the non-isolated multi-input multi-output DC-DC boost converter. It can be observed during simulation V_T and V_{01} reaches 50V and 30V similar to experimental values i.e. 48.76V and 30.00V respectively. The input voltages V_{in1} and V_{in2} were taken as 18V and 24V respectively and load resistance as 100 Ω each.

5.3.3 Performance of PID controller on Input Variations

The performance of the non-isolated multi-input multi-output DC-DC boost converter with closed loop PID controller subjected to input variations is discussed in this section. Duty ratio of each switch is evaluated using the control algorithm programmed in the microcontroller. Input voltage V_{in1} is varied keeping V_{in2} as 12V and 24V respectively. Load R_1 and R_2 are kept at 100Ω each.

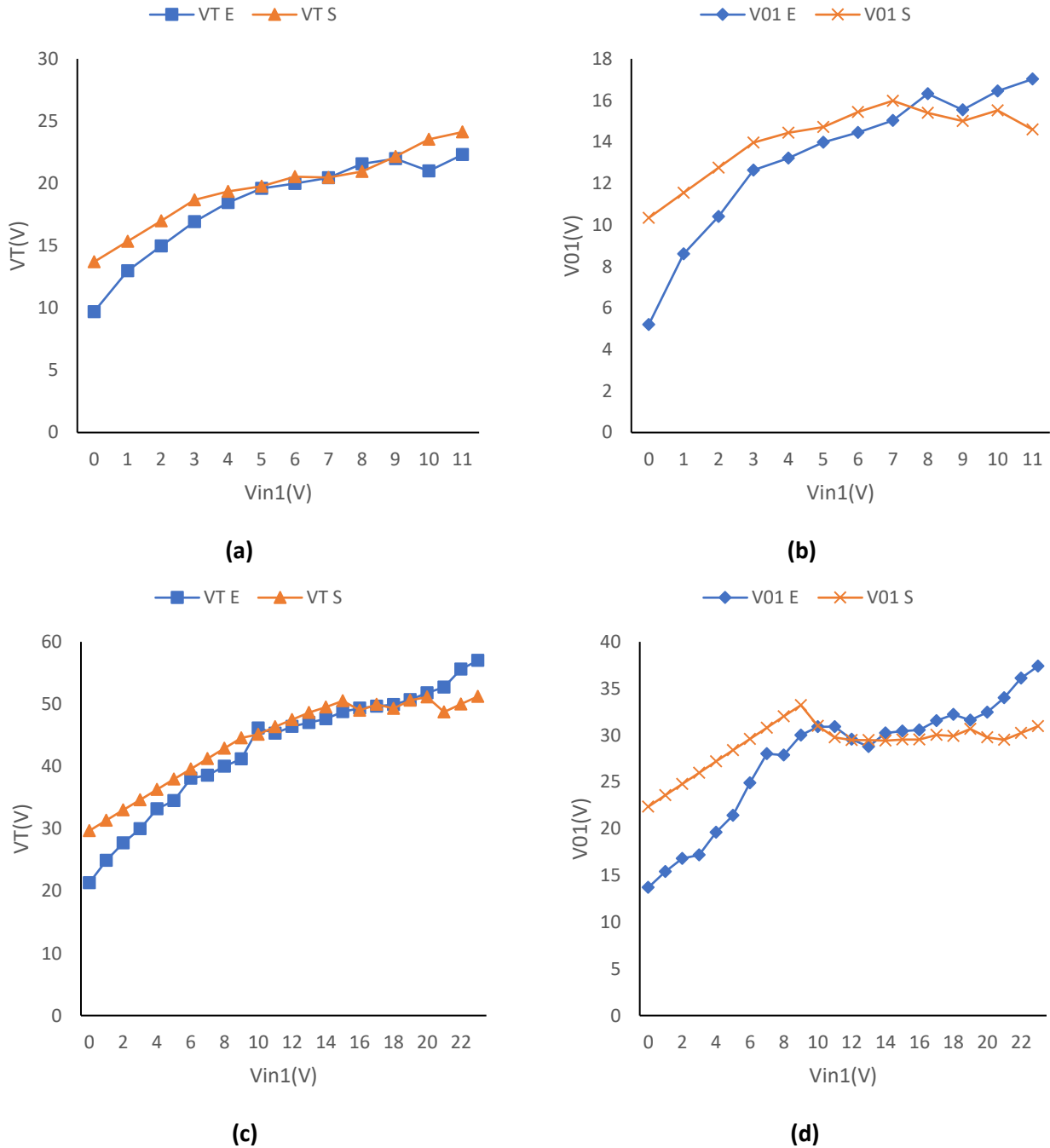


Fig. 5.5 Simulated vs experimental results of closed loop PID control for (a) V_T (b) V_{01} (c) V_T and (d) V_{01} with input voltage variations keeping V_{in2} as 12V and 24V respectively.

Fig. 5.5 shows output voltage variation as input voltage (V_{in1}) is varied. Fig. 5.5(a-b) shows output voltage variation for 12V battery as V_{in2} . In closed loop PID control, as the input voltage is increasing from 0 to 11V (keeping in mind the constraint $V_{in1} < V_{in2}$) output voltages tries to maintain the desired setpoint voltages. The desired V_T is 20V whereas desired V_{01} is 15V. V_T tries to maintain 20V at output as V_{in1} varies from 3V to 9V in simulation whereas V_{in1} varies from 4V to 11V during experimentation. V_{01} tries to maintain 15V as V_{in1} varies from 3V to 11V in simulation whereas V_{in1} varies from 6V to 9V during experimentation.

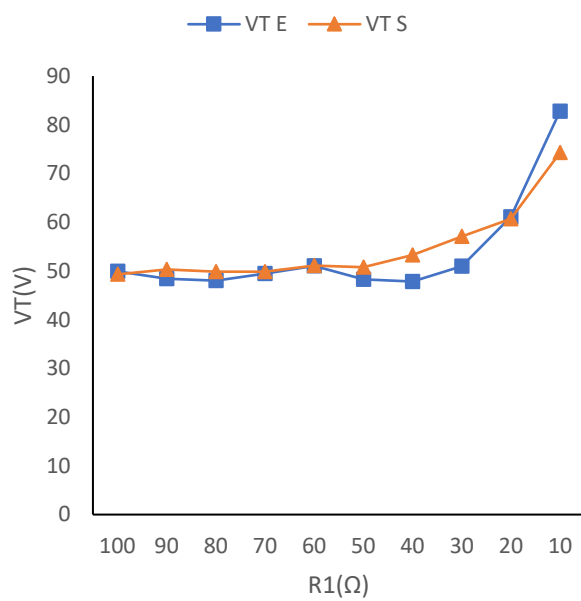
Fig. 5.5(c-d) shows output voltage variation for 24V battery as V_{in2} . Using PID control, as the input voltage is increasing from 0 to 23V (keeping in mind the constraint $V_{in1} < V_{in2}$) output voltages tries to maintain the desired setpoint voltages. The desired V_T is 50V whereas desired V_{01} is 30V. V_T tries to maintain 50V at output as V_{in1} varies from 13V to 23V in simulation whereas V_{in1} varies from 15V to 21V during experimentation. V_{01} tries to maintain 30V as V_{in1} varies from 5V to 23V in simulation whereas V_{in1} varies from 7V to 20V during experimentation.

The constraints of duty ratios make it hard to maintain desired setpoints during initial and final V_{in2} values. Internal resistance of each component also adds to slight variation in simulation and experimental data.

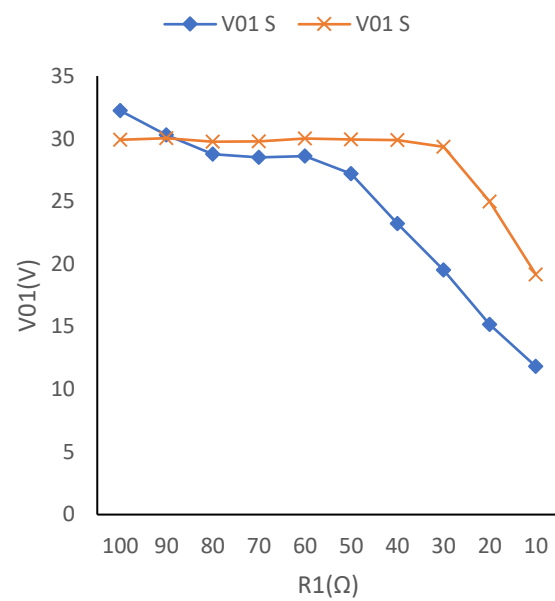
5.3.4 Performance of PID controller on Load Variations

The performance of the non-isolated multi-input multi-output DC-DC boost converter with closed loop PID controller subjected to load variations is discussed in this section. Duty ratio of each switch is evaluated using the control algorithm programmed in the microcontroller. The load variations are performed in three parts. Firstly, load R_1 is varied and results are accumulated. Then load R_2 is varied and data is collected. Finally, both the loads R_1 and R_2 are varied simultaneously and proportionally.

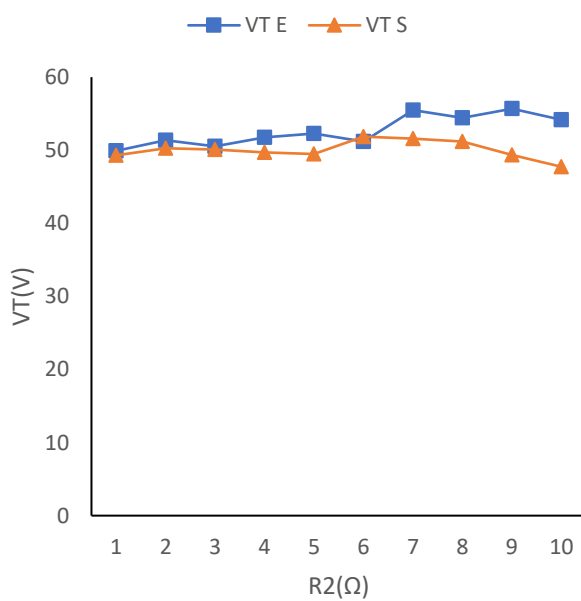
During the whole procedure of simulation and experimental data acquisition, the input voltages V_{in1} and V_{in2} are kept at 18V and 24V respectively. The loads R_1 and R_2 varies from 100Ω to 10Ω with an interval of 10Ω each.



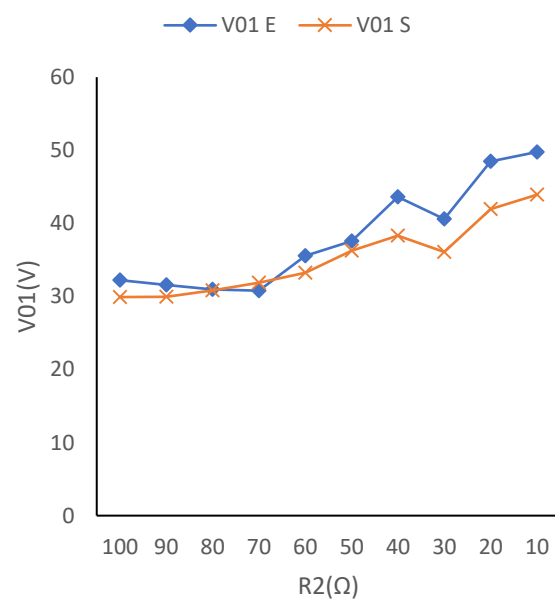
(a)



(b)



(c)



(d)

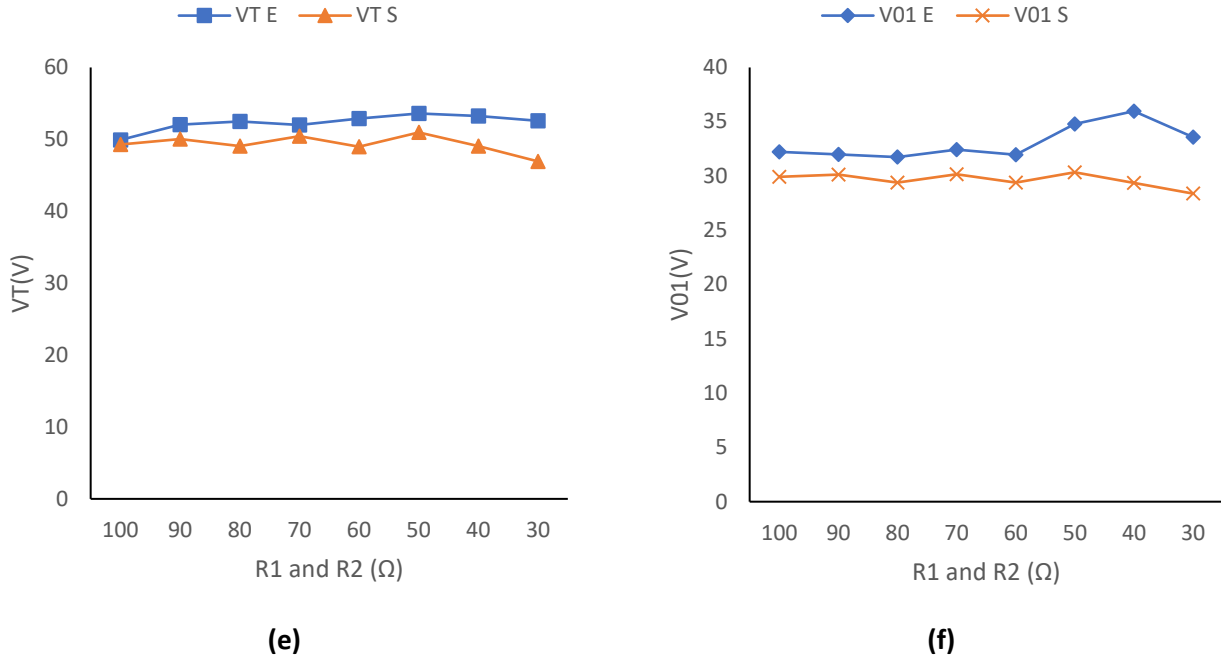


Fig. 5.6 Simulated vs experimental results of closed loop PID control for (a) V_T (b) V_{01} (c) V_T (d) V_{01} (e) V_T and (f) V_{01} with load resistance variations.

Fig. 5.6 shows output voltage variation as load resistance is varied. Fig. 5.6(a-b) shows output voltage variation with change in load resistance R_1 from 100Ω to 10Ω with an interval of 10Ω . In closed loop PID control, as R_1 value decreases, desired V_T and V_{01} i.e. $50V$ and $30V$ is maintained respectively. Desired V_T is maintained from 100Ω to 50Ω during simulation whereas from 100Ω to 30Ω during experimentation. Desired V_{01} is maintained from 100Ω to 30Ω during simulation whereas from 100Ω to 60Ω during experimentation. Fig. 5.6(c-d) shows output voltage variation with change in load resistance R_2 from 100Ω to 10Ω with an interval of 10Ω . In closed loop PID control, as R_2 value decreases, desired V_T and V_{01} i.e. $50V$ and $30V$ is maintained respectively. Desired V_T is maintained from 100Ω to 10Ω during simulation whereas from 100Ω to 50Ω during experimentation. Desired V_{01} is maintained from 100Ω to 60Ω during simulation whereas from 100Ω to 70Ω during experimentation. Fig. 5.6(e-f) shows output voltage variation with change in load resistance R_1 and R_2 from 100Ω to 10Ω with an interval of 10Ω simultaneously and proportionally. In closed loop PID control, as R_1 and R_2 value decreases, desired V_T and V_{01} i.e. $50V$ and $30V$ is maintained respectively. Desired V_T is maintained from 100Ω to 30Ω during simulation whereas from 100Ω to 30Ω during experimentation. Desired V_{01} is maintained from 100Ω to 30Ω during simulation whereas from 100Ω to 50Ω during experimentation. The constraints of duty ratios and inductor saturation point make it hard to maintain desired setpoints during low load resistance values. Internal resistance of each component also adds to slight variation in simulation and experimental data.

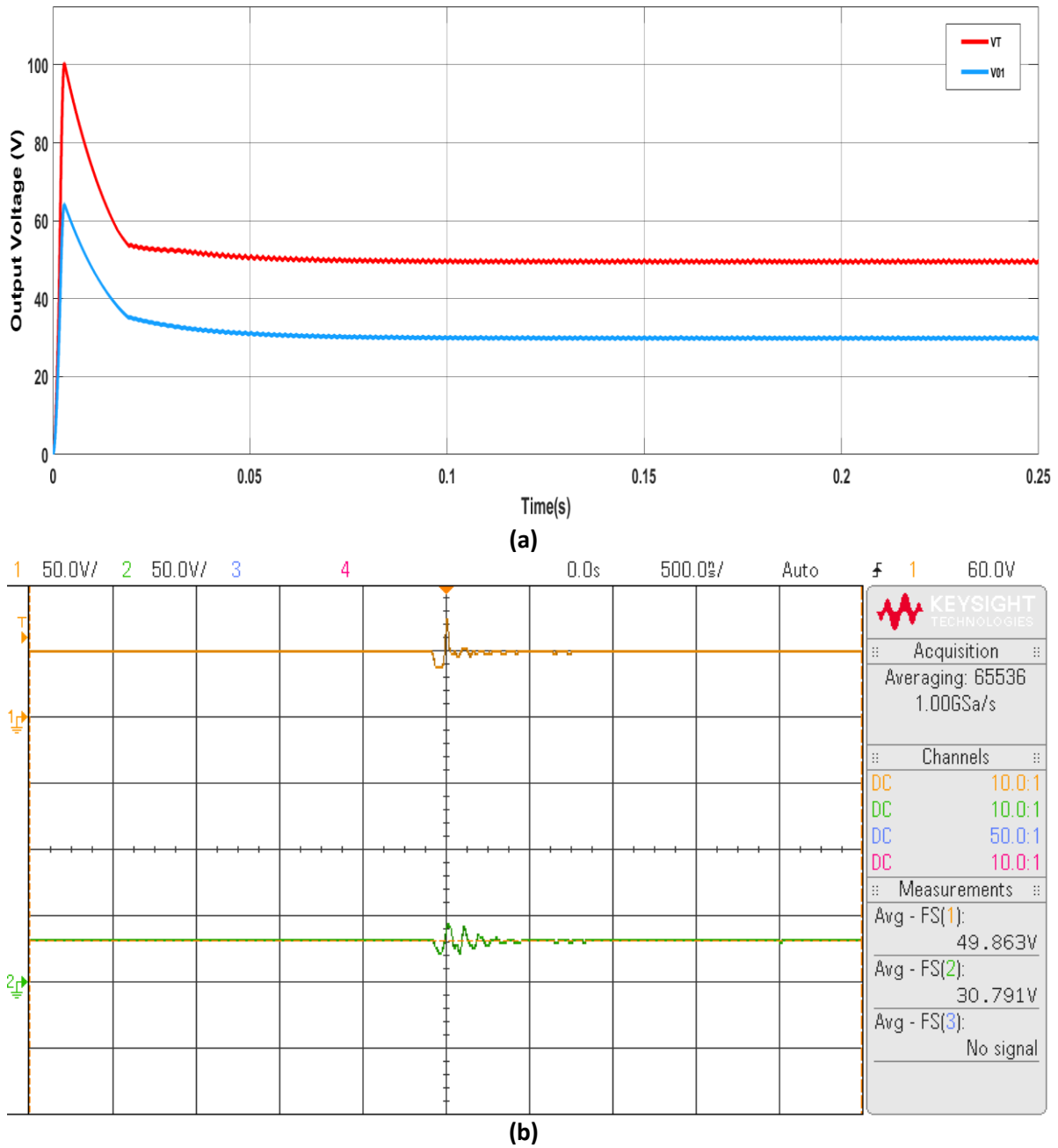


Fig. 5.6.1 Output Voltage (V_T & V_{O1}) plot for (a) simulated and (b) experimental results.

Fig. 5.6.1 shows the output voltage waveforms obtained from simulation and experimental results. Fig. 5.6.1(a) shows output voltage waveforms obtained during simulation whereas Fig. 5.6.1(b) indicates output voltage waveform during experimental results obtained on DSO. These waveforms are obtained for PID control strategy implemented on the non-isolated multi-input multi-output DC-DC boost converter. The simulation results obtained shows output voltages V_T and V_{O1} as 50V and 30V respectively whereas experimental results show 49.863V and 30.791V respectively. The input voltages V_{in1} and V_{in2} were taken as 18V and 24V respectively and load resistance as 100 Ω each.

5.3.5 Performance of FOPID controller on Input Variations

The performance of the non-isolated multi-input multi-output DC-DC boost converter with closed loop FOPID controller subjected to input variations is discussed in this section. Duty ratio of each switch is evaluated using the control algorithm programmed in the microcontroller. Input voltage V_{in1} is varied keeping V_{in2} as 12V and 24V respectively. Load R_1 and R_2 are kept at 100Ω each.

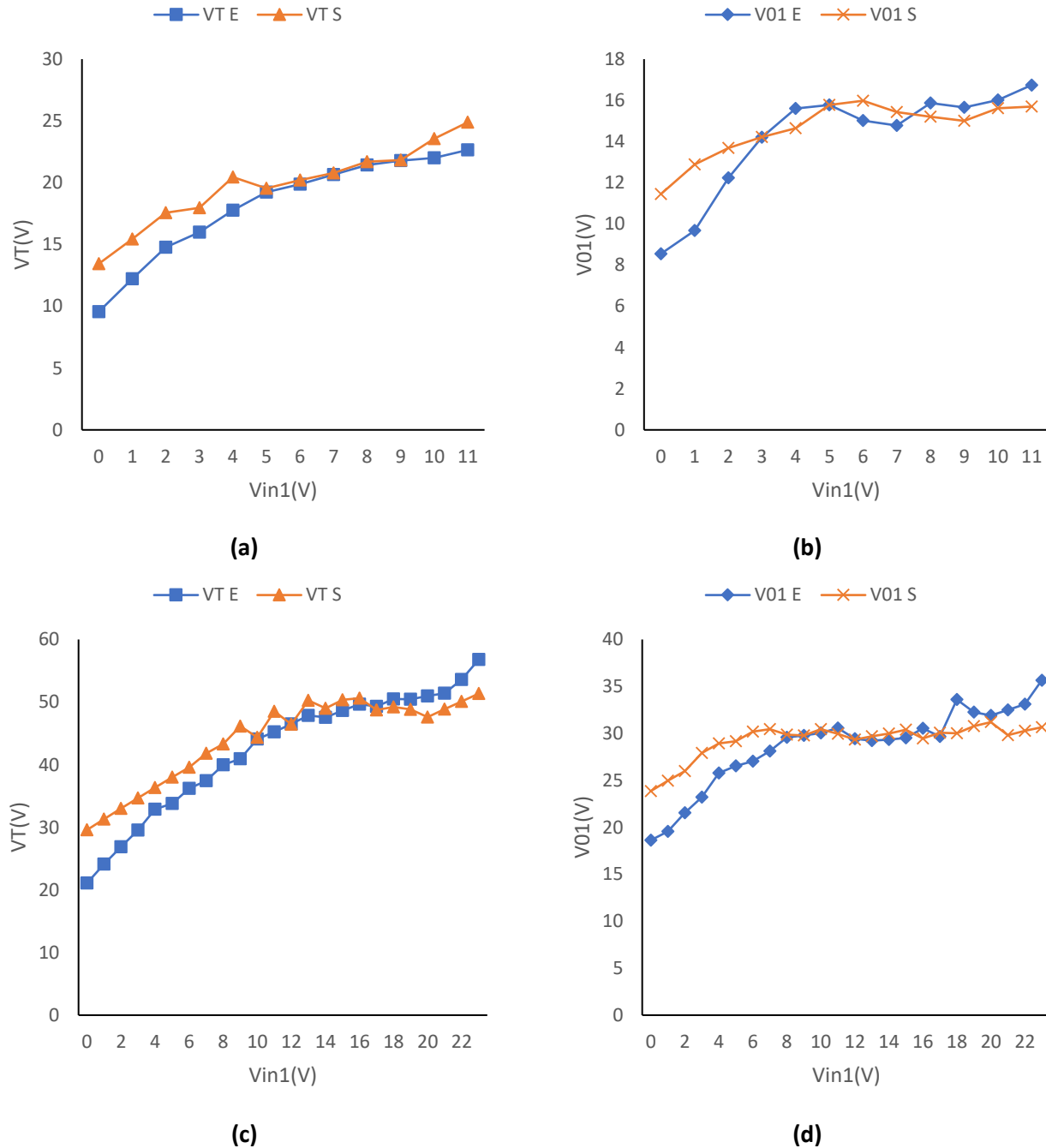
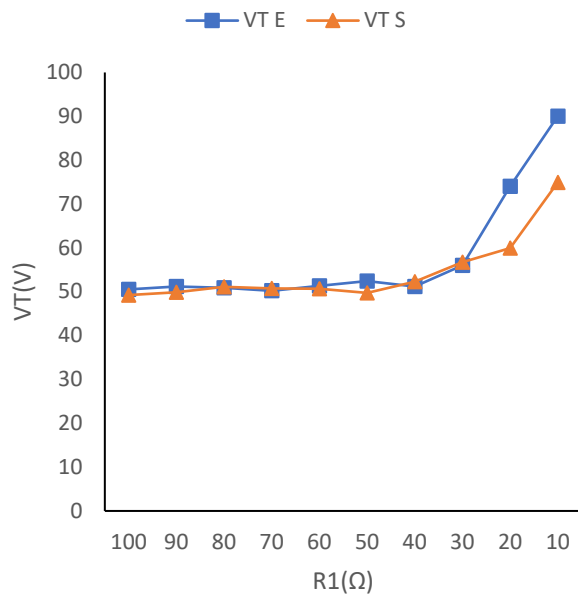


Fig. 5.7 Simulated vs experimental results of closed loop FOPID control for (a) V_T (b) V_{01} (c) V_T and (d) V_{01} with input voltage variations keeping V_{in2} as 12V and 24V respectively.

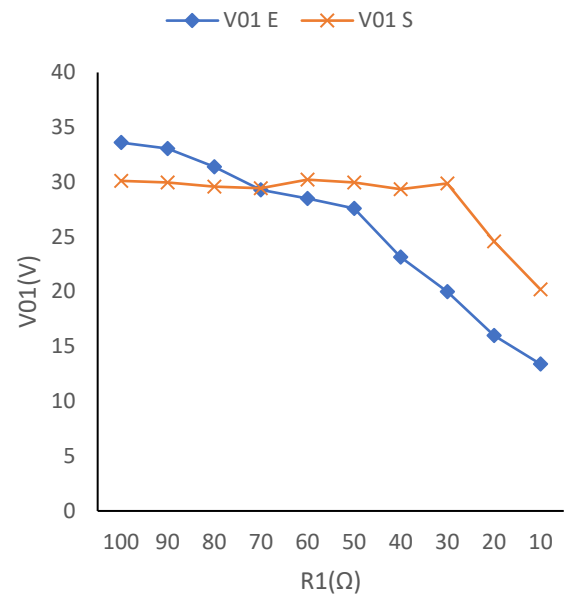
Fig. 5.7 shows output voltage variation as input voltage (V_{in1}) is varied. Fig. 5.7(a-b) shows output voltage variation for 12V battery as V_{in2} . In closed loop FOPID control, as the input voltage is increasing from 0 to 11V (keeping in mind the constraint $V_{in1} < V_{in2}$) output voltages tries to maintain the desired setpoint voltages. The desired V_T is 20V whereas desired V_{01} is 15V. V_T tries to maintain 20V at output as V_{in1} varies from 4V to 9V in simulation whereas V_{in1} varies from 5V to 10V during experimentation. V_{01} tries to maintain 15V as V_{in1} varies from 4V to 11V in simulation whereas V_{in1} varies from 3V to 11V during experimentation. Fig. 5.7(c-d) shows output voltage variation for 24V battery as V_{in2} . Using FOPID control, as the input voltage is increasing from 0 to 23V (keeping in mind the constraint $V_{in1} < V_{in2}$) output voltages tries to maintain the desired setpoint voltages. The desired V_T is 50V whereas desired V_{01} is 30V. V_T tries to maintain 50V at output as V_{in1} varies from 11V to 23V in simulation whereas V_{in1} varies from 14V to 21V during experimentation. V_{01} tries to maintain 30V as V_{in1} varies from 3V to 23V in simulation whereas V_{in1} varies from 7V to 21V during experimentation. The constraints of duty ratios make it hard to maintain desired setpoints during initial and final V_{in2} values. Internal resistance of each component also adds to slight variation in simulation and experimental data.

5.3.6 Performance of FOPID controller on Load Variations

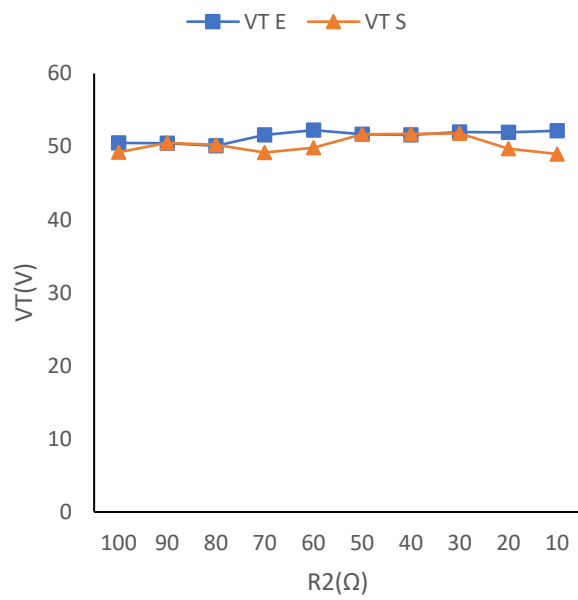
The performance of the non-isolated multi-input multi-output DC-DC boost converter with closed loop FOPID controller subjected to load variations is discussed in this section. Duty ratio of each switch is evaluated using the control algorithm programmed in the microcontroller. The load variations are performed in three parts. Firstly, load R_1 is varied and results are accumulated. Then load R_2 is varied and data is collected. Finally, both the loads R_1 and R_2 are varied simultaneously and proportionally. During the whole procedure of simulation and experimental data acquisition, the input voltages V_{in1} and V_{in2} are kept at 18V and 24V respectively. The loads R_1 and R_2 varies from 100 Ω to 10 Ω with an interval of 10 Ω each.



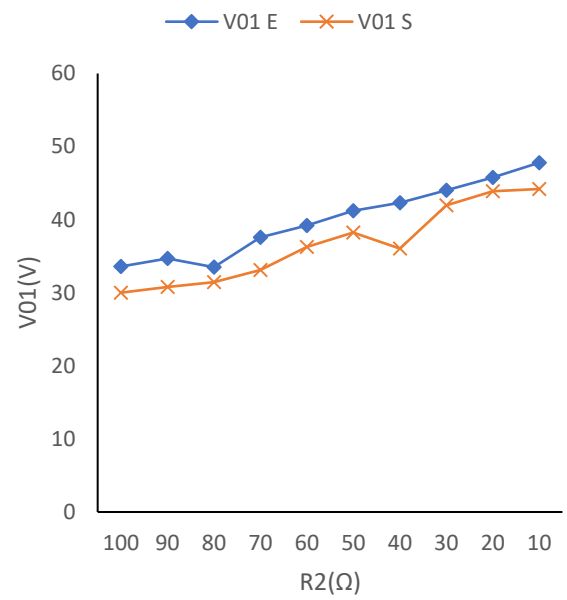
(a)



(b)



(c)



(d)

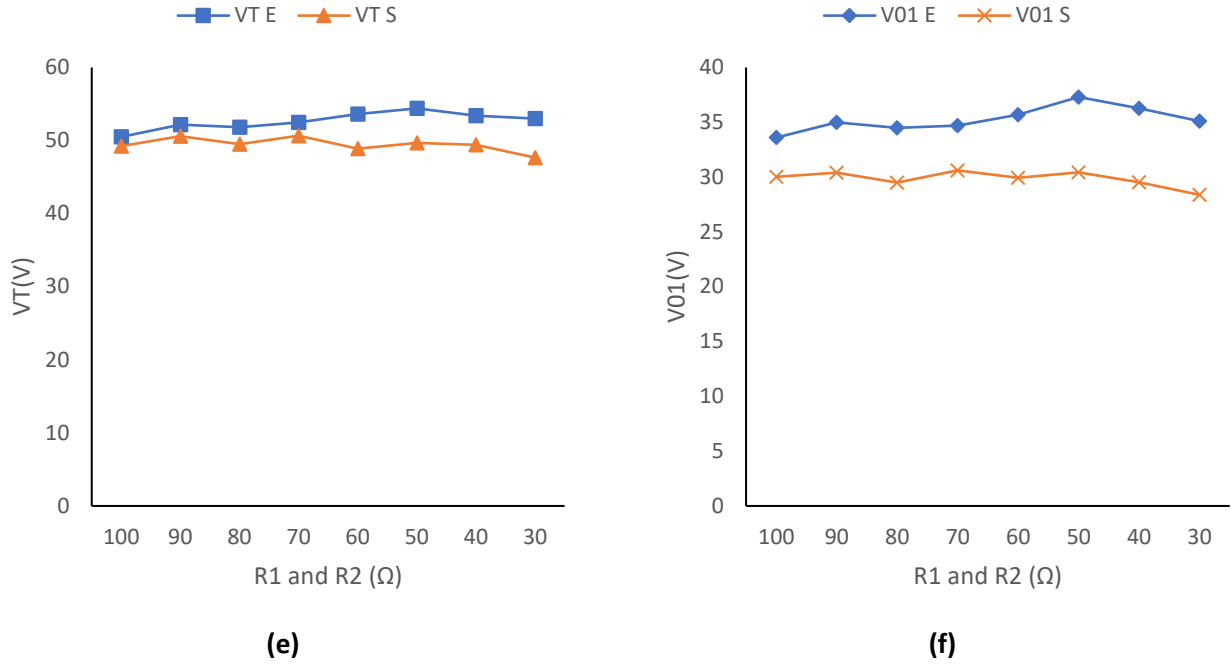


Fig. 5.8 Simulated vs experimental results of closed loop FOPID control for (a) V_T (b) V_{01} (c) V_T (d) V_{01} (e) V_T and (f) V_{01} with load resistance variations.

Fig. 5.8 shows output voltage variation as load resistance is varied. Fig. 5.8(a-b) shows output voltage variation with change in load resistance R_1 from 100Ω to 10Ω with an interval of 10Ω. In closed loop FOPID control, as R_1 value decreases, desired V_T and V_{01} i.e. 50V and 30V is maintained respectively. Desired V_T is maintained from 100Ω to 40 Ω during simulation whereas from 100Ω to 40Ω during experimentation. Desired V_{01} is maintained from 100Ω to 30Ω during simulation whereas from 100Ω to 50Ω during experimentation. Fig. 5.8(c-d) shows output voltage variation with change in load resistance R_2 from 100Ω to 10Ω with an interval of 10Ω. In closed loop FOPID control, as R_2 value decreases, desired V_T and V_{01} i.e. 50V and 30V is maintained respectively. Desired V_T is maintained from 100Ω to 10Ω during simulation whereas from 100Ω to 10Ω during experimentation. Desired V_{01} is maintained from 100Ω to 70Ω during simulation whereas from 100Ω to 80Ω during experimentation. Fig. 5.8(e-f) shows output voltage variation with change in load resistance R_1 and R_2 from 100Ω to 10Ω with an interval of 10Ω simultaneously and proportionally. In closed loop FOPID control, as R_1 and R_2 value decreases, desired V_T and V_{01} i.e. 50V and 30V is maintained respectively. Desired V_T is maintained from 100Ω to 30Ω during simulation whereas from 100Ω to 70Ω during experimentation. Desired V_{01} is maintained from 100Ω to 30Ω during simulation whereas from 100Ω to 30Ω during experimentation. The constraints of duty ratios and inductor saturation point make it hard to maintain desired setpoints during low load resistance values. Internal resistance of each component also adds to slight variation in simulation and experimental data.

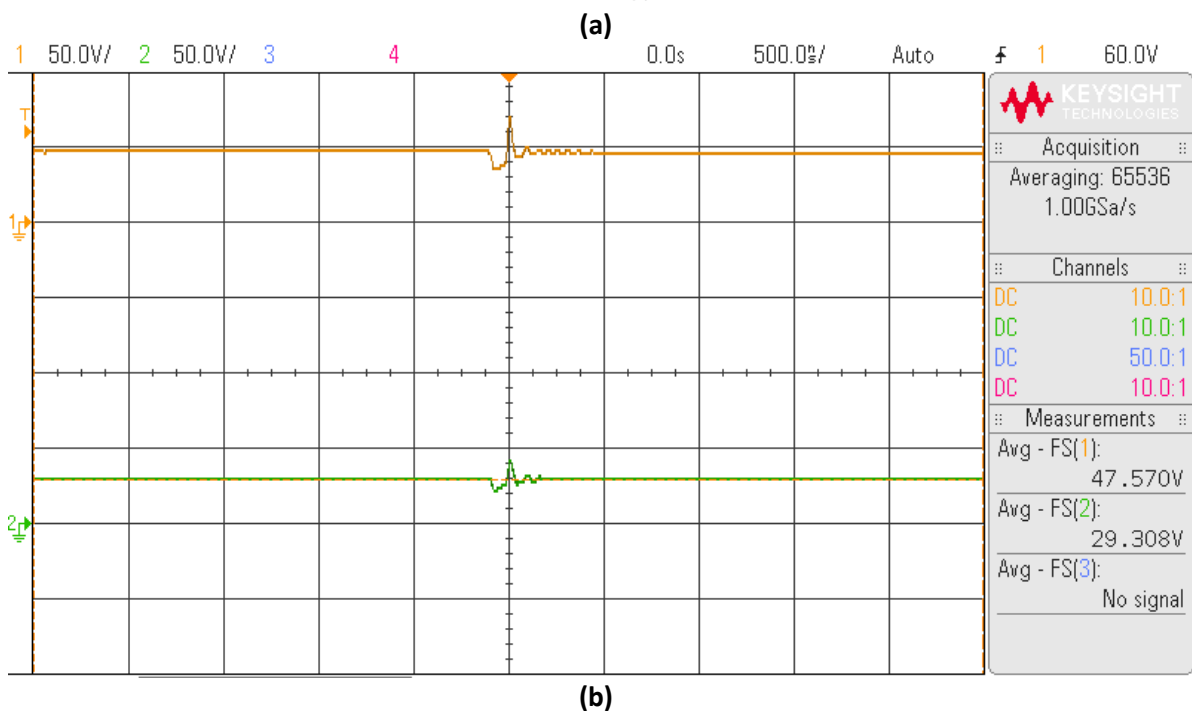
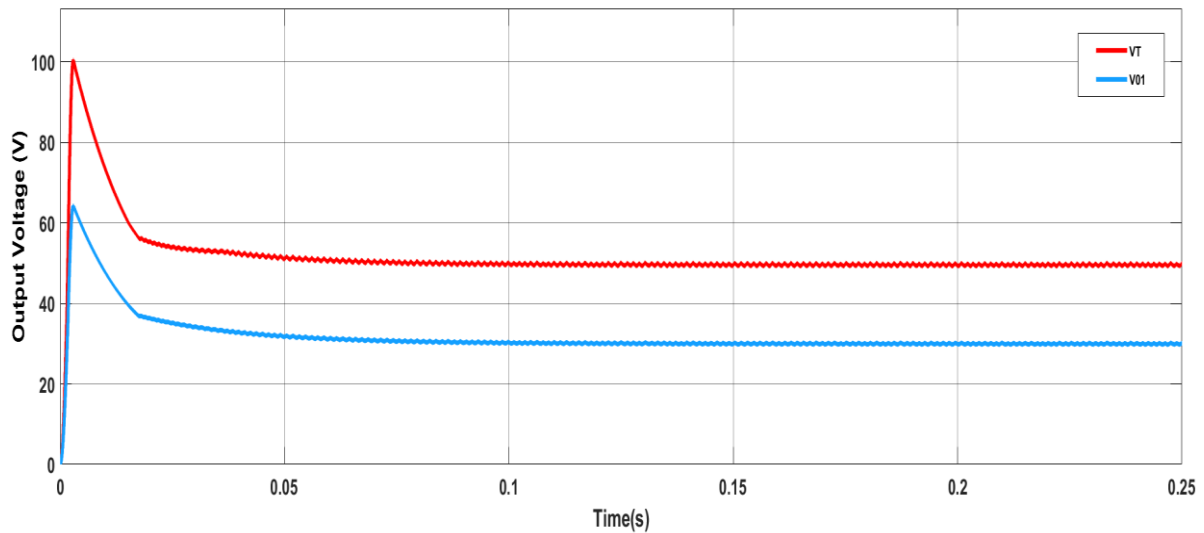


Fig. 5.8.1 Output Voltage (V_T & V_{01}) plot for (a) simulated and (b) experimental results.

Fig. 5.8.1 shows the output voltage waveforms obtained from simulation and experimental results. Fig. 5.8.1(a) shows output voltage waveforms obtained during simulation whereas Fig. 5.8.1(b) indicates output voltage waveform during experimental results obtained on DSO. These waveforms are obtained for FOPID control strategy implemented on the non-isolated multi-input multi-output DC-DC boost converter. The simulations voltages i.e. V_T and V_{01} settles at 50V and 30V respectively whereas it can be observed that experimental values show 47.57V and 29.308V respectively. The input voltages V_{in1} and V_{in2} were taken as 18V and 24V respectively and load resistance as 100 Ω each.

5.3.7 Performance of ANN controller on Input Variations

The performance of the non-isolated multi-input multi-output DC-DC boost converter with closed loop ANN controller subjected to input variations is discussed in this section. Duty ratio of each switch is evaluated using the control algorithm programmed in the microcontroller. Input voltage V_{in1} is varied keeping V_{in2} as 12V and 24V respectively. Load R_1 and R_2 are kept at 100Ω each.

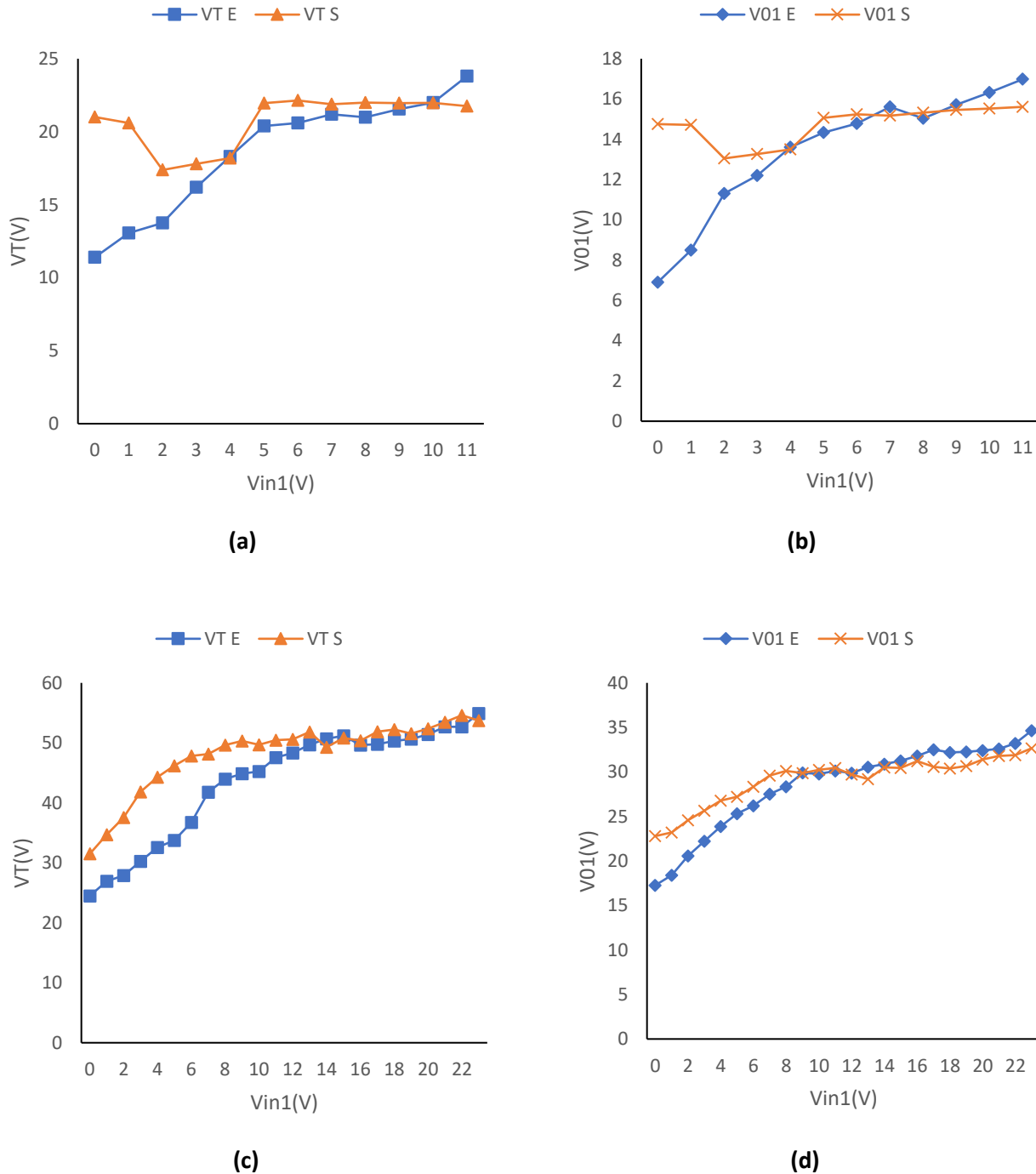
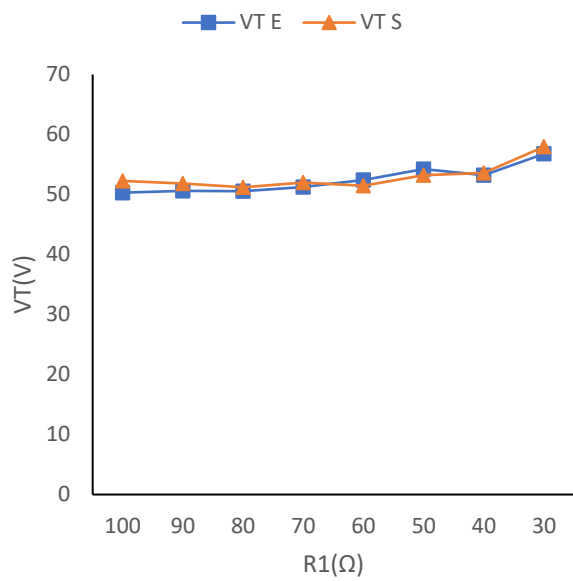


Fig. 5.9 Simulated vs experimental results of closed loop ANN control for (a) V_T (b) V_{01} (c) V_T and (d) V_{01} with input voltage variations.

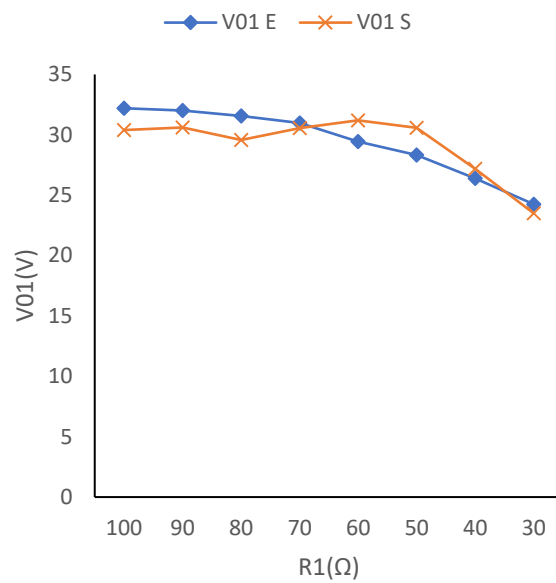
Fig. 5.9 shows output voltage variation as input voltage (V_{in1}) is varied. Fig. 5.9(a-b) shows output voltage variation for 12V battery as V_{in2} . In closed loop ANN control, as the input voltage is increasing from 0 to 11V (keeping in mind the constraint $V_{in1} < V_{in2}$) output voltages tries to maintain the desired setpoint voltages. The desired V_T is 20V whereas desired V_{01} is 15V. V_T tries to maintain 20V at output as V_{in1} varies from 0V to 11V in simulation whereas V_{in1} varies from 4V to 11V during experimentation. V_{01} tries to maintain 15V as V_{in1} varies from 0V to 11V in simulation whereas V_{in1} varies from 5V to 11V during experimentation. Fig. 5.9(c-d) shows output voltage variation for 24V battery as V_{in2} . Using ANN control, as the input voltage is increasing from 0 to 23V (keeping in mind the constraint $V_{in1} < V_{in2}$) output voltages tries to maintain the desired setpoint voltages. The desired V_T is 50V whereas desired V_{01} is 30V. V_T tries to maintain 50V at output as V_{in1} varies from 6V to 20V in simulation whereas V_{in1} varies from 12V to 22V during experimentation. V_{01} tries to maintain 30V as V_{in1} varies from 6V to 23V in simulation whereas V_{in1} varies from 8V to 21V during experimentation. The constraints of duty ratios make it hard to maintain desired setpoints during initial and final V_{in2} values. Internal resistance of each component also adds to slight variation in simulation and experimental data.

5.3.8 Performance of ANN controller on Load Variations

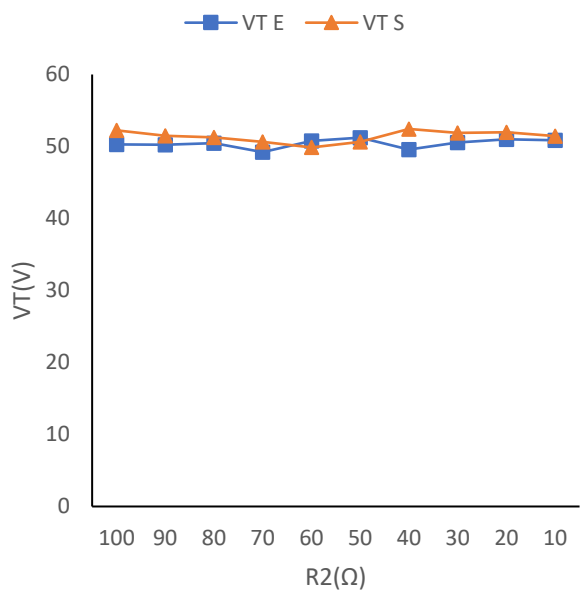
The performance of the non-isolated multi-input multi-output DC-DC boost converter with closed loop ANN controller subjected to load variations is discussed in this section. Duty ratio of each switch is evaluated using the control algorithm programmed in the microcontroller. The load variations are performed in three parts. Firstly, load R_1 is varied and results are accumulated. Then load R_2 is varied and data is collected. Finally, both the loads R_1 and R_2 are varied simultaneously and proportionally. During the whole procedure of simulation and experimental data acquisition, the input voltages V_{in1} and V_{in2} are kept at 18V and 24V respectively. The loads R_1 and R_2 varies from 100 Ω to 10 Ω with an interval of 10 Ω each.



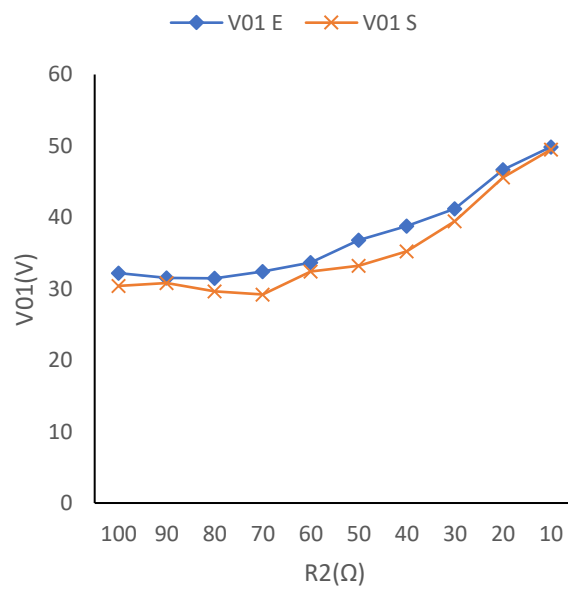
(a)



(b)



(c)



(d)

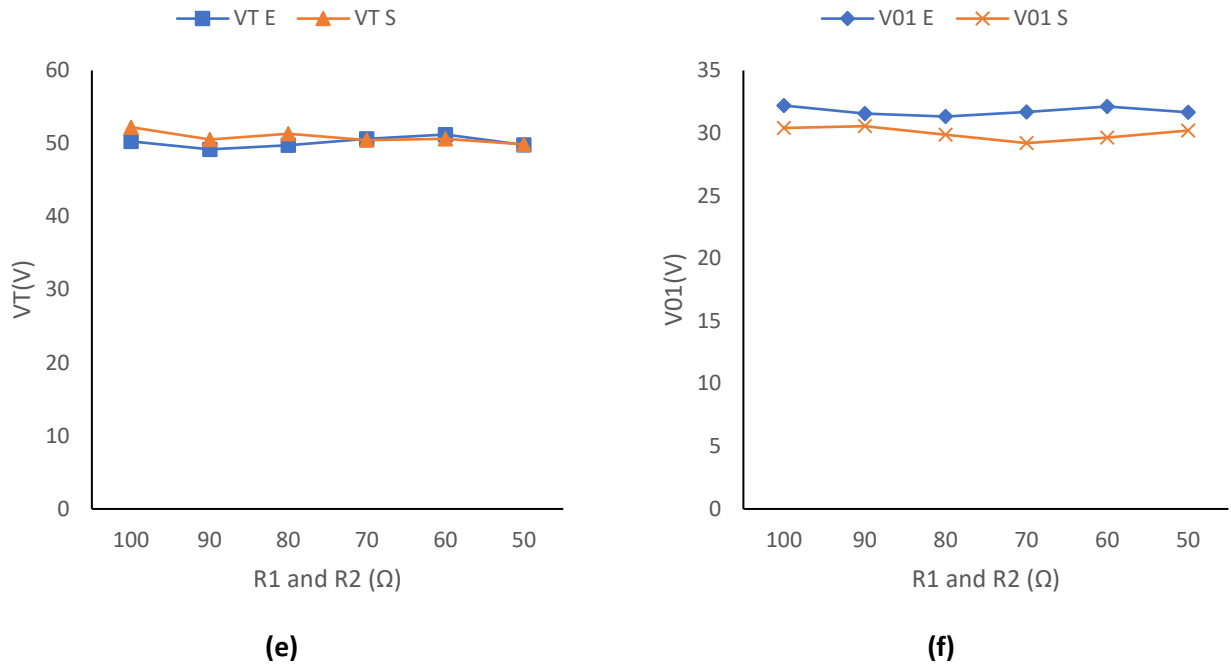


Fig. 5.10 Simulated vs experimental results of closed loop ANN control for (a) V_T (b) V_{O1} (c) V_T (d) V_{O1} (e) V_T and (f) V_{O1} with input voltage variations keeping V_{in2} as 12V and 24V respectively.

Fig. 5.10 shows output voltage variation as load resistance is varied. Fig. 5.10(a-b) shows output voltage variation with change in load resistance R_1 from 100Ω to 10Ω with an interval of 10Ω. In closed loop ANN control, as R_1 value decreases, desired V_T and V_{O1} i.e. 50V and 30V is maintained respectively. Desired V_T is maintained from 100Ω to 40Ω during simulation whereas from 100Ω to 40Ω during experimentation. Desired V_{O1} is maintained from 100Ω to 50Ω during simulation whereas from 100Ω to 50Ω during experimentation. Fig. 5.10(c-d) shows output voltage variation with change in load resistance R_2 from 100Ω to 10Ω with an interval of 10Ω. In closed loop ANN control, as R_2 value decreases, desired V_T and V_{O1} i.e. 50V and 30V is maintained respectively. Desired V_T is maintained from 100Ω to 10Ω during simulation whereas from 100Ω to 10Ω during experimentation. Desired V_{O1} is maintained from 100Ω to 60Ω during simulation whereas from 100Ω to 70Ω during experimentation. Fig. 5.10(e-f) shows output voltage variation with change in load resistance R_1 and R_2 from 100Ω to 10Ω with an interval of 10Ω simultaneously and proportionally. In closed loop ANN control, as R_1 and R_2 value decreases, desired V_T and V_{O1} i.e. 50V and 30V is maintained respectively. Desired V_T is maintained from 100Ω to 50Ω during simulation whereas from 100Ω to 50Ω during experimentation. Desired V_{O1} is maintained from 100Ω to 50Ω during simulation whereas from 100Ω to 50Ω during experimentation. The constraints of duty ratios and inductor saturation point make it hard to maintain desired setpoints during low load resistance values. Internal resistance of each component also adds to slight variation in simulation and experimental data.

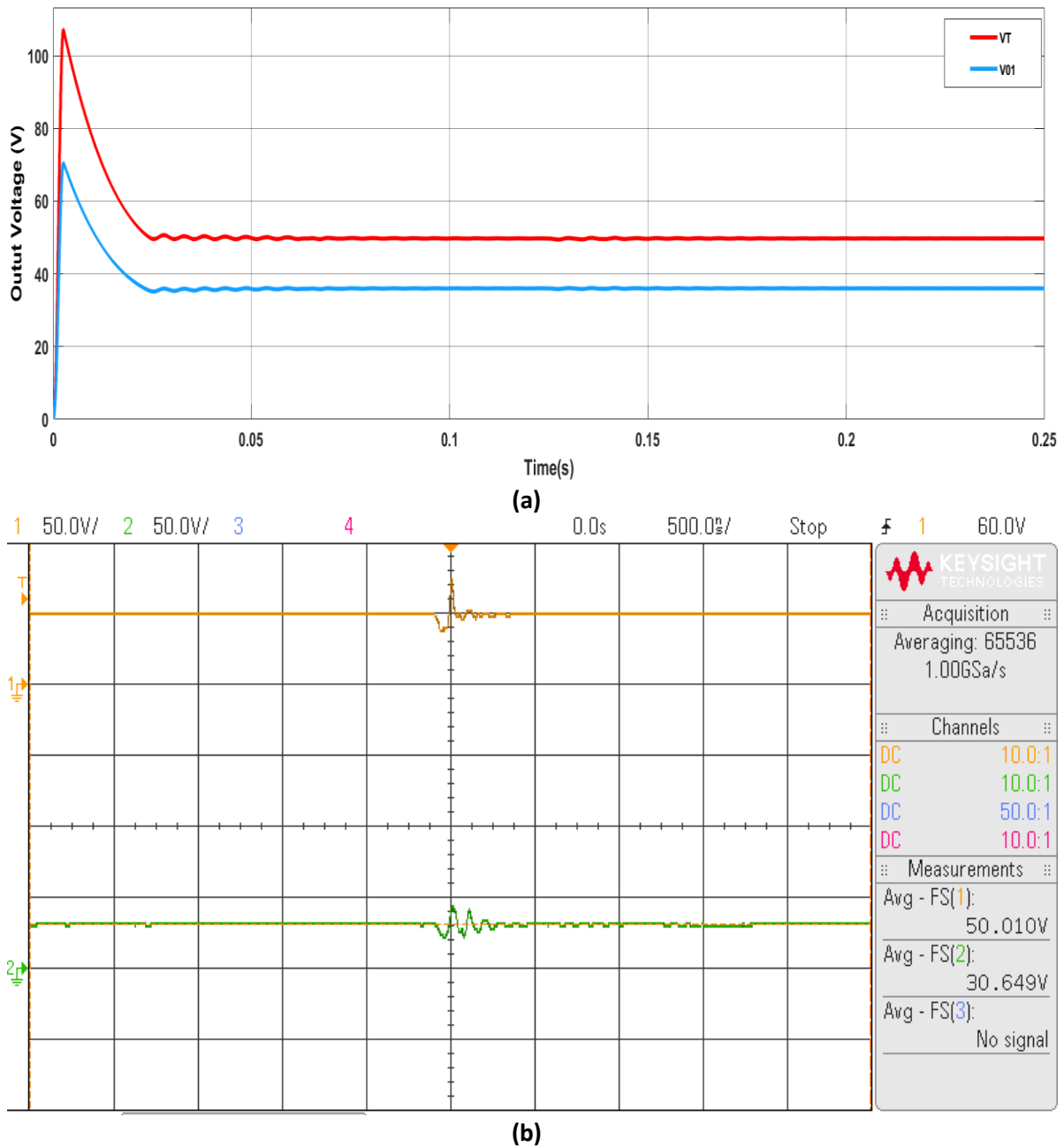


Fig. 5.10.1 Output Voltage (V_T & V_{O1}) plot for (a) simulated and (b) experimental results.

Fig. 5.10.1 shows the output voltage waveforms obtained from simulation and experimental results. Fig. 5.10.1(a) shows output voltage waveforms obtained during simulation whereas Fig. 5.10.1(b) indicates output voltage waveform during experimental results obtained on DSO. These waveforms are obtained for ANN control strategy implemented on the non-isolated multi-input multi-output DC-DC boost converter. The simulations voltages i.e. V_T and V_{O1} settles at 50V and 30V respectively whereas it can be observed that experimental values show 50.01V and 30.649V respectively. The input voltages V_{in1} and V_{in2} were taken as 18V and 24V respectively and load resistance as 100 Ω each.

5.4 Comparative Analysis

The graphical investigation of the non-isolated multi-input multi-output DC-DC boost converter has been done in this section by comparing various simulated and experimentally implemented control algorithms. It is the duty of switch S_1 to maintain V_T , switch S_3 to maintain I_B and switch S_4 to maintain V_{01} which has been discussed in the previous chapters. Simulation and experimental results are compared graphically subjected to input voltage variations as well as load variations.

5.4.1 Performance of various control algorithms subjected to input variations

The simulated and experimental output voltage (V_T) variation with input voltage (V_{in2} as 12V) has been shown in Fig. 5.11 and Fig. 5.12 respectively. The trend shown in Fig. 5.11 is that ANN controller has the best performance as it almost keeps 20V at output whereas in Fig. 5.12 ANN and PI controller performs better than other controllers. It can be observed from the figure that open loop voltage keeps on increasing whereas other control strategies increases till the setpoint is achieved and then follows the setpoint pattern. However, due to duty constraints setpoint voltage is not followed during initial and final values of input voltages. So, the voltage at initial and final points will be less and more than the setpoint value respectively.

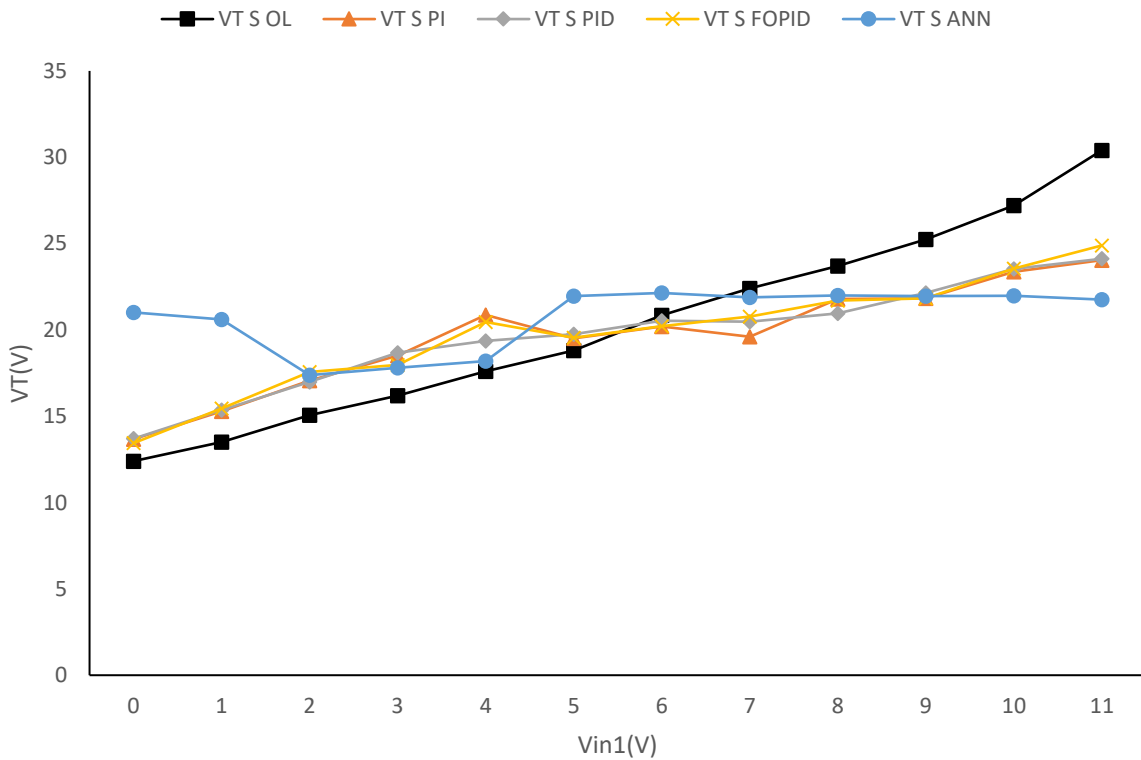


Fig. 5.11 Simulated output voltage vs input voltage (V_{in1}) variations keeping 12V as V_{in2}

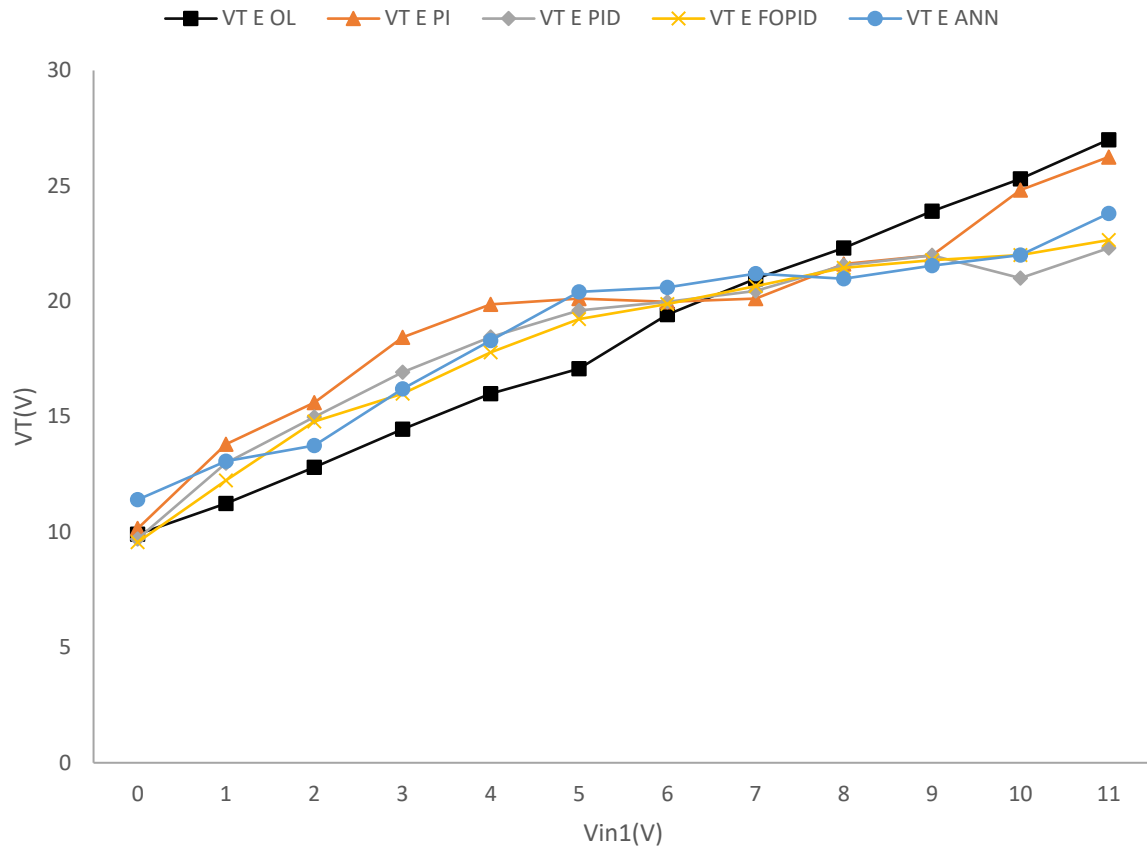


Fig. 5.12 Experimental output voltage vs input voltage (V_{in1}) variations keeping 12V as V_{in2}

The simulated and experimental output voltage (V_T) variation with input voltage (V_{in2} as 24V) has been shown in Fig. 5.13 and Fig. 5.14 respectively. The trend shown in Fig. 5.13 is that ANN controller has the best performance as it almost keeps 50V at output whereas in Fig. 5.14 PID and PI controller performs better than other controllers and they almost overlaps each other. It can also be observed from the figure that open loop voltage keeps on increasing whereas other control strategies increases till the setpoint is achieved and then follows the setpoint pattern. However, due to duty constraints setpoint voltage is not followed during initial and final values of input voltages. So, the voltage at initial and final points will be less and more than the setpoint value respectively.

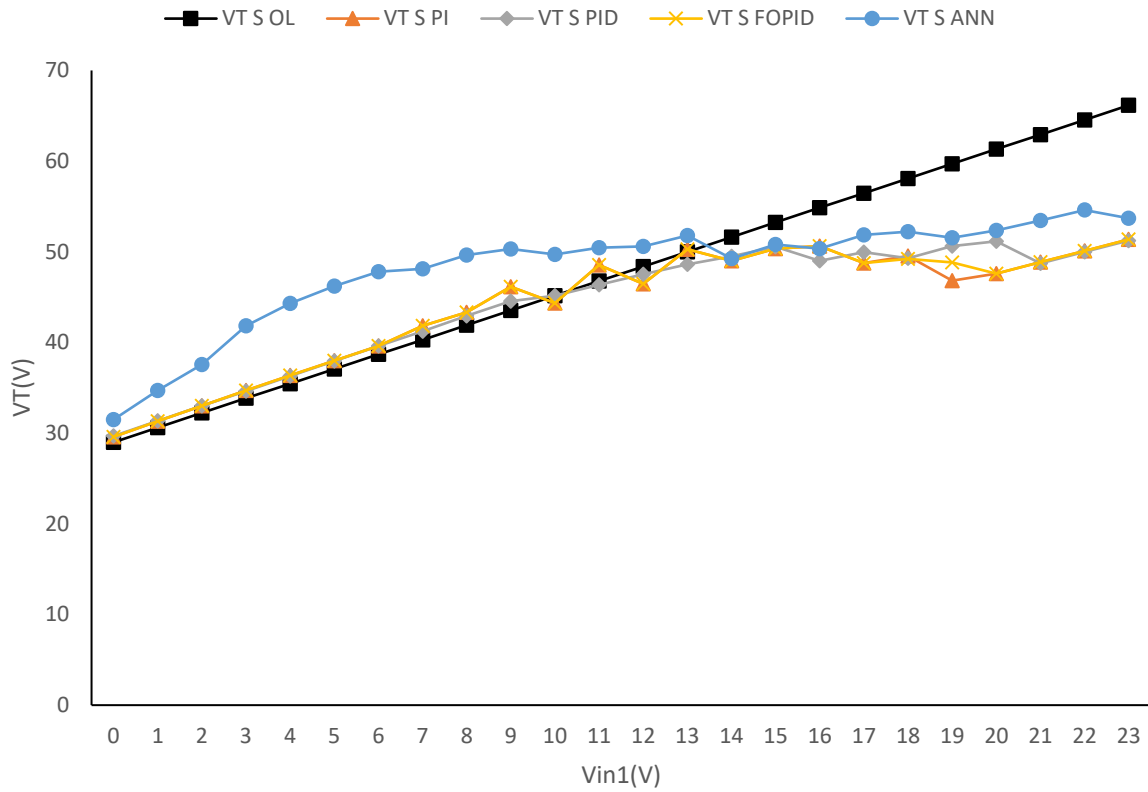


Fig. 5.13 Simulated output voltage vs input voltage (V_{in1}) variations keeping 24V as V_{in2}

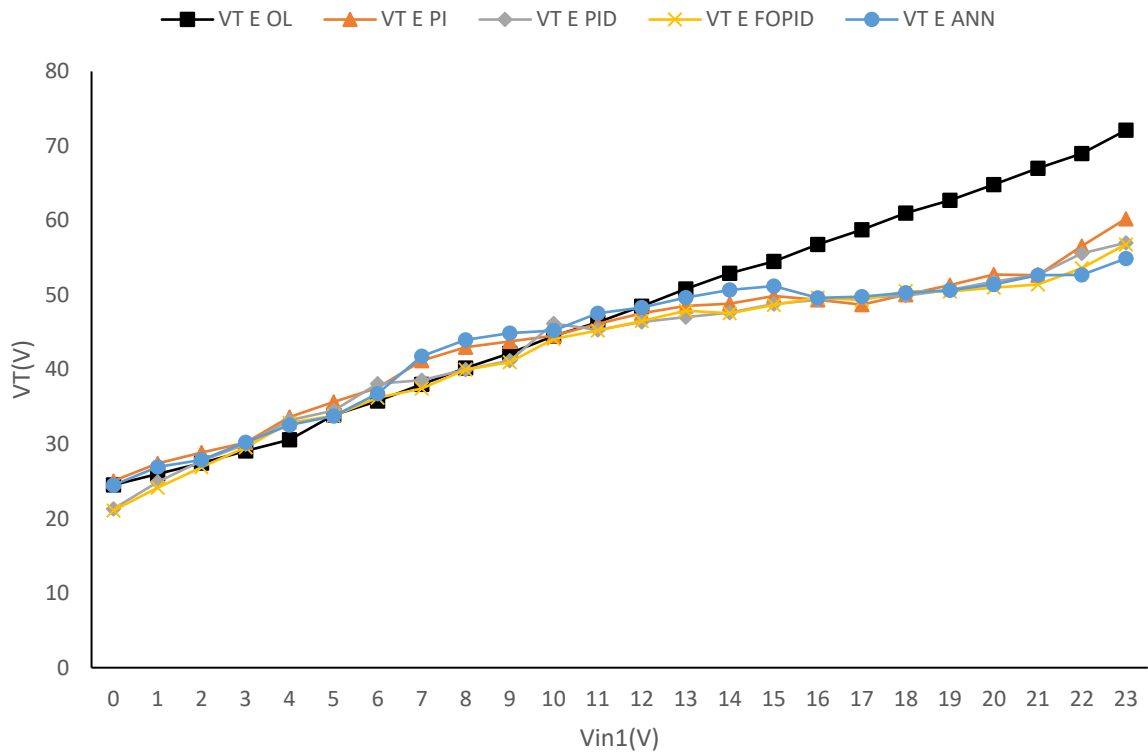


Fig. 5.14 Experimental output voltage vs input voltage (V_{in1}) variations keeping 24V as V_{in2}

The simulated and experimental output voltage (V_{01}) variation with input voltage (V_{in2} as 12V) has been shown in Fig. 5.15 and Fig. 5.16 respectively. The trend shown in Fig. 5.15 is that ANN controller has the best performance as it almost keeps 15V at output followed by FOPID controller whereas in Fig. 5.16 FOPID and PI controller gives better performance than other controllers. In Fig. 5.16, initially PID gives worst results but finally it follows ANN controller. It can be observed from the figure that open loop voltage keeps on increasing whereas other control strategies increases till the setpoint is achieved and then follows the setpoint pattern. However, due to duty constraints setpoint voltage is not followed during initial and final values of input voltages. So, the voltage at initial and final points will be less and more than the setpoint value respectively.

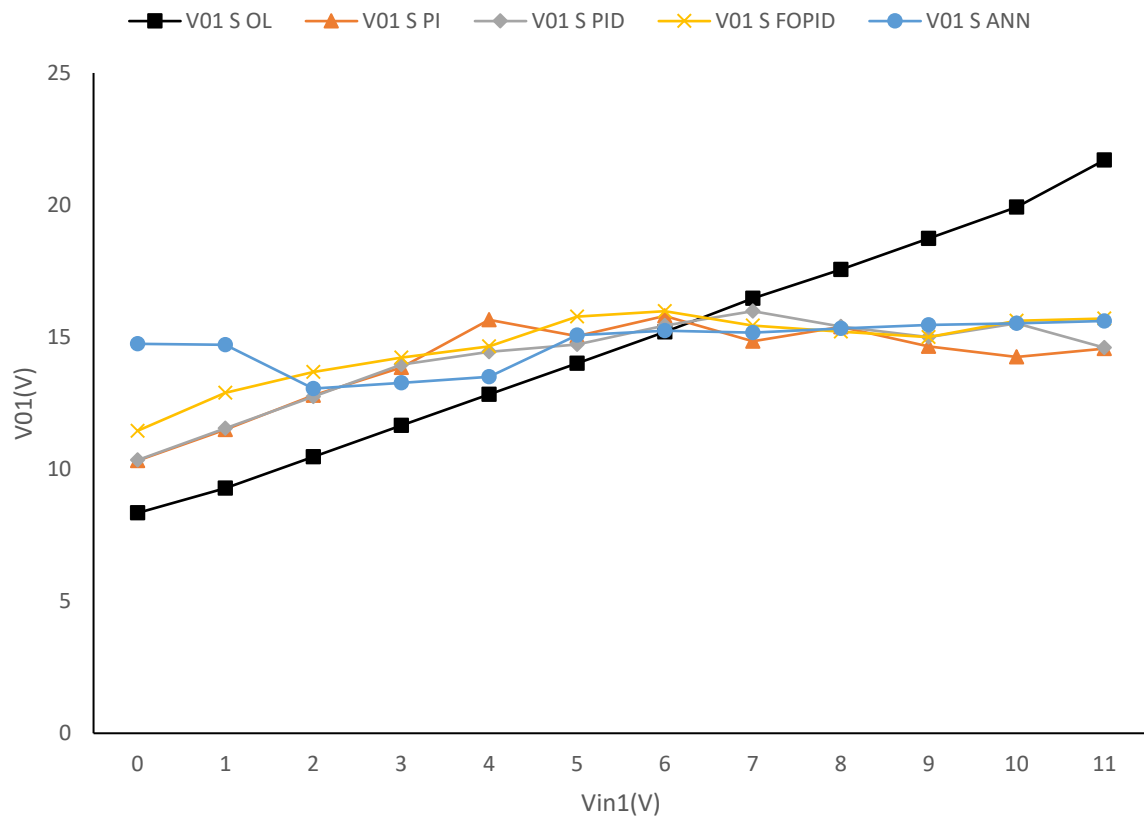


Fig. 5.15 Simulated output voltage (V_{01}) vs input voltage (V_{in1}) variations keeping 12V as V_{in2}

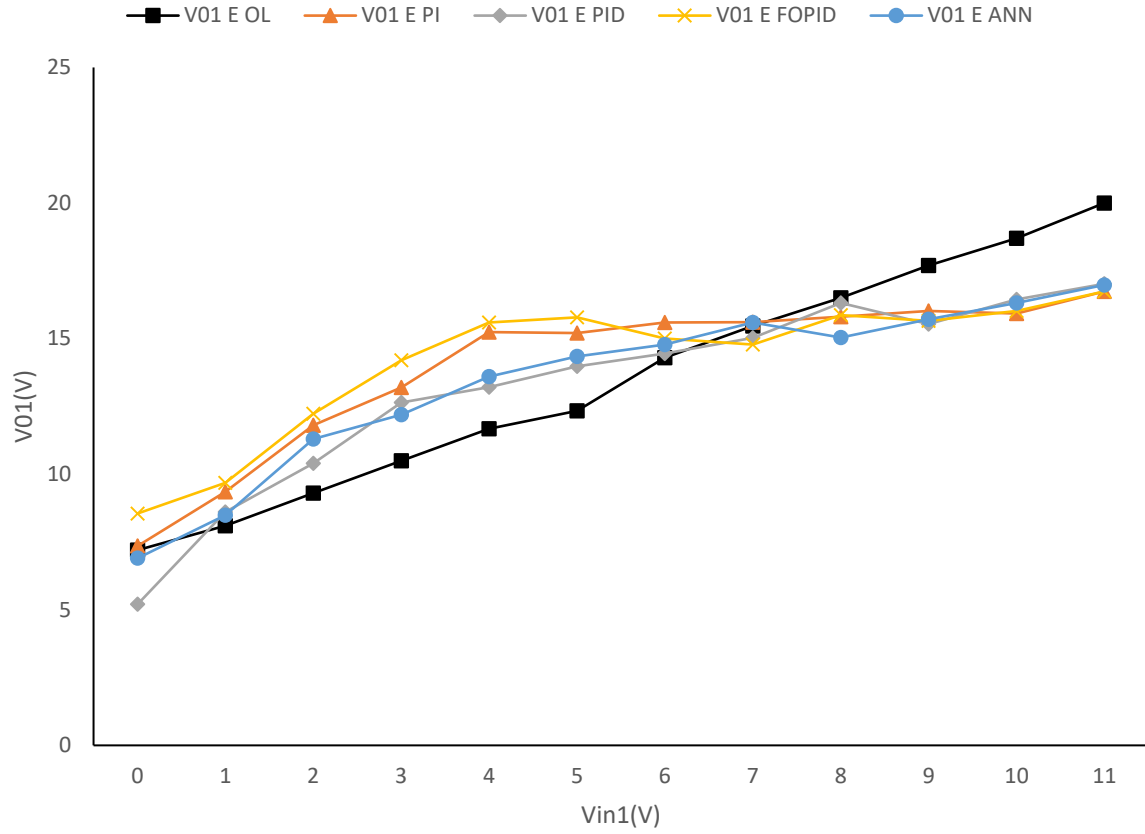


Fig. 5.16 Experimental output voltage (V_{01}) vs input voltage (V_{in1}) variations keeping 12V as V_{in2}

The simulated and experimental output voltage (V_{01}) variation with input voltage (V_{in2} as 24V) has been shown in Fig. 5.17 and Fig. 5.18 respectively. The trend shown in Fig. 5.17 is that FOPID controller has the best performance as it almost keeps 30V at output whereas in Fig. 5.18 ANN and FOPID controller performs better than other controllers. It can be observed from the figure that open loop voltage keeps on increasing whereas other control strategies increases till the setpoint is achieved and then follows the setpoint pattern. Here also in Fig. 5.18 PID gives worst results during initial input voltage values but finally follows the setpoint. However, due to duty constraints setpoint voltage is not followed during initial and final values of input voltages. So, the voltage at initial and final points will be less and more than the setpoint value respectively.

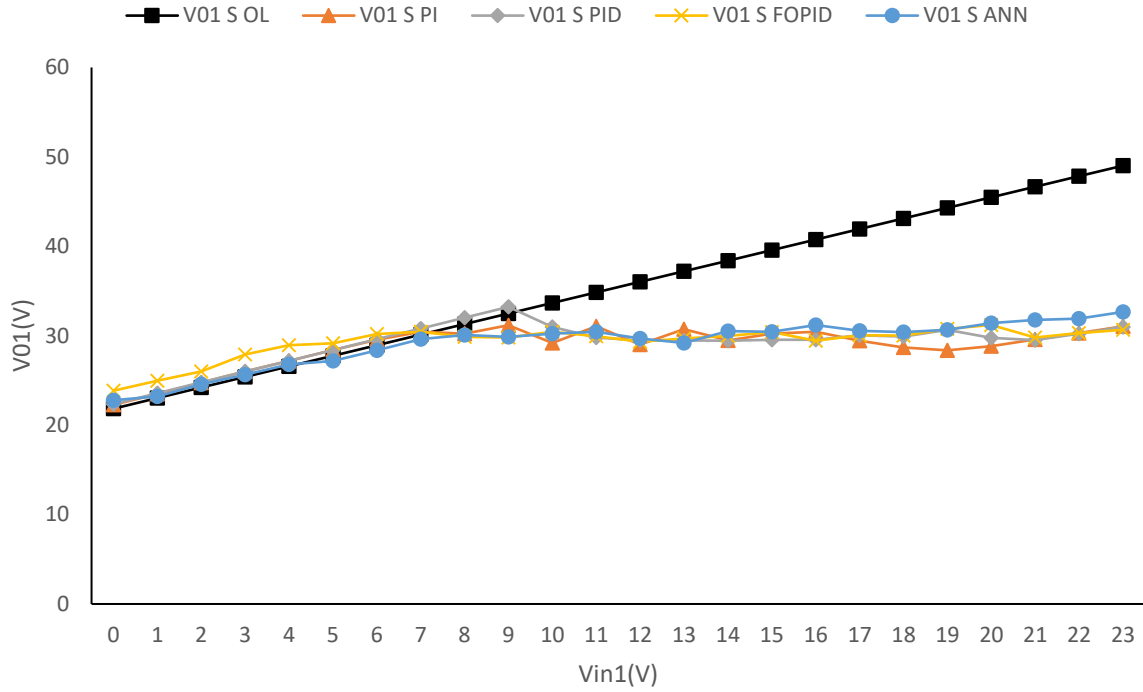


Fig. 5.17 Simulated output voltage (V_{01}) vs input voltage (V_{in1}) variations keeping 24V as V_{in2}

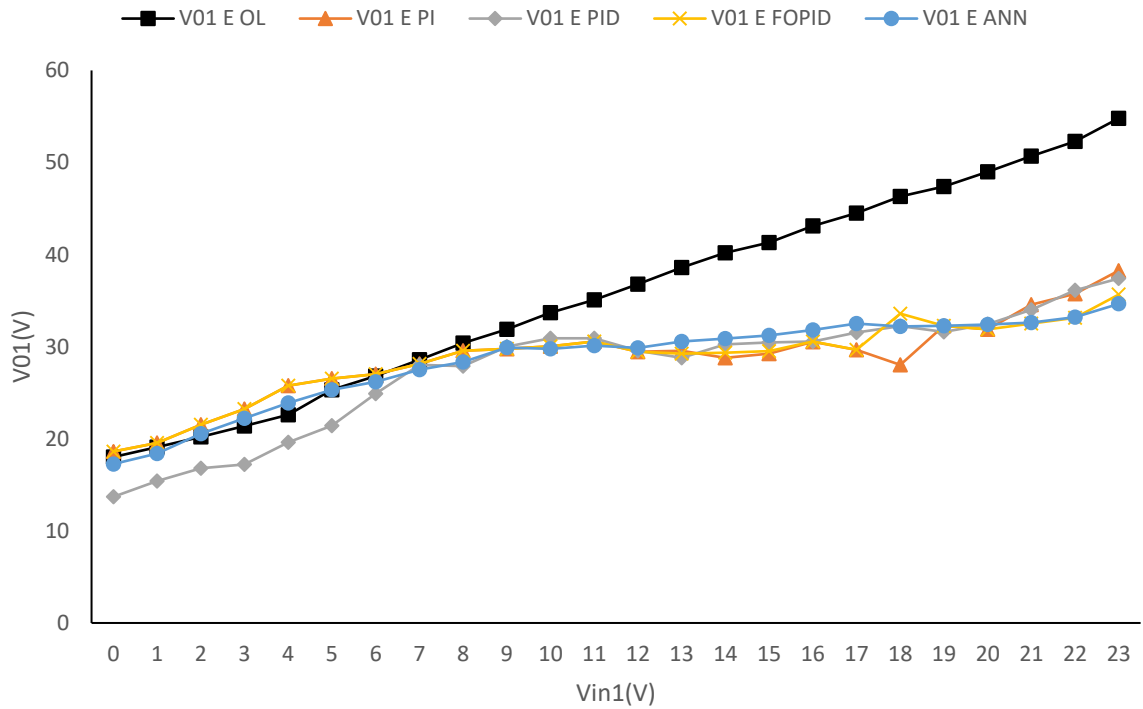


Fig. 5.18 Experimental output voltage (V_{01}) vs input voltage (V_{in1}) variations keeping 24V as V_{in2}

5.4.2 Performance of various control algorithms subjected to load variations

The variation of output voltage (V_T) with load resistance (R_1) has been shown in Fig. 5.19 and Fig. 5.20 for simulation and experimental data respectively. It can be observed in Fig. 5.19 that

ANN controller has the best performance as it almost keeps 50V at output whereas in Fig. 5.20 all controller almost follows same pattern diminishing the open loop voltage from 60V to 50V. It can be observed from the figure that open loop voltage is more whereas other control strategies follows the setpoint pattern. However, due to duty constraints and inductor saturation point voltage values are not evaluated experimentally below some resistance values.

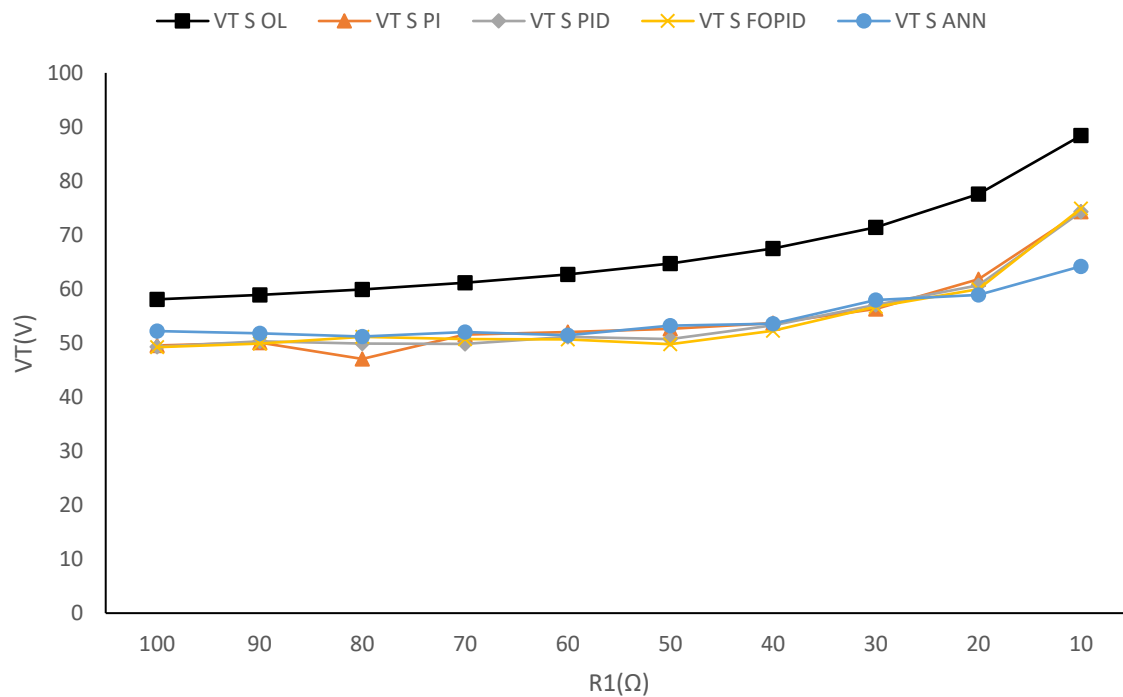


Fig. 5.19 Simulated output voltage vs load (R_1) variations

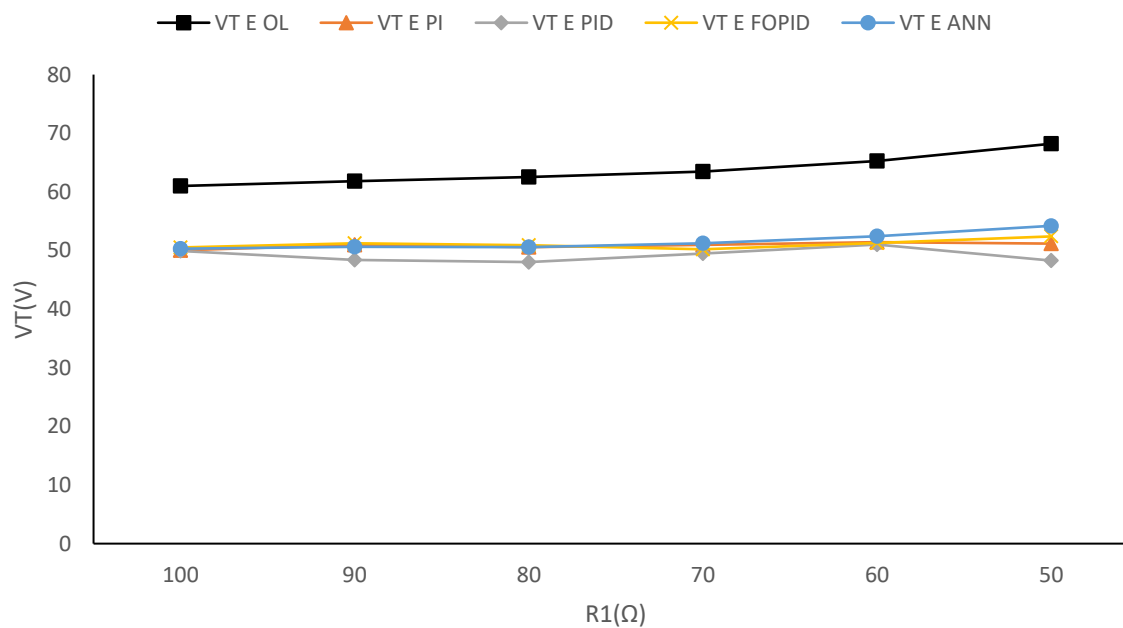


Fig. 5.20 Experimental output voltage vs load (R_1) variations

The variation of output voltage (V_T) with load resistance (R_2) has been shown in Fig. 5.21 and Fig. 5.22 for simulation and experimental data respectively. It can be observed in Fig. 5.21 that PID and FOPID controller have the best performance as it almost keeps 50V at output whereas in Fig. 5.22 ANN controller gives best possible results followed by other controllers.

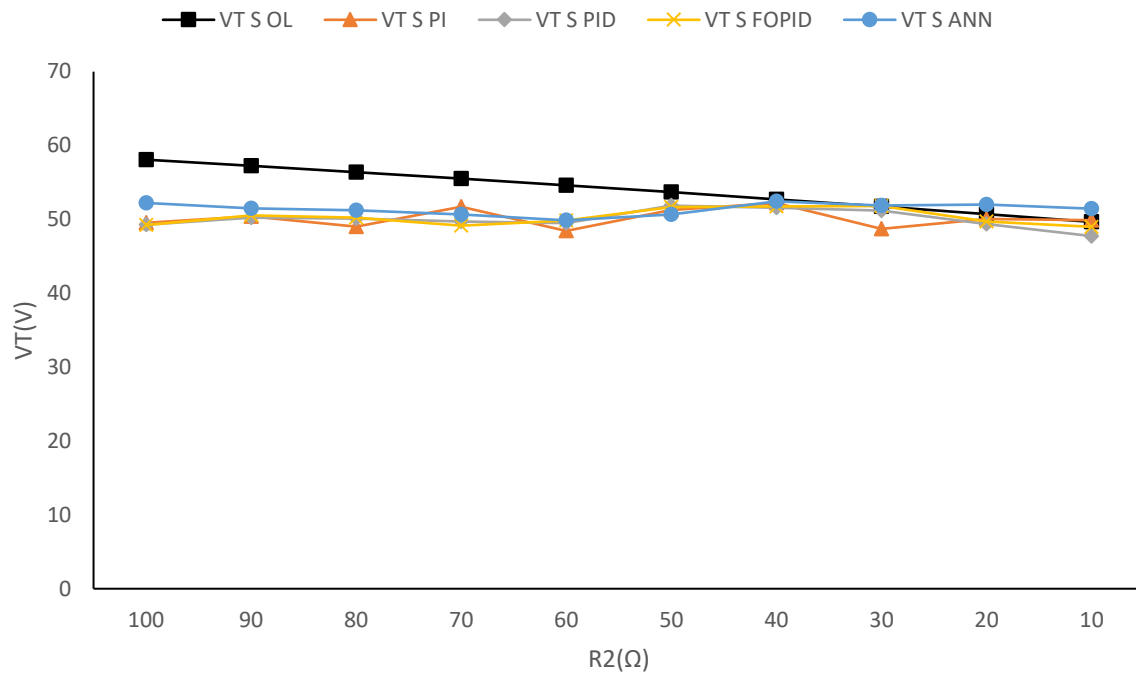


Fig. 5.21 Simulated output voltage vs load (R_2) variations

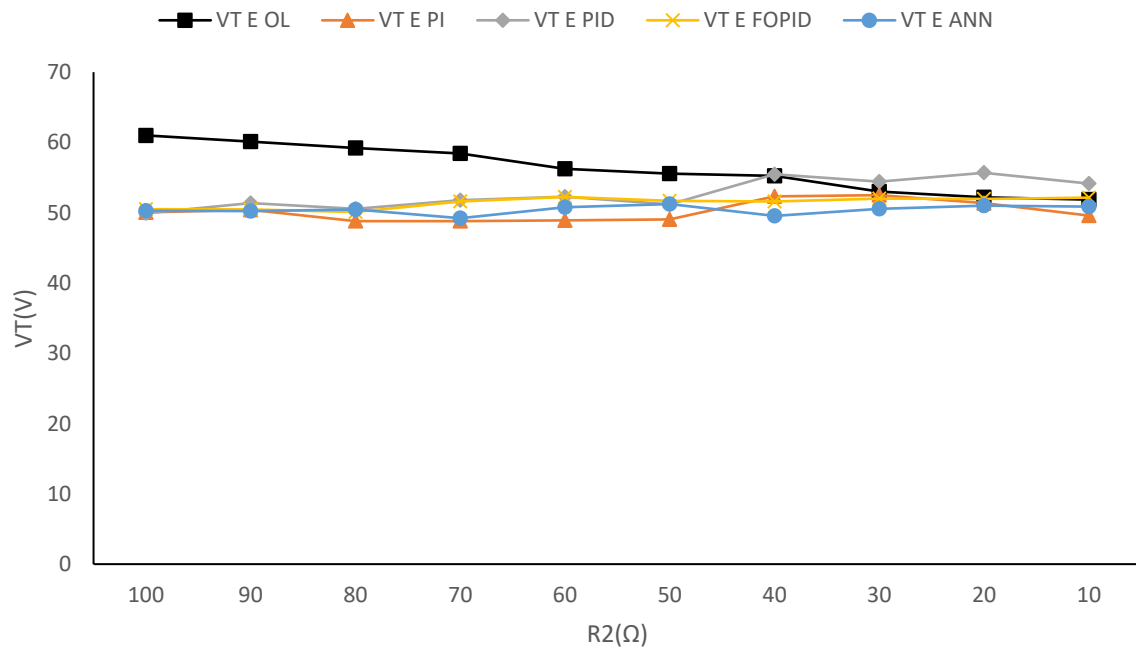


Fig. 5.22 Experimental output voltage vs load (R_2) variations

The variation of output voltage (V_T) with load resistance (R_1 & R_2) has been shown in Fig. 5.23 and Fig. 5.24 for simulation and experimental data respectively. It can be observed in Fig. 5.23 that FOPID and ANN controller has the best performance as it almost keeps 50V at output whereas in Fig. 5.24 ANN controller gives better results. However, due to duty constraints and inductor saturation point voltage values are not evaluated experimentally below some resistance values.

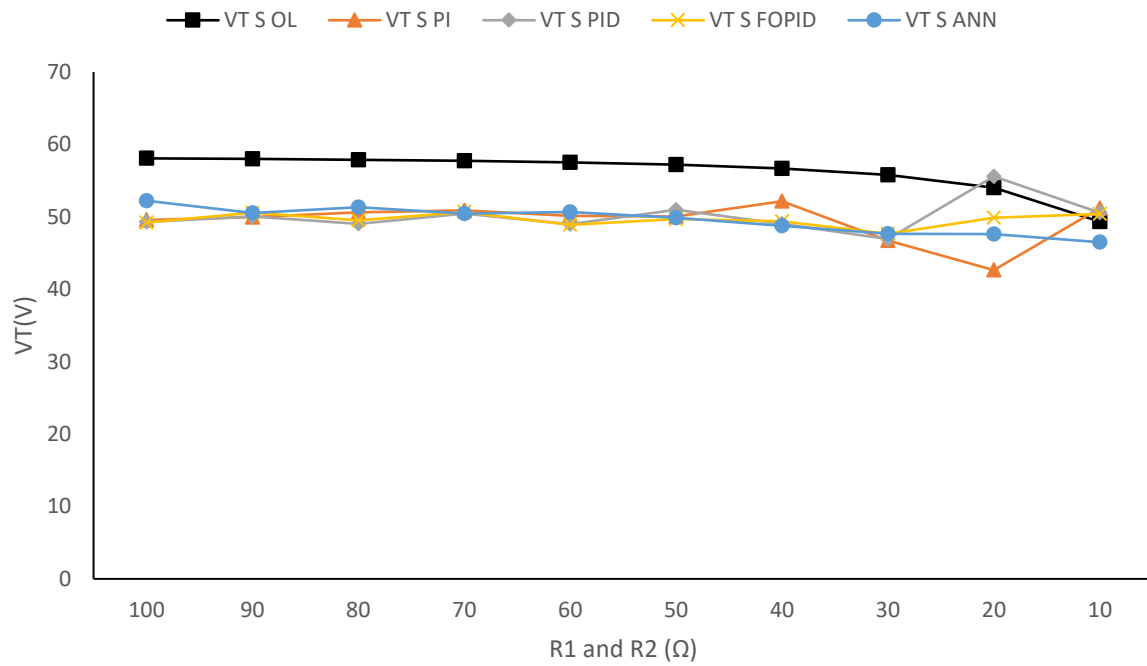


Fig. 5.23 Simulated output voltage vs load (R_1 and R_2) variations

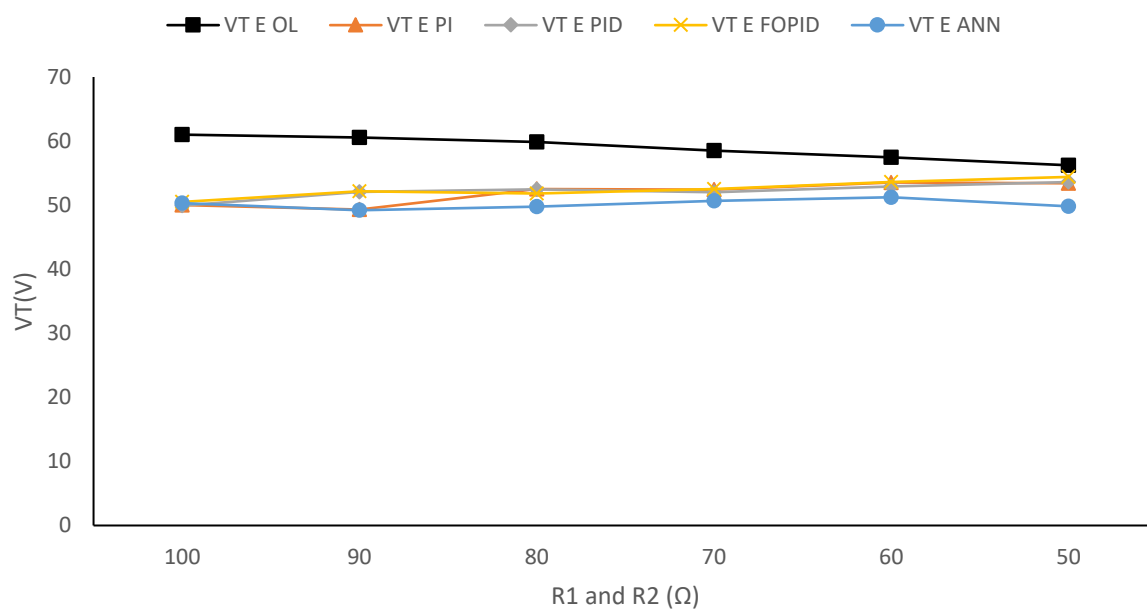


Fig. 5.24 Experimental output voltage vs load (R_1 and R_2) variations

The variation of output voltage (V_{01}) with load resistance (R_1) has been shown in Fig. 5.25 and Fig. 5.26 for simulation and experimental data respectively. It can be observed in Fig. 5.25 that PID controller has the best performance as it almost keeps 30V at output whereas in Fig. 5.26 ANN and FOPID controller gives better results. However, due to duty constraints and inductor saturation point voltage values are not evaluated experimentally below some resistance values.

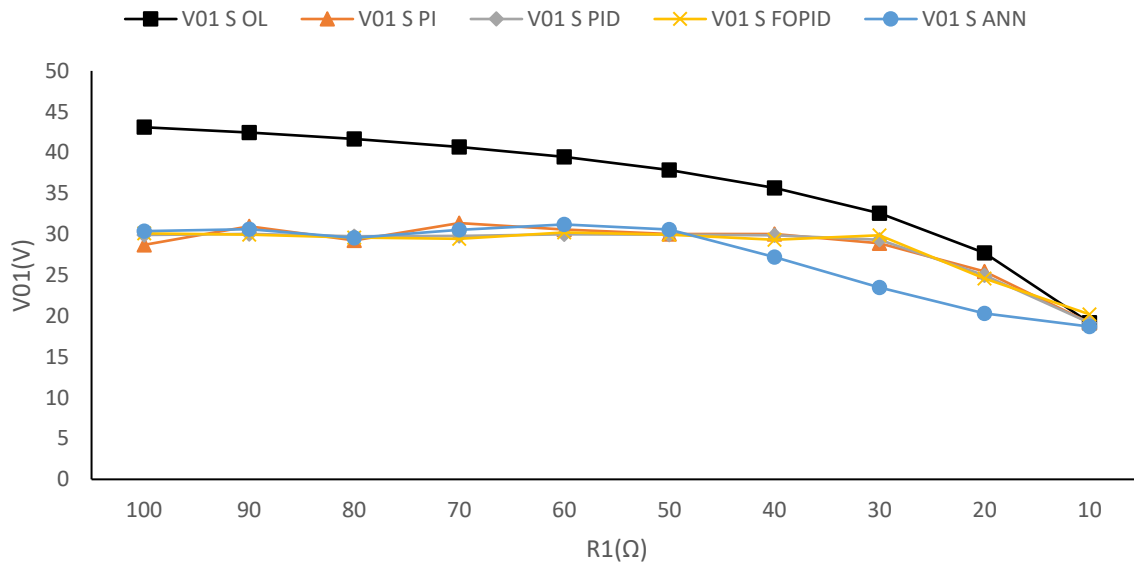


Fig. 5.25 Simulated output voltage (V_{01}) vs load (R_1) variations

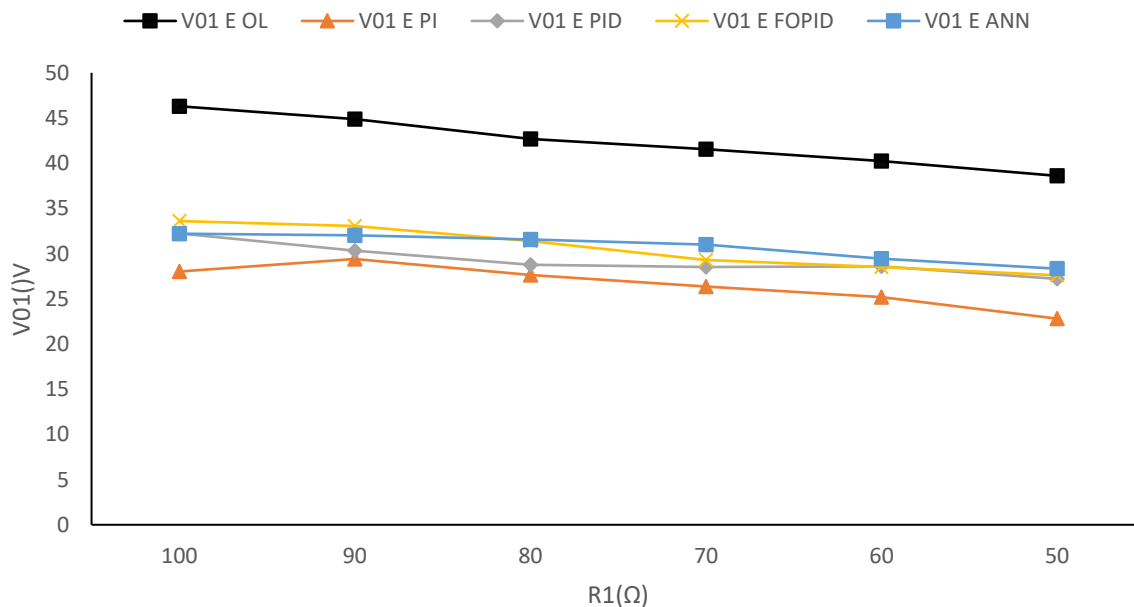


Fig. 5.26 Experimental output voltage (V_{01}) vs load (R_1) variations

The variation of output voltage (V_{01}) with load resistance (R_2) has been shown in Fig. 5.27 and Fig. 5.28 for simulation and experimental data respectively. It can be observed in Fig. 5.27 that

PID controller has the best performance as it almost keeps 30V at output whereas in Fig. 5.28 PI controller gives better results with respect to other control strategies.

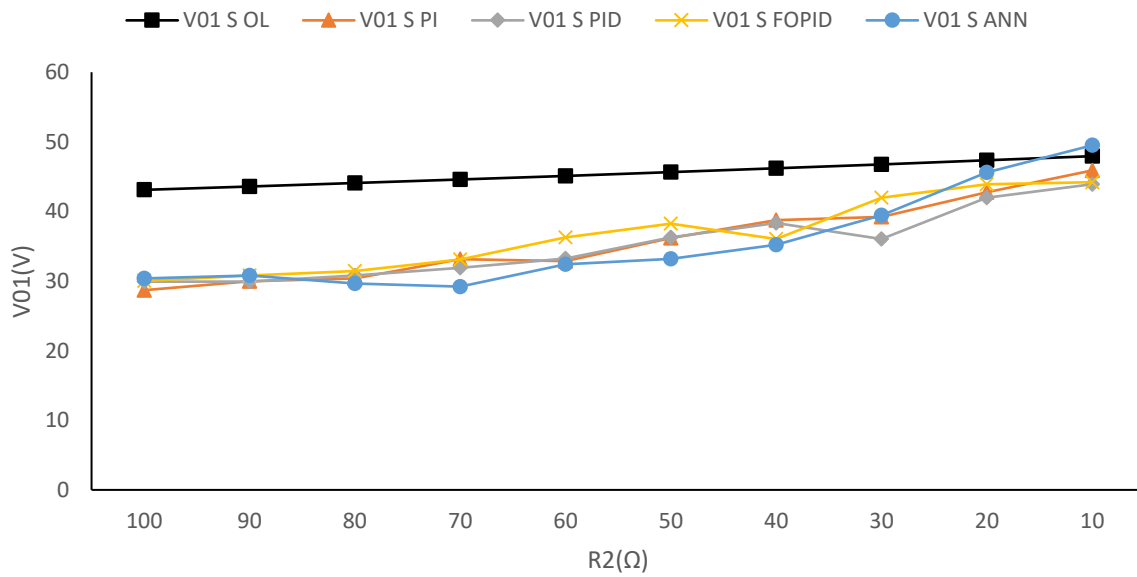


Fig. 5.27 Simulated output voltage (V_{01}) vs load (R_2) variations

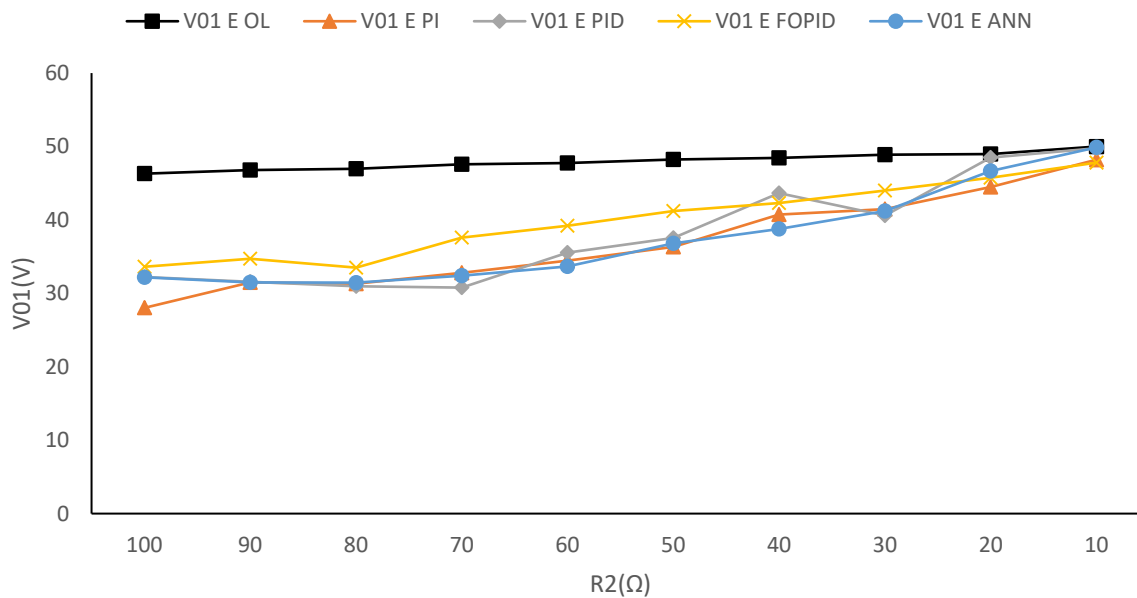


Fig. 5.28 Experimental output voltage (V_{01}) vs load (R_2) variations

The variation of output voltage (V_{01}) with load resistance (R_1 & R_2) has been shown in Fig. 5.29 and Fig. 5.30 for simulation and experimental data respectively. It can be observed in Fig. 5.29 that PID controller has the best performance as it almost keeps 30V at output whereas in Fig. 5.30 PI controller gives better results. However, due to duty constraints and inductor saturation point voltage values are not evaluated experimentally below some resistance values.

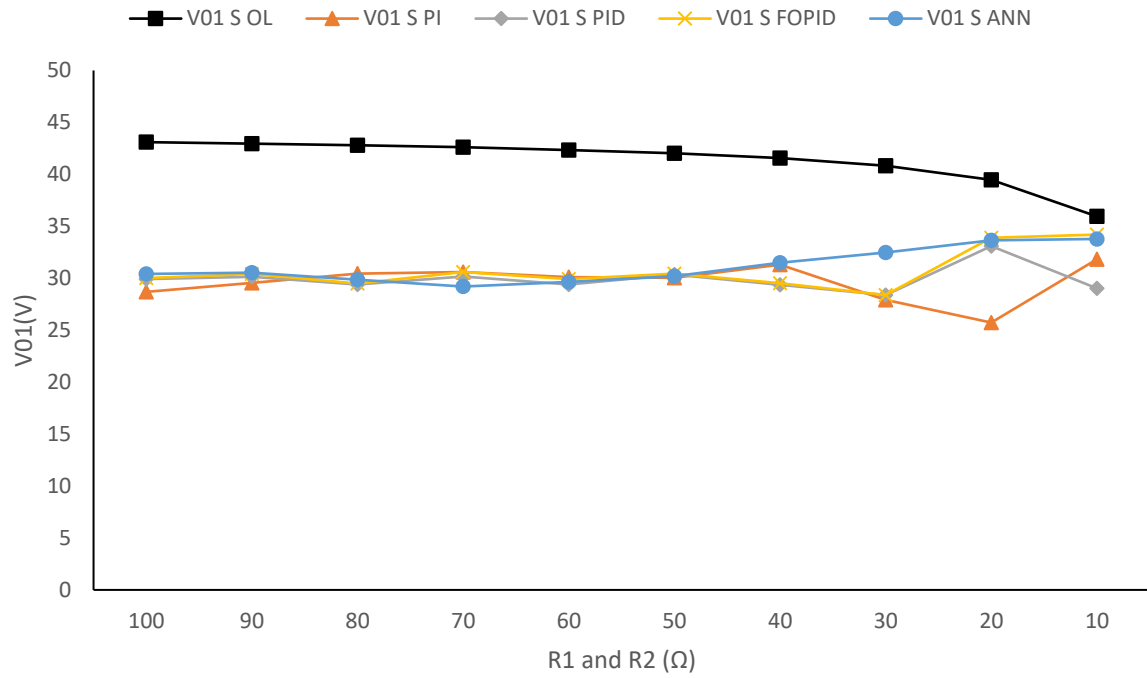


Fig. 5.29 Simulated output voltage (V_{01}) vs load (R_1 and R_2) variations

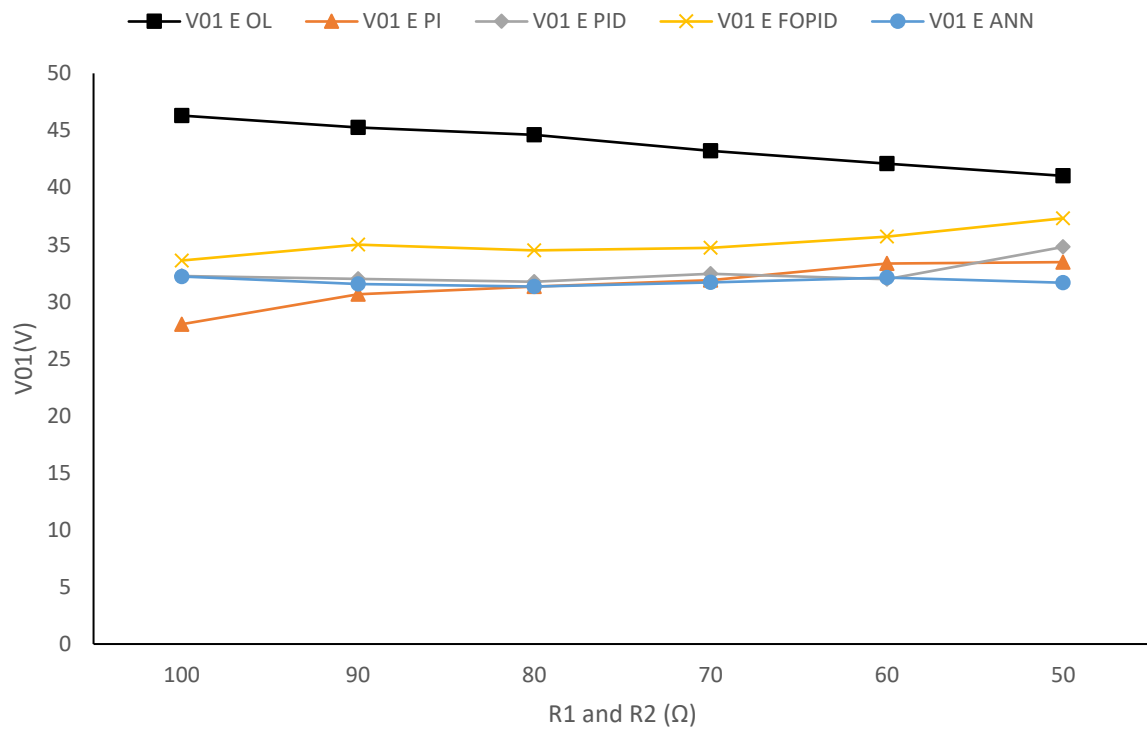


Fig. 5.30 Experimental output voltage (V_{01}) vs load (R_1 and R_2) variations

5.4.3 Performance of simulated output voltages subjected to various control algorithms

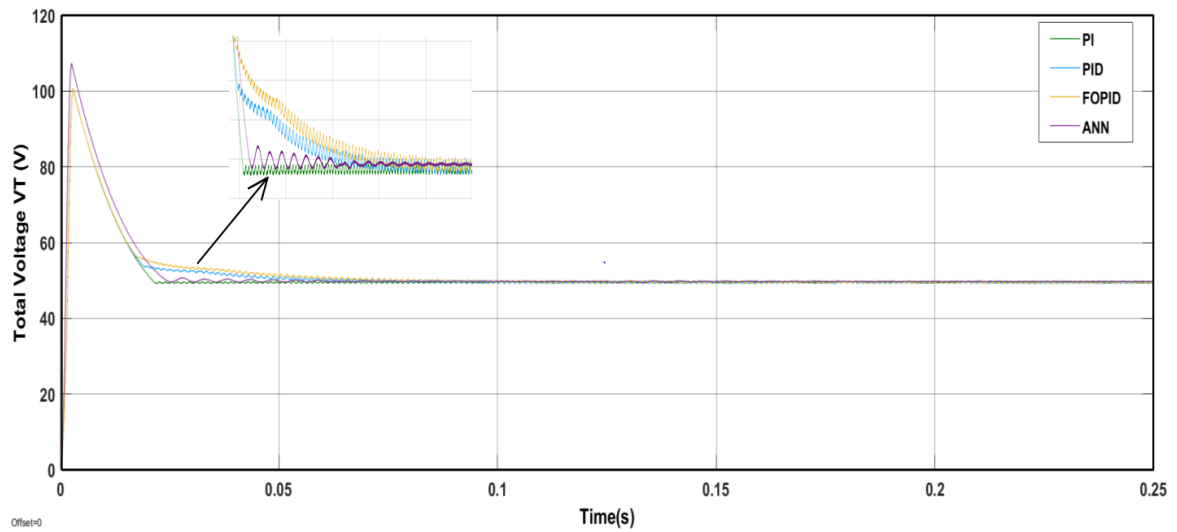


Fig. 5.31 Simulated total output voltage waveform

Figure 5.31 shows comparison of simulated output voltage (V_T). The PI control scheme reaches settling time much faster followed by ANN controller. Small sustained oscillations are present in all control schemes which are very less in case of ANN controller. PID and FOPID controllers follow almost same pattern with less oscillations than PI controller after transient period. The maximum starting peak voltage is reached by ANN controllers which is 108V whereas it is 100V for other controllers. PI controller settles in 0.024 seconds whereas other controllers settle in 0.06 seconds. The controller parameters considered here were discussed in the previous chapter.

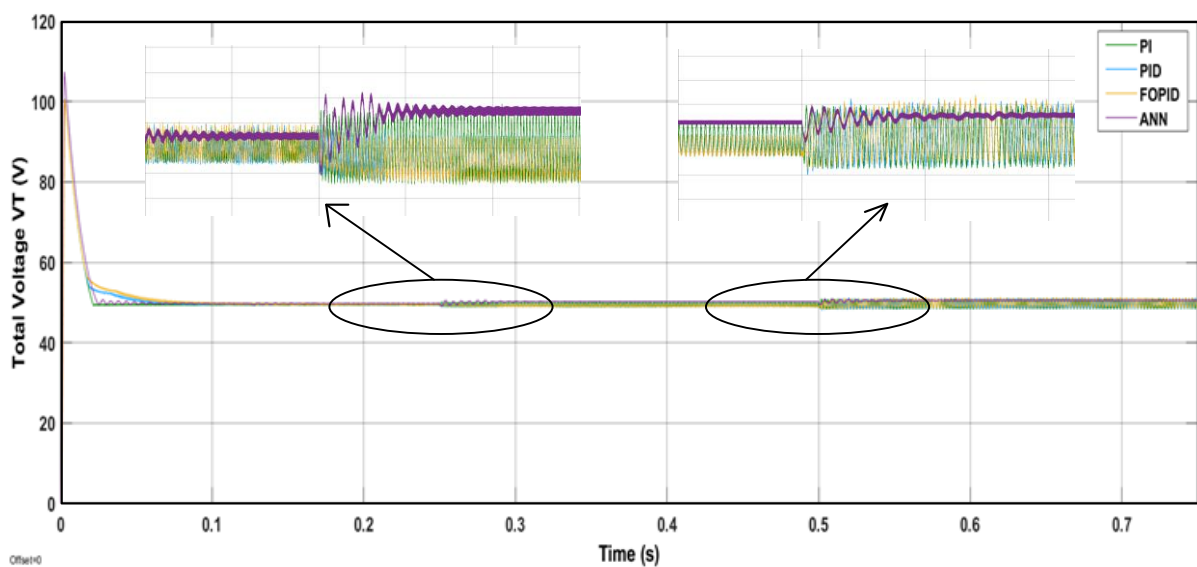


Fig. 5.32 Simulated total output voltage waveform with load switching

Figure 5.32 shows the trend of output voltage comparison as load is increased by sudden switching. The load resistance R_1 and R_2 are decreased from 100Ω to 75Ω at $t=0.25$ seconds and further decreased to 60Ω at $t=0.5$ seconds. It can be observed from the figure that output voltage remains constant but sustained oscillations are increased as in case of PI, PID and FOPID controller. PI controller has more oscillations. ANN controller settles with least oscillations at the desired setpoint voltage i.e. 50V.

5.4.4 Performance of simulated output voltages with varying control parameters

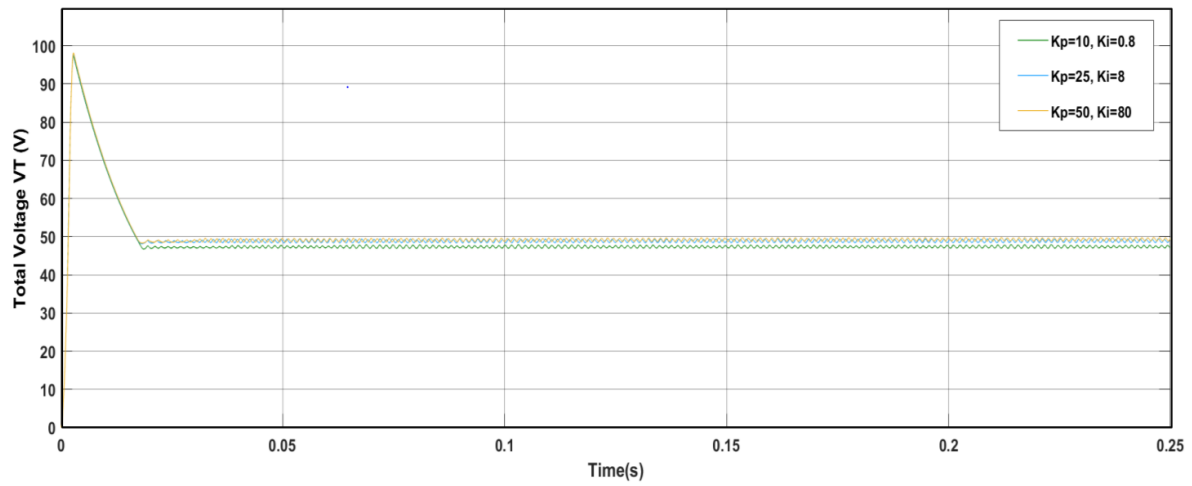


Fig. 5.33 Simulated total output voltage waveform with varying PI controller parameters

Figure 5.33 shows the trend of output voltage waveform as PI controller parameters are varied. It can be observed that on increasing K_P and K_I values sustained oscillation diminishes and setpoint voltage is reached. Further increment in parameter values results in increment of amplitude of sustained oscillations.

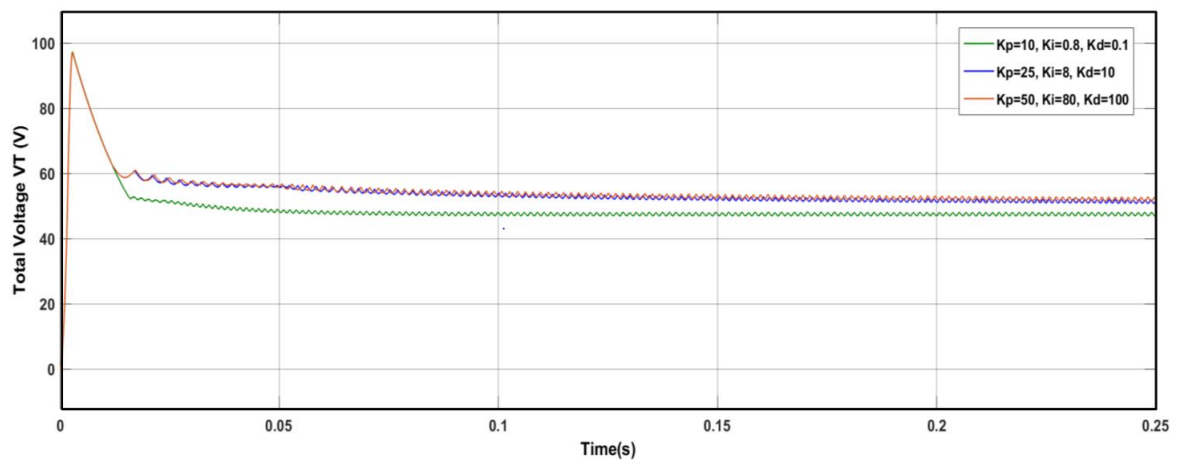


Fig. 5.34 Simulated total output voltage waveform with varying PID controller parameters

Figure 5.34 shows the trend of output voltage waveform as PID controller parameters are varied. It can be observed that on increasing K_P , K_I and K_D values sustained oscillation diminishes and setpoint voltage is reached. Further increment in parameter values results in increment of amplitude of sustained oscillations.

5.4.5 Performance of experimental output voltages subjected to various control algorithms

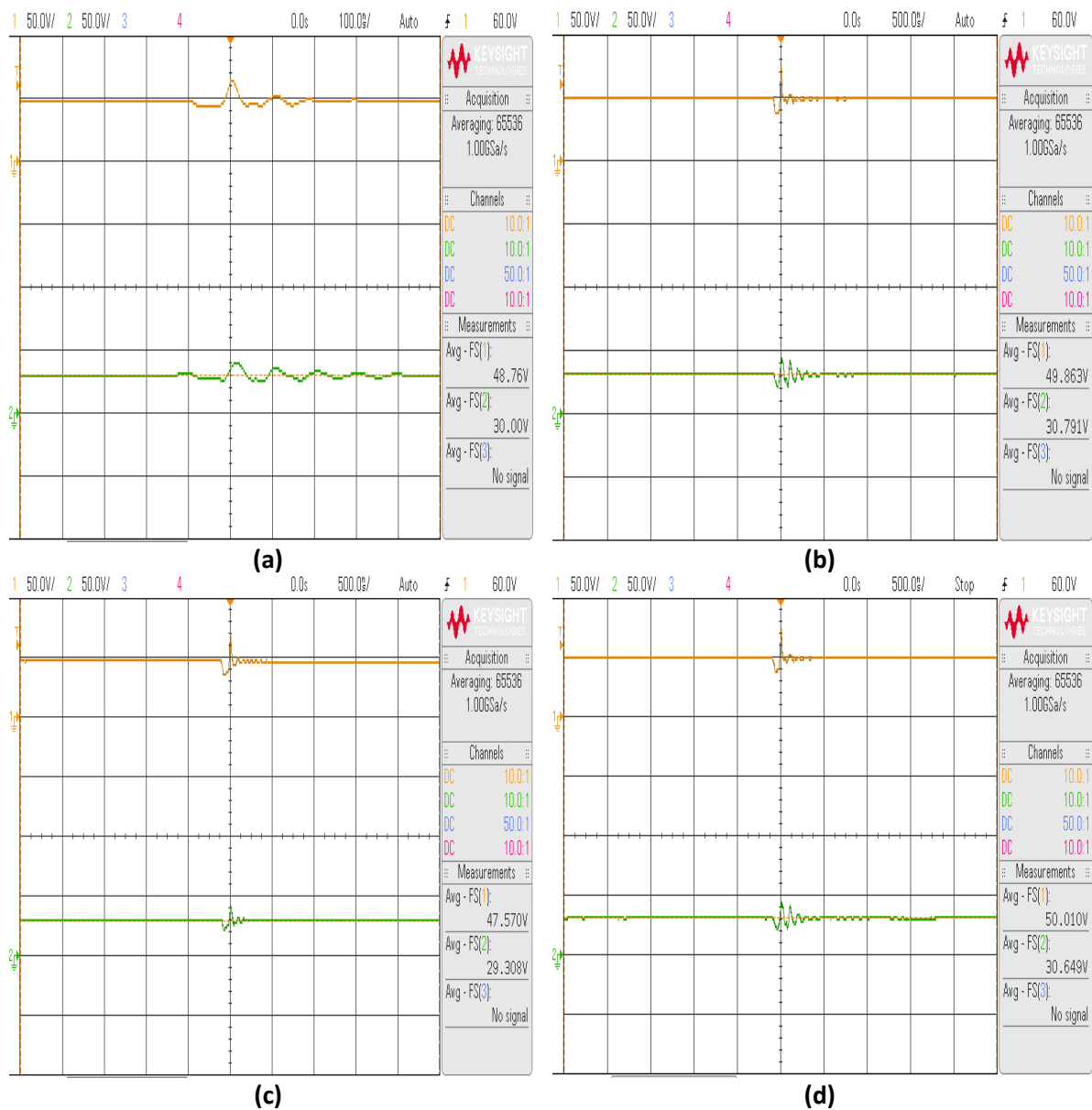


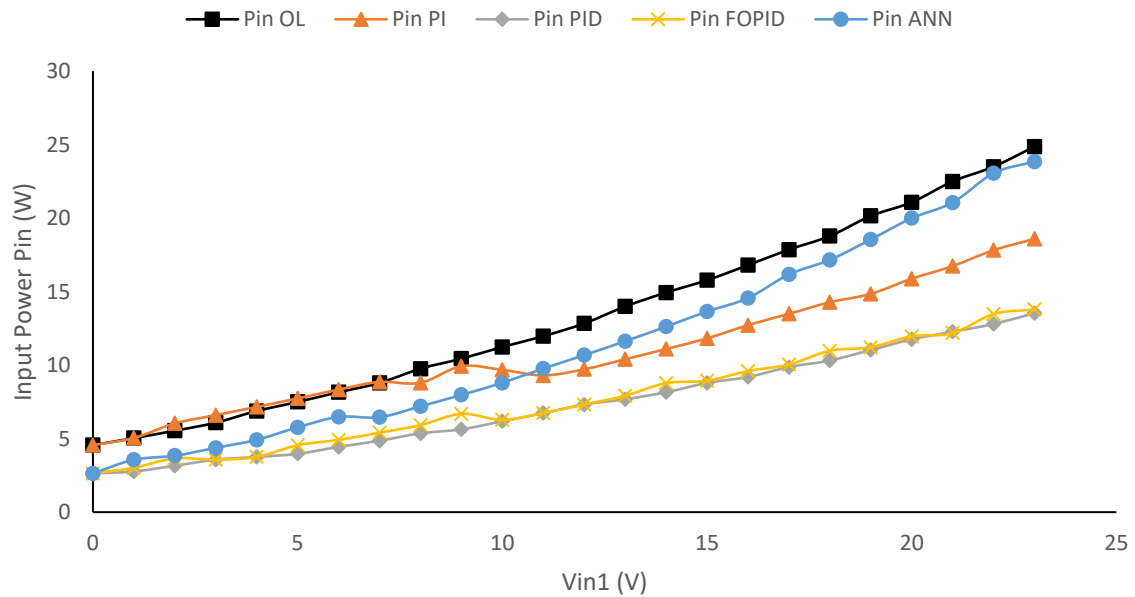
Fig. 5.35 Experimental output voltage waveforms of (a) PI controller (b) PID controller (c) FOPID controller (d) ANN controller

The experimental output voltage waveform is compared in the fig. 5.35. Figure 5.35(a) shows output voltage for PI controller, Figure 5.35(b) shows output voltage for PID controller, Figure 5.35(c) shows output voltage for FOPID controller and Figure 5.35(d) shows output voltage

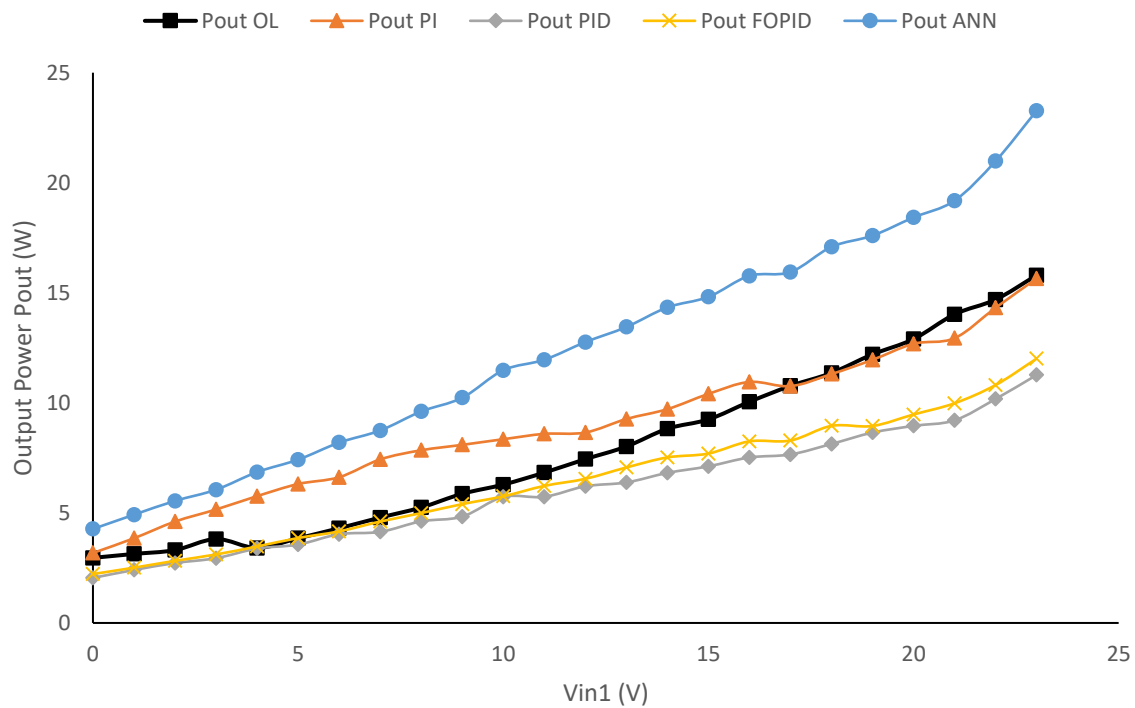
for ANN controller. It can be noticed that ANN controller settles nearest to the setpoint voltages i.e. V_T as 50V and V_{O1} as 30V. Considering V_{in1} as 18V, V_{in2} as 24V and load resistances as 100Ω each.

5.4.6 Performance of Power and Efficiency for multiport converter

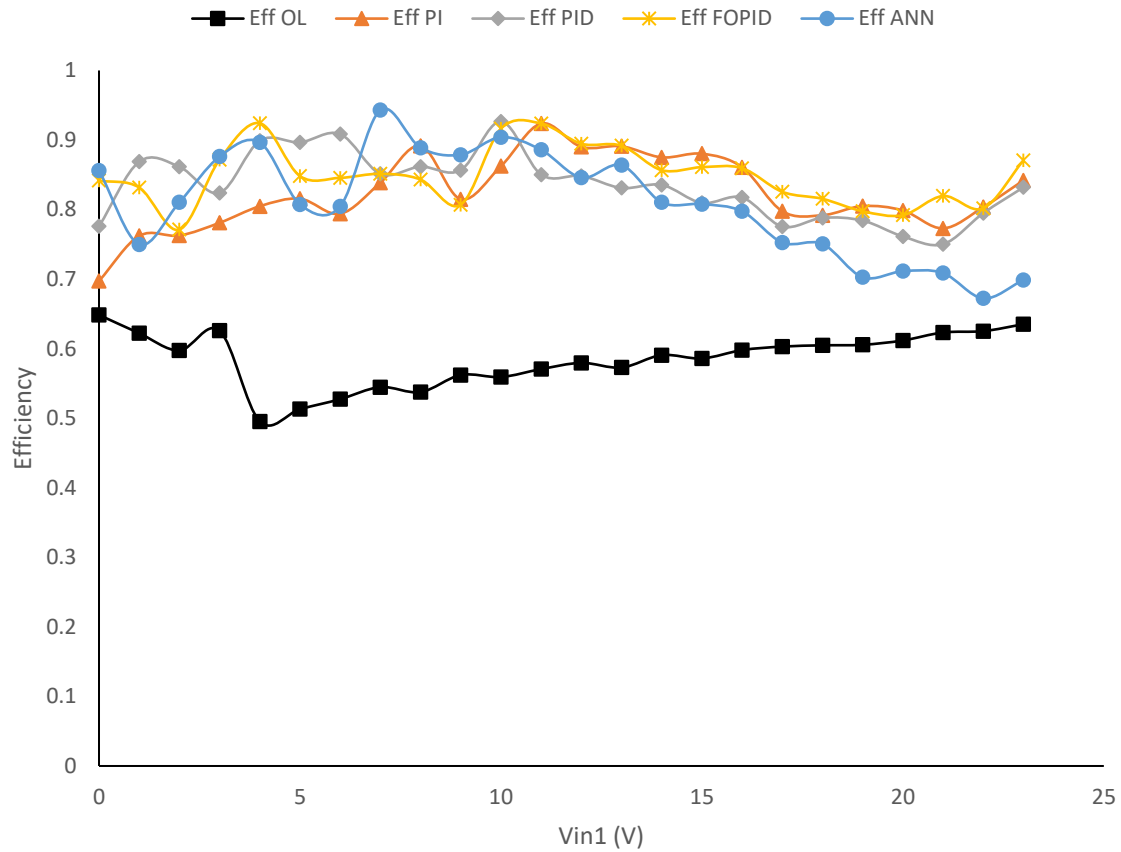
Figure 5.36 showcase the power input, power output and efficiency plots.



(a)



(b)



(c)

Fig. 5.36 Comparison of (a) input power (b) output power and (c) efficiency under various control strategies with input voltage (V_{in1}) variations keeping V_{in2} as 24V and load resistances as 100Ω each.

Figure 5.36 showcase the power input, power output and efficiency plots. The input voltage is varied accordingly. Figure 5.36 (a) shows experimental results comparison of input power, figure 5.36 (b) shows experimental results comparison of output power and figure 5.36 (c) shows experimental results comparison of efficiency considering input voltage variations. It can be clearly stated from the figure that power rating of ANN controller is much more than other control strategies whereas efficiency of PI and FOPID controller is much better. Open loop shows more input as well as output power. This is because constant duty is given to the switches of the converter which results in more voltage than the desired setpoint voltages. PI control has more efficiency for high input voltage values whereas PID control has more efficiency for low input voltage values. FOPID controller has almost same efficiency for low as well as high input voltage value. ANN controller also has more efficiency for low as well as mid voltage values.

Table 5.1 Comparison of results under different control strategies for multiport converter considering $V_{in1}=18V$, $V_{in2}=24V$ and $R_1=R_2=100\Omega$

Control Algorithm	$P_{in1}(W)$	$P_{in2}(W)$	$P_{o1}(W)$	$P_{o2}(W)$	Efficiency(%)
Open Loop	9.18	9.6	6.07	5.29	60.5
PI	6.84	7.44	7.56	3.74	79.2
PID	5.04	5.28	5.48	2.65	78.8
FOPID	5.22	5.76	6.38	3.09	79.2
ANN	10.44	6.72	9.98	2.89	75.05

The power and efficiency of the multiport converter has been examined under the influence of various control strategies. Open loop shows more input as well as output power. This is because constant duty is given to the switches of the converter which results in more voltage than the desired setpoint voltages. Among control strategies implemented, ANN controller provides more power to the output i.e. 12.88 watts but efficiency of PI and FOPID controller is much better as shown in Table 5.1. Overall efficiency of all control algorithms is more than open loop system. The abovementioned results obtained for the converter are evaluated using V_{in1} as 18V, V_{in2} as 24V and load resistances at 100 Ω each.

5.5 Summary of the Chapter

This chapter has thoroughly discussed the performance of the different control strategies implemented on the non-isolated multi-input multi-output DC-DC boost converter mentioned in previous chapter. The performance for both input variations and load variations have been evaluated through simulations as well as experimentally. Different controller parameters are considered for the evaluation of system performance. The major finding of the results will be presented in the next chapter.

This dissertation work has been done to obtain the dynamic behaviour of the non-isolated dual-input dual-output DC-DC boost converter. Various control strategies are implemented using ATmega328p microcontroller. MATLAB/Simulink based model is developed and simulated results are compared with experimental results. The converter switches were given duty using various control algorithms viz. PI, PID, FOPID and ANN and effect of input as well as load variations were scrutinized. The following conclusions were drawn from this work.

6.1 Conclusion

- The dynamic modelling of the non-isolated multi-input multi-output DC-DC boost converter has been performed mathematically as well as computationally using MATLAB/Simulink[®] environment.
- Proper designing and fabrication of the non-isolated multi-input multi-output DC-DC boost converter along with gate driver circuit using TLP 250H has been accomplished using MOSFET as switches.
- Programming of various control logics have been particularly implemented using ATmega328p (Arduino) microcontroller.
- The simulation results were obtained using MATLAB/Simulink[®] environment and have been compared with experimental results obtained from fabricated MIMO converter. Duty to the switches have been given by the driver circuit which in turn is connected to the microcontroller.
- The results are obtained for input voltage variation as well as load resistance variation. Input voltage (V_{in1}) is varied keeping V_{in2} as 12V and 24V respectively and following the condition $V_{in1} < V_{in2}$. The load resistance is varied from 100Ω to 10Ω individually and then simultaneously and proportionally.
- Among all the control strategies implemented, ANN was found to be the best control algorithm as it gives best performance in both input variation as well as load variations.

- PI and PID controllers give better results in input voltage variations whereas FOPID controller gives better results during load resistance variations.
- ANN controller has more power rating whereas PI and FOPID controller have much better efficiency.

6.2 Future Scope

- Integration of the non-isolated multi-input multi-output DC-DC boost converter with multilevel inverters can be done.
- Switching losses of each switch and fabrication costing of single converter can be determined.
- In this work, battery charging mode was theoretically examined but practical implementation is possible with design of different control parameters.
- More power rating circuit can be designed in order to meet electric vehicle requirements.

REFERENCES

- [1] X. Zhang and C. Mi, *Vehicle Power Management*, New York, NY, USA: Springer, 2011.
- [2] M. Ehsani, Y. Gao, and A. Emadi, *Modern Electric, Hybrid Electric and Fuel Cell Vehicle Fundamentals, Theory and Design*, 2nd ed., New York, NY, USA: CRC Press, 2010.
- [3] P. Thounthong, V. Chunkag, P. Sethakul, B. Davat, and M. Hinaje, "Comparative study of fuel-cell vehicle hybridization with battery or supercapacitor storage device," *IEEE Trans. Veh. Technol.*, vol. 58, no. 8, pp. 3892–3905, Oct. 2009.
- [4] L. Wang, E. G. Collins, and H. Li, "Optimal design and real-time control for energy management in electric vehicles," *IEEE Trans. Veh. Technol.*, vol. 60, no. 4, pp. 1419–1429, May 2011.
- [5] M. Zandi, A. Peyman, J. P. Martin, S. Pierfederici, B. Davat, and F. Meybody-tabar, "Energy management of a fuel cell/supercapacitor/battery power source for electric vehicular applications," *IEEE Trans. Veh. Technol.*, vol. 60, no. 2, pp. 433–443, Feb. 2011.
- [6] P. Thounthong, S. Pierfederici, and B. Davat, "Analysis of differential flatness-based control for fuel cell hybrid power source," *IEEE Trans. Energy Convers.*, vol. 25, no. 3, pp. 909–920, Sep. 2010.
- [7] A. Peyman, S. Pierfederici, F. Meybody-tabar, and B. Davat, "An adapted control strategy to minimize dc-bus capacitors of parallel fuel cell/ultracapacitor hybrid system," *IEEE Trans. Power Electron.*, vol. 26, no. 12, pp. 3843–3852, Dec. 2011.
- [8] M. Michon, J.L. Duarte, M.A.M. Hendrix, and M.G. Simes, "A three port bidirectional converter for hybrid fuel cell systems," in *Proc. 35th Annual IEEE Power Electron. Spec. Conf.*, Aachen, Germany, 2004, pp.4736– 4741.
- [9] J. L. Duarte, M. Hendrix, and M. G. Simoes, "Three-port bidirectional converter for hybrid fuel cell systems," *IEEE Trans. Power Electron.*, vol. 22, no. 2, pp. 480–487, Mar. 2007.
- [10] H. Tao, A. Kotsopoulos, J.L. Duarte, and M.A.M. Hendrix, "Transformer coupled multiport ZVS bidirectional DC–DC converter with wide input range," *IEEE Trans. Power Electron.*, vol. 23, no. 2, pp. 771–781, Mar. 2008.
- [11] H. Tao, A. Kotsopoulos, J. L. Duarte, and M. A. M. Hendrix, "Family of multiport bidirectional DC–DC converters," *Inst. Electr. Eng. Proc. Elect. Power Appl.*, vol. 153, no. 3, pp. 451–458, May 2006.
- [12] H. Tao, J. Duarte, and M. Hendrix, "Three-port triple-half-bridge bidirectional converter with zero-voltage switching," *IEEE Trans. Power Electron.*, vol. 23, no. 2, pp. 782–792, Mar. 2008.
- [13] H. Krishnaswami and N. Mohan, "Three-port series-resonant DC–DC converter to interface renewable energy sources with bidirectional load and energy storage ports," *IEEE Trans. Power Electron.*, vol. 24, no. 10, pp. 2289–2297, Oct. 2009.
- [14] R. Ahmadi and M. Ferdowsi, "Double-input converter on h-bridge cells: derivation, small-signal modelling, and power sharing analysis" *IEEE Trans. Circuit Syst.*, vol. 59, no. 4, pp. 875–889, Apr. 2012.

- [15] V. A. K. Prabhala, D. Somayajula and M. Ferdowsi, "Power sharing in a double-input buck converter using dead-time control," in Proc. Energy Convers. Congr. Expo., 2009.
- [16] Z. Li, O. Onar, and A. Khaligh, "Design and control of a multiple input DC/DC Converter for battery/ultra capacitor based electric vehicle power system" in Proc. IEEE Twenty-Fourth Annu. Appl. Power Electron. Conf. Expo., 2009.
- [17] K. Gummi and M. Ferdowsi, "Double-input DC-DC power electronic converters for electric-drive vehicles –topology exploration and synthesis using a single-pole triple-throw switch," IEEE Trans. Ind. Electron., vol. 57, no. 2, pp. 617–621, Feb. 2010.
- [18] S.M. Dehghan, M. Mohamadian, A. Yazdian, and F. Ashrafzadeh, "Dual input dual-output Z-source inverter," IEEE Trans. PowerElectron., vol. 25, no. 2, pp. 360–368, Feb. 2010.
- [19] T. Bhattacharya, V. S. Giri, K. Mathew, and L. Umanand, "Multiphase bidirectional flyback converter topology for hybrid electric vehicles," IEEE Trans. Ind. Electron., vol. 56, no. 1, pp. 78–83, Jan. 2009.
- [20] F. Nejabatkhah, S. Danyali, S.H. Hosseini, M. Sabahi, and S.A. Mozaffari Niapour, "Modelling and control of a new three-input DC–DC Boost converter for hybrid PV/FC/battery power system," IEEE Trans. Power Electron., vol. 27, no. 5, pp. 2309–2325, May 2012.
- [21] Y. C. Liu and Y. M. Chen, "A systematic approach to synthesizing multi-input DC–DC converters," IEEE Trans. Power Electron., vol. 24, no. 1, pp. 116–127, Jan. 2009.
- [22] O. C. Onar and A. Khaligh, "A novel integrated magnetic structure based DC/DC converter for hybrid battery/ultracapacitor energy storage systems," IEEE Trans. Smart Grid, vol. 3, no. 1, pp. 296–308, Mar. 2012.
- [23] H. Wu, K. S. Ding, and Y. Xing, "Topology derivation of non-isolated three-port DC–DC converters from DIC and DOC," IEEE Trans. Power Electron., vol. 28, no. 7, pp. 3297–3307, Jul. 2013.
- [24] S. Danyali, S.H. Hosseini, and G. B. Gharehpetian, "New extendable single stage multi-input DC–DC/AC boost converter," IEEE Trans. Power Electron., vol. 29, no. 2, pp. 775–788, Feb. 2014.
- [25] A. Nami, F. Zare, A. Ghosh, and F. Blaabjerg, "Multi-output DC–DC converters based on diode-clamped converters configuration: Topology and control strategy," IET Power Electron., vol. 3, pp. 197–208, 2010.
- [26] A. A. Boora, A. Nami, F. Zare, A. Ghosh, and F. Blaabjerg, "Voltage sharing converter to supply single-phase asymmetrical four-level diode clamped inverter with high power factor load," IEEE Trans. Power Electron., vol. 25, no. 10, pp. 2507–2521, Oct. 2010.
- [27] J. D. Dasika, B. Bahrani, M. Saeedifard, A. Karimi, and A. Rufer, "Multivariable control of single-inductor dual-output buck converters," IEEE Trans. Power Electron., vol. 29, no. 4, pp. 2061–2070, Apr. 2014.
- [28] H. Behjati and A. Davoudi, "A MIMO topology with series outputs: An interface between diversified energy sources and diode-clamped multilevel inverter," in Proc. Appl. Power Electron. Conf. Expo., 2012.

- [29] H. Behjatmand, A. Davoudi, "A multi-port DC–DC converter with independent outputs for vehicular applications," in Proc. Vehicle Power Propulsion Conf., 2011.
- [30] R.W. Erickson and D. Maksimovic, Fundamentals of Power Electronics. 2nd ed., New York, NY, USA: Kluwer Academic Publisher, 2000.

APPENDIX A

EXPERIMENTAL SETUP

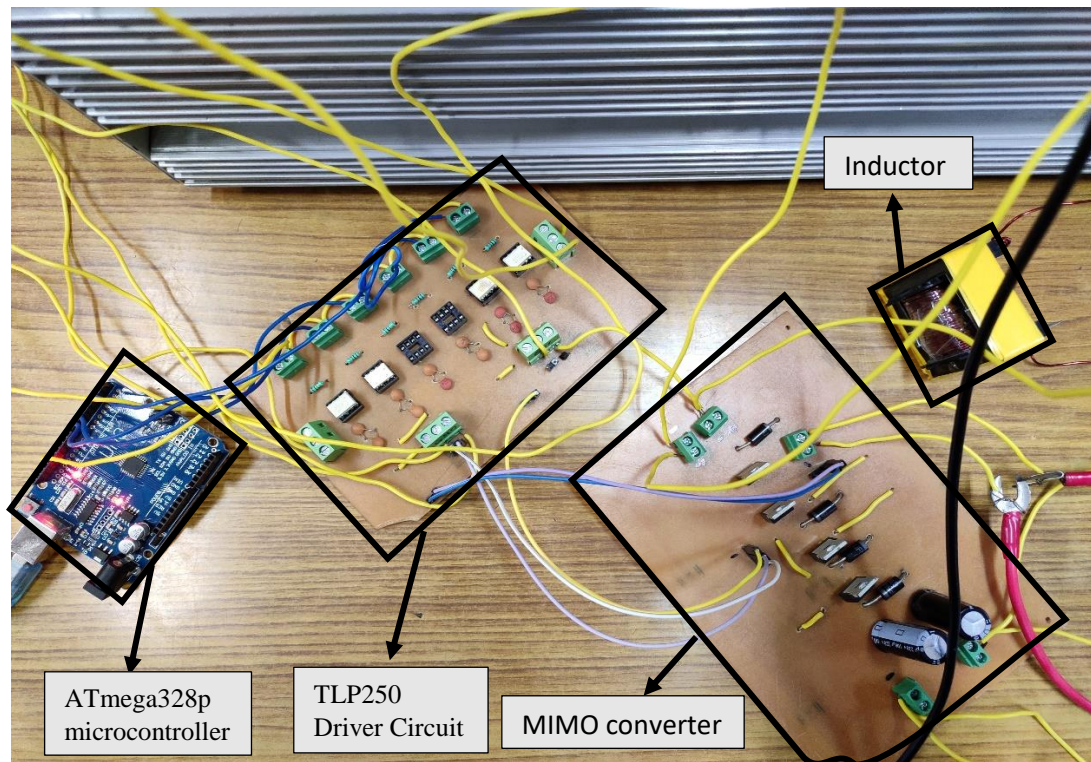


Fig. A.1 PCB driver and converter circuit

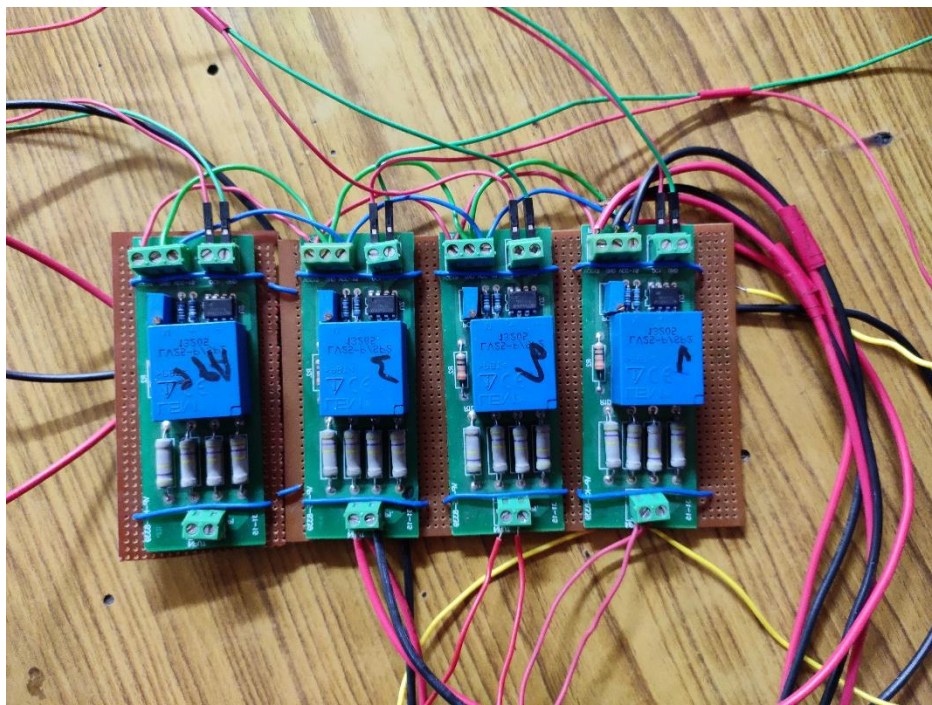


Fig. A.2 Voltage sensor circuit

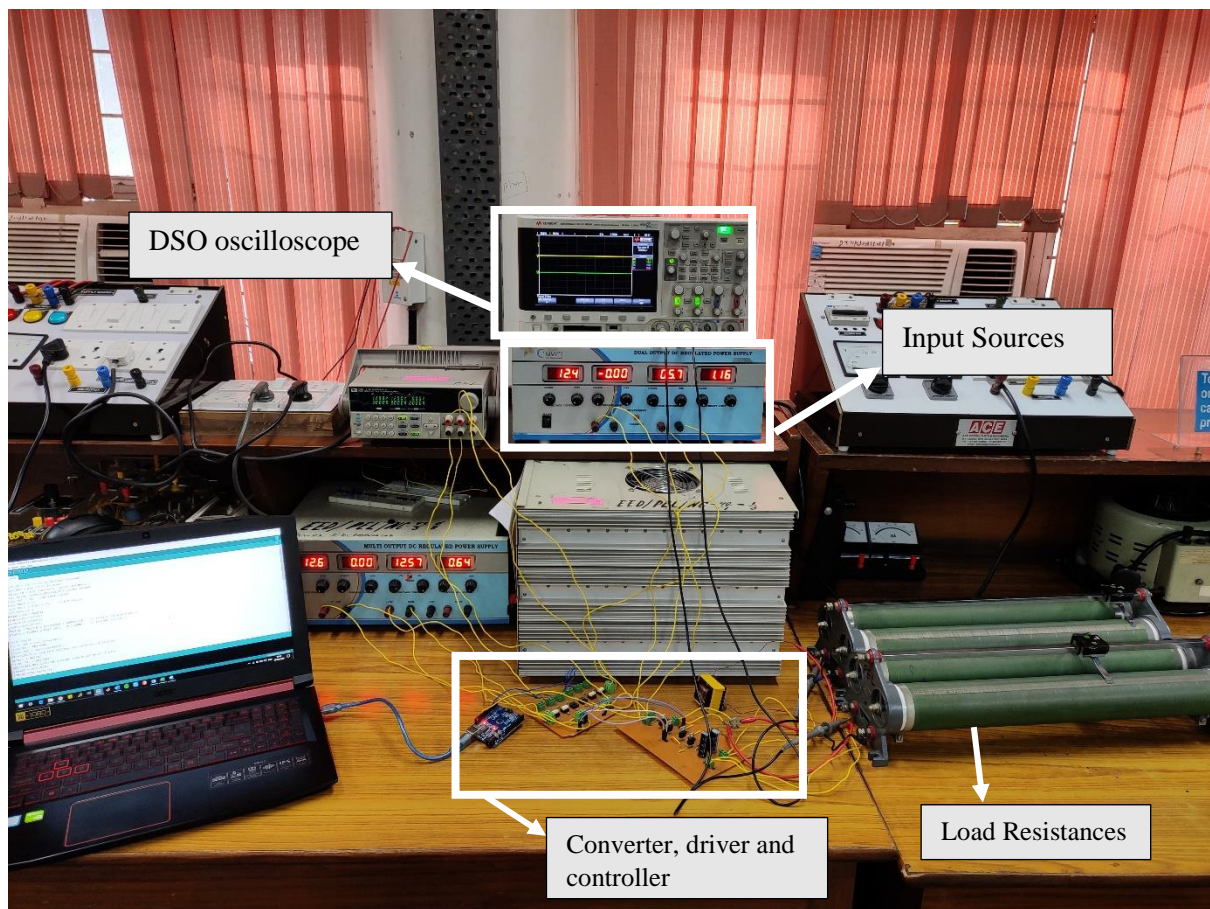


Fig. A.3 Experimental setup

APPENDIX B

PCB DESIGN CIRUITS

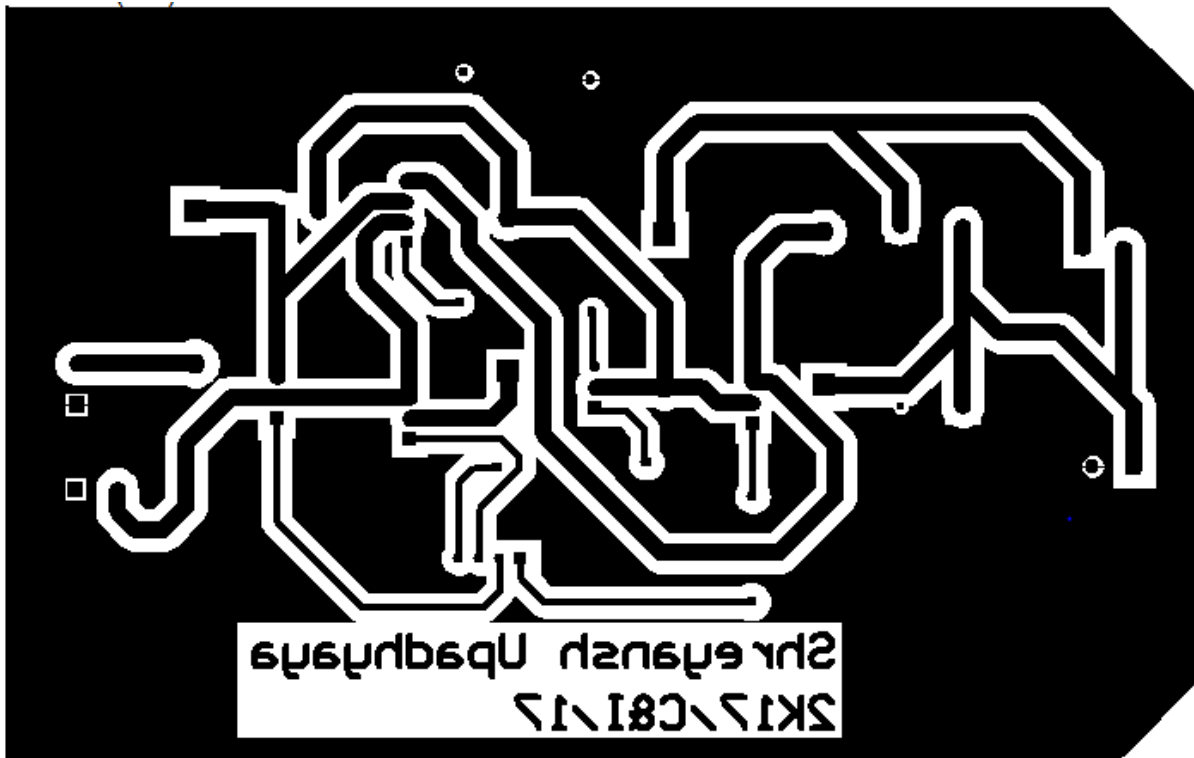


Fig. B.1 PCB for MIMO converter

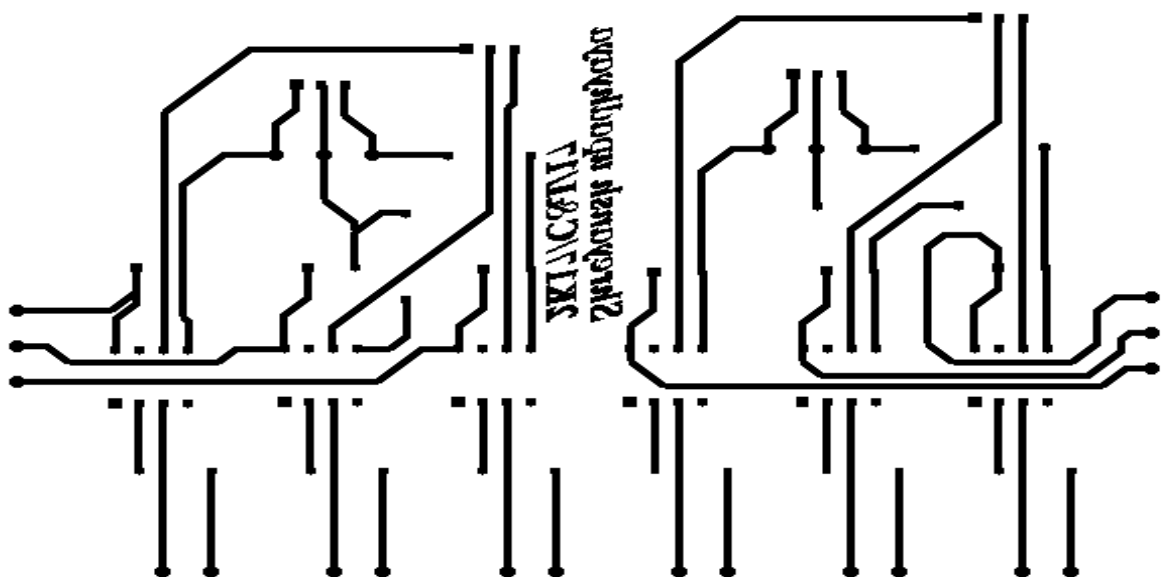


Fig. B.2 PCB for driver circuit

APPENDIX C

DATASHEET OF MOSFET

International
IR Rectifier

- Advanced Process Technology
- Dynamic dv/dt Rating
- 175°C Operating Temperature
- Fast Switching
- Fully Avalanche Rated
- Ease of Paralleling
- Simple Drive Requirements

Description

Fifth Generation HEXFET® Power MOSFETs from International Rectifier utilize advanced processing techniques to achieve extremely low on-resistance per silicon area. This benefit, combined with the fast switching speed and ruggedized device design that HEXFET Power MOSFETs are well known for, provides the designer with an extremely efficient and reliable device for use in a wide variety of applications.

The TO-220 package is universally preferred for all commercial-industrial applications at power dissipation levels to approximately 50 watts. The low thermal resistance and low package cost of the TO-220 contribute to its wide acceptance throughout the industry.

The D²Pak is a surface mount power package capable of accommodating die sizes up to HEX-4. It provides the highest power capability and the lowest possible on-resistance in any existing surface mount package. The D²Pak is suitable for high current applications because of its low internal connection resistance and can dissipate up to 2.0W in a typical surface mount application.

The through-hole version (IRF640NL) is available for low-profile application.

Absolute Maximum Ratings

	Parameter	Max.	Units
$I_D @ T_C = 25^\circ\text{C}$	Continuous Drain Current, $V_{GS} @ 10\text{V}$	18	A
$I_D @ T_C = 100^\circ\text{C}$	Continuous Drain Current, $V_{GS} @ 10\text{V}$	13	
I_{DM}	Pulsed Drain Current ①	72	
$P_D @ T_C = 25^\circ\text{C}$	Power Dissipation	150	W
	Linear Derating Factor	1.0	W/°C
V_{GS}	Gate-to-Source Voltage	± 20	V
E_{AS}	Single Pulse Avalanche Energy ②	247	mJ
I_{AR}	Avalanche Current ①	18	A
E_{AR}	Repetitive Avalanche Energy ①	15	mJ
dv/dt	Peak Diode Recovery dv/dt ⑥	8.1	V/ns
T_J	Operating Junction and	-55 to +175	°C
T_{STG}	Storage Temperature Range		
	Soldering Temperature, for 10 seconds		
	Mounting torque, 6-32 or M3 screw ④		

www.irf.com

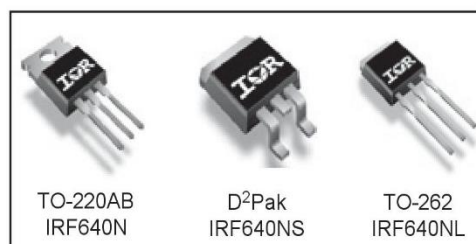
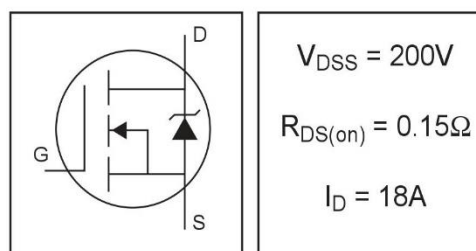
PD - 94006A

IRF640N

IRF640NS

IRF640NL

HEXFET® Power MOSFET

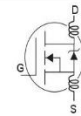


IRF640N/S/L

International
IR Rectifier

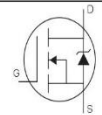
Electrical Characteristics @ $T_J = 25^\circ\text{C}$ (unless otherwise specified)

	Parameter	Min.	Typ.	Max.	Units	Conditions
$V_{(BR)DSS}$	Drain-to-Source Breakdown Voltage	200	—	—	V	$V_{GS} = 0V, I_D = 250\mu A$
$\Delta V_{(BR)DSS}/\Delta T_J$	Breakdown Voltage Temp. Coefficient	—	0.25	—	V/ $^\circ\text{C}$	Reference to 25°C , $I_D = 1mA$
$R_{DS(on)}$	Static Drain-to-Source On-Resistance	—	—	0.15	Ω	$V_{GS} = 10V, I_D = 11A$ ③
$V_{GS(th)}$	Gate Threshold Voltage	2.0	—	4.0	V	$V_{DS} = V_{GS}, I_D = 250\mu A$
g_{fs}	Forward Transconductance	6.8	—	—	S	$V_{DS} = 50V, I_D = 11A$ ③
I_{DSS}	Drain-to-Source Leakage Current	—	—	25	μA	$V_{DS} = 200V, V_{GS} = 0V$
		—	—	250		$V_{DS} = 160V, V_{GS} = 0V, T_J = 150^\circ\text{C}$
I_{GSS}	Gate-to-Source Forward Leakage	—	—	100	nA	$V_{GS} = 20V$
	Gate-to-Source Reverse Leakage	—	—	-100		$V_{GS} = -20V$
Q_g	Total Gate Charge	—	—	67	nC	$I_D = 11A$
Q_{gs}	Gate-to-Source Charge	—	—	11		$V_{DS} = 160V$
Q_{gd}	Gate-to-Drain ("Miller") Charge	—	—	33		$V_{GS} = 10V$, See Fig. 6 and 13
$t_{d(on)}$	Turn-On Delay Time	—	10	—	ns	$V_{DD} = 100V$
t_r	Rise Time	—	19	—		$I_D = 11A$
$t_{d(off)}$	Turn-Off Delay Time	—	23	—		$R_G = 2.5\Omega$
t_f	Fall Time	—	5.5	—		$R_D = 9.0\Omega$, See Fig. 10 ③
L_D	Internal Drain Inductance	—	4.5	—	nH	Between lead, 6mm (0.25in.) from package and center of die contact
L_S	Internal Source Inductance	—	7.5	—		
C_{iss}	Input Capacitance	—	1160	—	pF	$V_{GS} = 0V$
C_{oss}	Output Capacitance	—	185	—		$V_{DS} = 25V$
C_{rss}	Reverse Transfer Capacitance	—	53	—		$f = 1.0MHz$, See Fig. 5



Source-Drain Ratings and Characteristics

	Parameter	Min.	Typ.	Max.	Units	Conditions
I_S	Continuous Source Current (Body Diode)	—	—	18	A	MOSFET symbol showing the integral reverse p-n junction diode.
I_{SM}	Pulsed Source Current (Body Diode) ①	—	—	72		
V_{SD}	Diode Forward Voltage	—	—	1.3	V	$T_J = 25^\circ\text{C}, I_S = 11A, V_{GS} = 0V$ ③
t_{rr}	Reverse Recovery Time	—	167	251	ns	$T_J = 25^\circ\text{C}, I_F = 11A$
Q_{rr}	Reverse Recovery Charge	—	929	1394	nC	$di/dt = 100A/\mu s$ ③
t_{on}	Forward Turn-On Time	Intrinsic turn-on time is negligible (turn-on is dominated by $L_S + L_D$)				



Thermal Resistance

	Parameter	Typ.	Max.	Units
$R_{\theta JC}$	Junction-to-Case	—	1.0	$^\circ\text{C/W}$
$R_{\theta CS}$	Case-to-Sink, Flat, Greased Surface ④	0.50	—	
$R_{\theta JA}$	Junction-to-Ambient ④	—	62	
$R_{\theta JA}$	Junction-to-Ambient (PCB mount) ⑤	—	40	

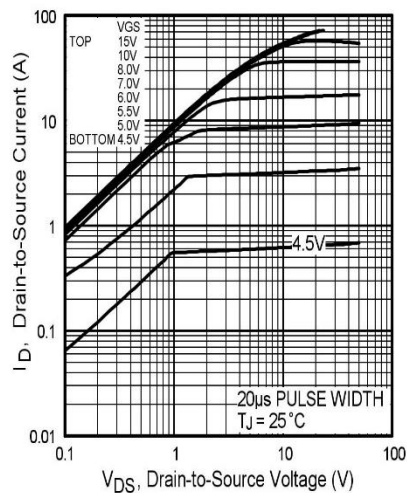


Fig 1. Typical Output Characteristics

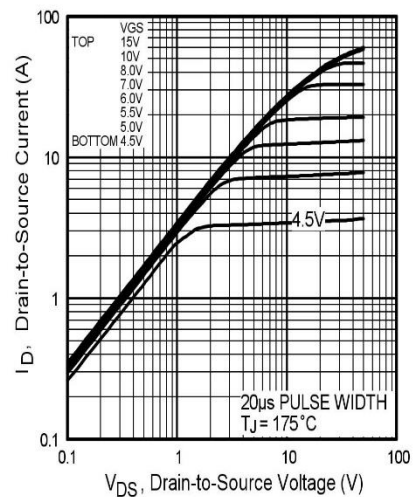


Fig 2. Typical Output Characteristics

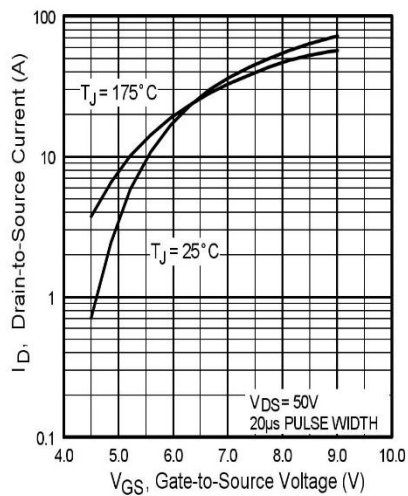


Fig 3. Typical Transfer Characteristics

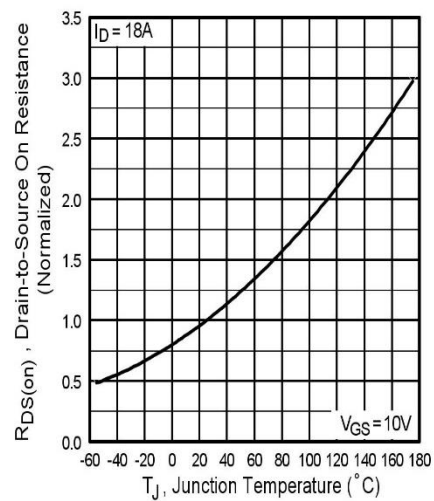


Fig 4. Normalized On-Resistance
Vs. Temperature

IRF640N/S/L

International
IR Rectifier

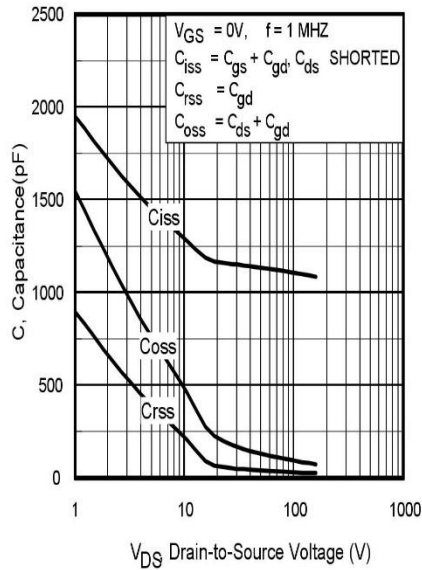


Fig 5. Typical Capacitance Vs. Drain-to-Source Voltage

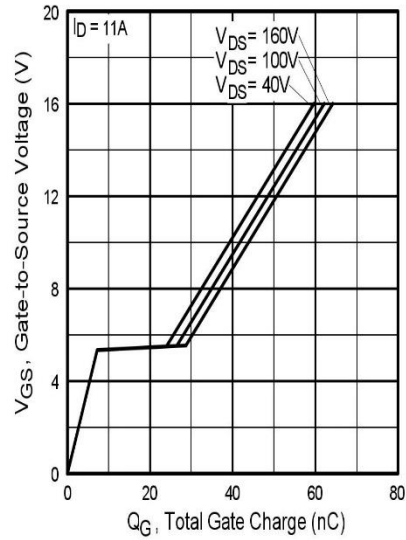


Fig 6. Typical Gate Charge Vs. Gate-to-Source Voltage

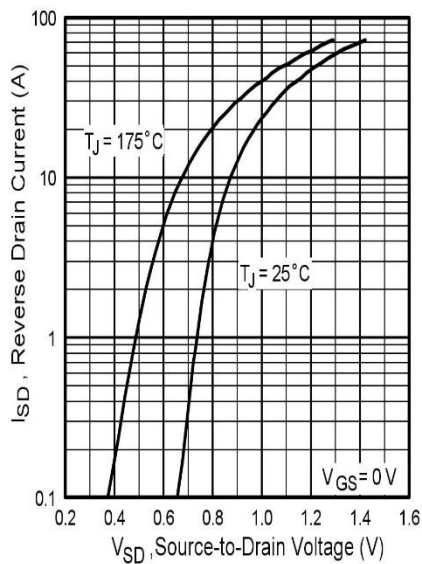


Fig 7. Typical Source-Drain Diode Forward Voltage

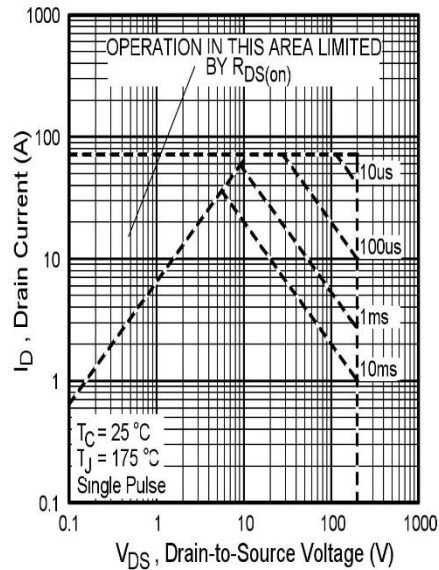


Fig 8. Maximum Safe Operating Area

APPENDIX D

DATASHEET OF DRIVER IC

TOSHIBA

TLP250H, TLP250HF

Photocouplers GaAs infrared LED & Photo IC

TLP250H, TLP250HF

1. Applications

- Industrial Inverters
- Air Conditioner Inverters
- IGBT Gate Drivers
- MOSFET Gate Drivers
- Induction Cooktop and Home Appliances

2. General

The TLP250H is a photocoupler in a DIP8 package that consists of a GaAs infrared light-emitting diode (LED) optically coupled to an integrated high-gain, high-speed photodetector IC chip. It provides guaranteed performance and specifications at temperatures up to 125 °C. The TLP250H has an internal Faraday shield that provides a guaranteed Common-mode transient immunity of ± 40 kV/ μ s. It has a totem-pole output that can both sink and source current. The TLP250H is ideal for IGBT and power MOSFET gate drive.

3. Features

- (1) Buffer logic type (totem pole output)
- (2) Output peak current: ± 2.5 A (max)
- (3) Operating temperature: -40 to 125 °C
- (4) Supply current: 3 mA (max)
- (5) Supply voltage: 10 to 30 V
- (6) Threshold input current: 5 mA (max)
- (7) Propagation delay time: 500 ns (max)
- (8) Common-mode transient immunity: ± 40 kV/ μ s (min)
- (9) Isolation voltage: 3750 Vrms (min)
- (10) Safety standards

UL-approved: UL1577, File No.E67349

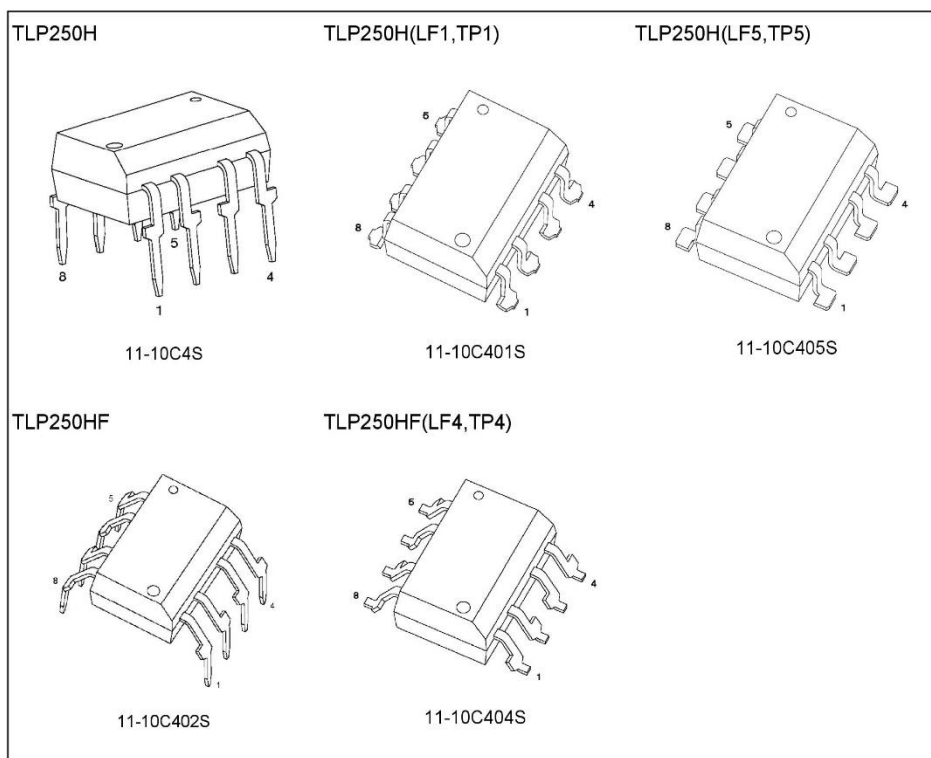
cUL-approved: CSA Component Acceptance Service No.5A File No.E67349

VDE-approved: EN60747-5-5, EN60065 or EN60950-1 (Note 1)

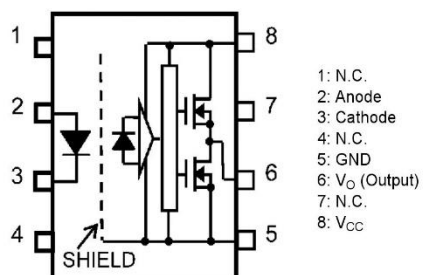
Note 1: When a VDE approved type is needed, please designate the Option (D4).

Start of commercial production

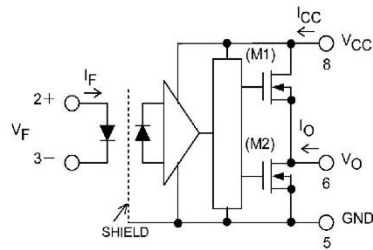
2012-09

4. Packaging (Note)


Note: Through-hole type: TLP250H, TLP250HF
 Lead forming option: (LF1), (LF4), (LF5)
 Taping option: (TP1), (TP4), (TP5)

5. Pin Assignment


6. Internal Circuit (Note)



Note: A 0.1- μ F bypass capacitor must be connected between pin 8 and pin 5.

7. Principle of Operation

7.1. Truth Table

Input	LED	M1	M2	Output
H	ON	ON	OFF	H
L	OFF	OFF	ON	L

7.2. Mechanical Parameters

Characteristics	7.62-mm Pitch TLP250H	10.16-mm Pitch TLP250HF	Unit
Creepage distances	7.0 (min)	8.0 (min)	mm
Clearance distances	7.0 (min)	8.0 (min)	
Internal isolation thickness	0.4 (min)	0.4 (min)	

8. Absolute Maximum Ratings (Note) (Unless otherwise specified, $T_a = 25\text{ }^{\circ}\text{C}$)

	Characteristics	Symbol	Note	Rating	Unit
LED	Input forward current	I_F		20	mA
	Input forward current derating ($T_a \geq 110\text{ }^{\circ}\text{C}$)	$\Delta I_F / \Delta T_a$		-0.54	mA/ $^{\circ}\text{C}$
	Peak transient input forward current	I_{FPT}	(Note 1)	1	A
	Peak transient input forward current derating ($T_a \geq 110\text{ }^{\circ}\text{C}$)	$\Delta I_{FPT} / \Delta T_a$		-25	mA/ $^{\circ}\text{C}$
	Input reverse voltage	V_R		6	V
	Input power dissipation	P_D		40	mW
	Input power dissipation derating ($T_a \geq 110\text{ }^{\circ}\text{C}$)	$\Delta P_D / \Delta T_a$		-1.0	mW/ $^{\circ}\text{C}$
Detector	Peak high-level output current ($T_a = -40\text{ to }125\text{ }^{\circ}\text{C}$)	I_{OPH}	(Note 2)	-2.5	A
	Peak low-level output current ($T_a = -40\text{ to }125\text{ }^{\circ}\text{C}$)	I_{OPL}	(Note 2)	+2.5	
	Output voltage	V_O		35	V
	Supply voltage	V_{CC}		35	
	Output power dissipation	P_O		260	mW
	Output power dissipation derating ($T_a \geq 110\text{ }^{\circ}\text{C}$)	$\Delta P_O / \Delta T_a$		-2.0	mW/ $^{\circ}\text{C}$
Common	Operating temperature	T_{opr}		-40 to 125	$^{\circ}\text{C}$
	Storage temperature	T_{stg}		-55 to 150	
	Lead soldering temperature (10 s)	T_{sol}	(Note 3)	260	
	Isolation voltage AC, 60 s, R.H. $\leq 60\%$	BV_S	(Note 4)	3750	Vrms

Note: Using continuously under heavy loads (e.g. the application of high temperature/current/voltage and the significant change in temperature, etc.) may cause this product to decrease in the reliability significantly even if the operating conditions (i.e. operating temperature/current/voltage, etc.) are within the absolute maximum ratings.

Please design the appropriate reliability upon reviewing the Toshiba Semiconductor Reliability Handbook ("Handling Precautions"/"Derating Concept and Methods") and individual reliability data (i.e. reliability test report and estimated failure rate, etc).

Note 1: Pulse width (PW) $\leq 1\text{ }\mu\text{s}$, 300 pps

Note 2: Exponential waveform. Pulse width $\leq 0.2\text{ }\mu\text{s}$, $f \leq 15\text{ kHz}$, $V_{CC} = 20\text{ V}$, $T_a = -40\text{ to }125\text{ }^{\circ}\text{C}$
Exponential waveform. Pulse width $\leq 0.08\text{ }\mu\text{s}$, $f \leq 25\text{ kHz}$, $V_{CC} = 15\text{ V}$, $T_a = -40\text{ to }125\text{ }^{\circ}\text{C}$

Note 3: $\geq 2\text{ mm}$ below seating plane.

Note 4: This device is considered as a two-terminal device: Pins 1, 2, 3 and 4 are shorted together, and pins 5, 6, 7 and 8 are shorted together.

APPENDIX E

DATASHEET OF DIODE



UF5400 – UF5408

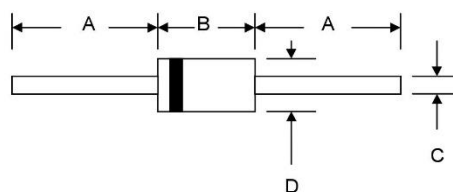
3.0A ULTRAFAST DIODE

Features

- Diffused Junction
- Low Forward Voltage Drop
- High Current Capability
- High Reliability
- High Surge Current Capability

Mechanical Data

- Case: DO-201AD, Molded Plastic
- Terminals: Plated Leads Solderable per MIL-STD-202, Method 208
- Polarity: Cathode Band
- Weight: 1.2 grams (approx.)
- Mounting Position: Any
- Marking: Type Number
- **Lead Free: For RoHS / Lead Free Version, Add “-LF” Suffix to Part Number, See Page 4**



DO-201AD		
Dim	Min	Max
A	25.4	—
B	7.20	9.50
C	1.20	1.30
D	4.80	5.30
All Dimensions in mm		

Maximum Ratings and Electrical Characteristics @T_A=25°C unless otherwise specified

Single Phase, half wave, 60Hz, resistive or inductive load.
For capacitive load, derate current by 20%.

Characteristic	Symbol	UF 5400	UF 5401	UF 5402	UF 5403	UF 5404	UF 5406	UF 5407	UF 5408	Unit
Peak Repetitive Reverse Voltage Working Peak Reverse Voltage DC Blocking Voltage	V_{RRM} V_{RWM} V_R	50	100	200	300	400	600	800	1000	V
RMS Reverse Voltage	$V_{R(RMS)}$	35	70	140	210	280	420	560	700	V
Average Rectified Output Current (Note 1) @T _A = 55°C	I _O	3.0								A
Non-Repetitive Peak Forward Surge Current 8.3ms Single half sine-wave superimposed on rated load (JEDEC Method)	I _{FSM}	150								A
Forward Voltage @I _F = 3.0A	V _{FM}	1.0				1.3	1.7			V
Peak Reverse Current @T _A = 25°C At Rated DC Blocking Voltage @T _A = 100°C	I _{RM}	10 100								μA
Reverse Recovery Time (Note 2)	t _{rr}	50					75			nS
Typical Junction Capacitance (Note 3)	C _j	80					50			pF
Operating Temperature Range	T _J	-65 to +125								°C
Storage Temperature Range	T _{STG}	-65 to +150								°C

Note: 1. Leads maintained at ambient temperature at a distance of 9.5mm from the case
2. Measured with I_F = 0.5A, I_R = 1.0A, I_{RR} = 0.25A. See figure 5.
3. Measured at 1.0 MHz and applied reverse voltage of 4.0V D.C.

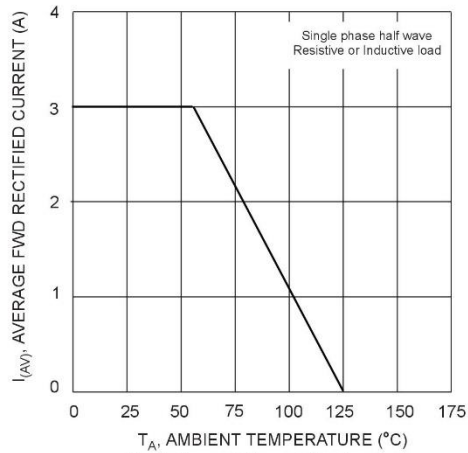


Fig. 1 Forward Current Derating Curve

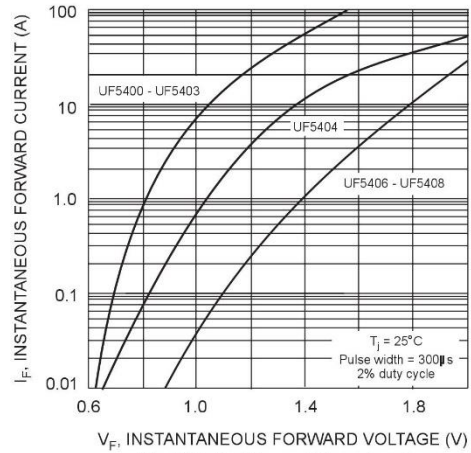


Fig. 2 Typical Forward Characteristics

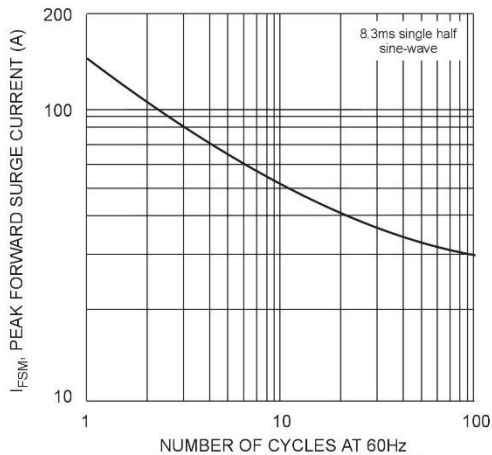


Fig. 3 Peak Forward Surge Current

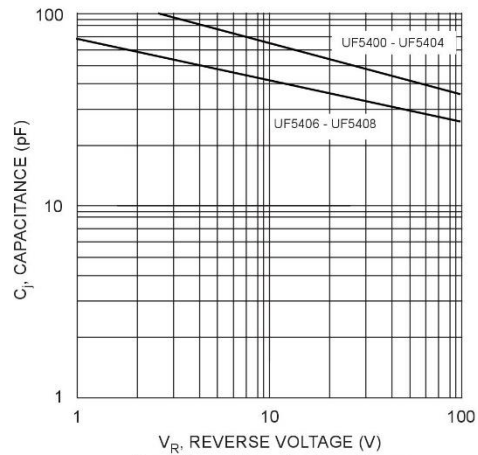
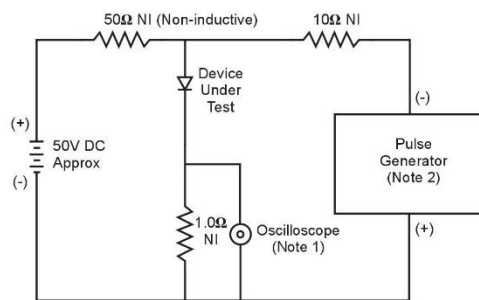


Fig. 4 Typical Junction Capacitance



- Notes:
1. Rise Time = 7.0ns max. Input Impedance = 1.0MΩ, 22pF.
 2. Rise Time = 10ns max. Input Impedance = 50Ω.

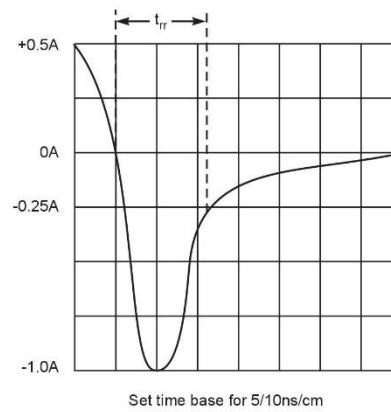
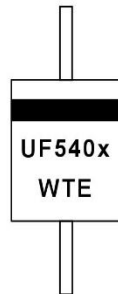


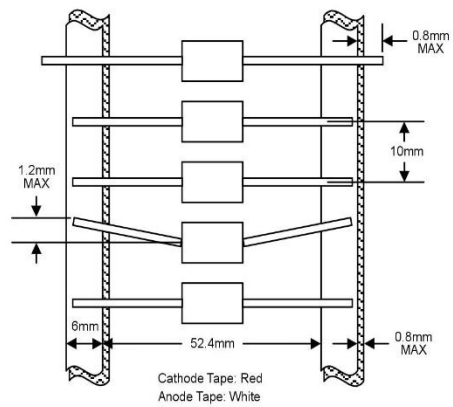
Fig. 5 Reverse Recovery Time Characteristic and Test Circuit

MARKING INFORMATION



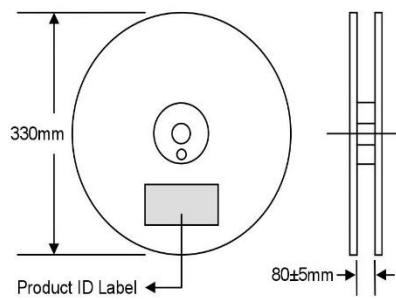
Cathode = Polarity Band
 UF540x = Device Number
 x = 0, 1, 2, 3, 4, 6, 7 or 8
 WTE = Manufacturer's Logo

TAPING SPECIFICATIONS

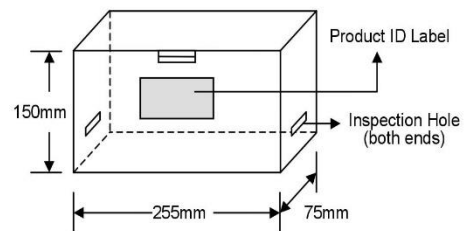


PACKAGING INFORMATION

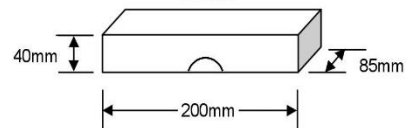
TAPE & REEL



TAPE & BOX



BULK



Packaging	Reel Diameter / Box Size (mm)	Quantity (PCS)	Carton Size (mm)	Quantity (PCS)	Approx. Gross Weight (KG)
TAPE & REEL	330	1,200	370 x 370 x 420	6,000	10.0
TAPE & BOX	255 x 75 x 150	1,200	400 x 273 x 415	12,000	17.0
BULK	200 x 85 x 40	500	459 x 214 x 256	12,500	16.0

Note: 1. Paper reel, white or gray color. Core material: plastic or metal.
 2. Components are packed in accordance with EIA standard RS-296-E.

ORDERING INFORMATION

Product No.	Package Type	Shipping Quantity
UF5400-T3	DO-201AD	1200/Tape & Reel
UF5400-TB	DO-201AD	1200/Tape & Box
UF5400	DO-201AD	500 Units/Box
UF5401-T3	DO-201AD	1200/Tape & Reel
UF5401-TB	DO-201AD	1200/Tape & Box
UF5401	DO-201AD	500 Units/Box
UF5402-T3	DO-201AD	1200/Tape & Reel
UF5402-TB	DO-201AD	1200/Tape & Box
UF5402	DO-201AD	500 Units/Box
UF5403-T3	DO-201AD	1200/Tape & Reel
UF5403-TB	DO-201AD	1200/Tape & Box
UF5403	DO-201AD	500 Units/Box
UF5404-T3	DO-201AD	1200/Tape & Reel
UF5404-TB	DO-201AD	1200/Tape & Box
UF5404	DO-201AD	500 Units/Box
UF5406-T3	DO-201AD	1200/Tape & Reel
UF5406-TB	DO-201AD	1200/Tape & Box
UF5406	DO-201AD	500 Units/Box
UF5407-T3	DO-201AD	1200/Tape & Reel
UF5407-TB	DO-201AD	1200/Tape & Box
UF5407	DO-201AD	500 Units/Box
UF5408-T3	DO-201AD	1200/Tape & Reel
UF5408-TB	DO-201AD	1200/Tape & Box
UF5408	DO-201AD	500 Units/Box

1. Products listed in **bold** are WTE Preferred devices.
2. Shipping quantity given is for minimum packing quantity only. For minimum order quantity, please consult the Sales Department.
3. To order RoHS / Lead Free version (with Lead Free finish), add "-LF" suffix to part number above. For example, **UF5400-TB-LF**.

Won-Top Electronics Co., Ltd (WTE) has checked all information carefully and believes it to be correct and accurate. However, WTE cannot assume any responsibility for inaccuracies. Furthermore, this information does not give the purchaser of semiconductor devices any license under patent rights to manufacturer. WTE reserves the right to change any or all information herein without further notice.

WARNING: DO NOT USE IN LIFE SUPPORT EQUIPMENT. WTE power semiconductor products are not authorized for use as critical components in life support devices or systems without the express written approval.

Won-Top Electronics Co., Ltd.
 No. 44 Yu Kang North 3rd Road, Chine Chen Dist., Kaohsiung, Taiwan
Phone: 886-7-822-5408 or 886-7-822-5410
Fax: 886-7-822-5417
Email: sales@wontop.com
Internet: http://www.wontop.com

We power your everyday.

APPENDIX F

ARDUINO UNO

Arduino Uno



Arduino Uno R3 Front

Arduino Uno R3 Back



Arduino Uno R2 Front

Arduino Uno SMD

Arduino Uno Front

Arduino Uno Back

Overview

The Arduino Uno is a microcontroller board based on the ATmega328 ([datasheet](#)). It has 14 digital input/output pins (of which 6 can be used as PWM outputs), 6 analog inputs, a 16 MHz ceramic resonator, a USB connection, a power jack, an ICSP header, and a reset button. It contains everything needed to support the microcontroller; simply connect it to a computer with a USB cable or power it with a AC-to-DC adapter or battery to get started.

The Uno differs from all preceding boards in that it does not use the FTDI USB-to-serial driver chip. Instead, it features the Atmega16U2 (Atmega8U2 up to version R2) programmed as a USB-to-serial converter.

[Revision 2](#) of the Uno board has a resistor pulling the 8U2 HWB line to ground, making it easier to put into DFU mode.

[Revision 3](#) of the board has the following new features:

- 1.0 pinout: added SDA and SCL pins that are near to the AREF pin and two other new pins placed near to the RESET pin, the IOREF that allow the shields to adapt to the voltage provided from the board. In future, shields will be compatible both with the board that use the AVR, which operate with 5V and with the Arduino Due that operate with 3.3V. The second one is a not connected pin, that is reserved for future purposes.
- Stronger RESET circuit.
- Atmega 16U2 replace the 8U2.

"Uno" means one in Italian and is named to mark the upcoming release of Arduino 1.0. The Uno and version 1.0 will be the reference versions of Arduino, moving forward. The Uno is the latest in a series of USB Arduino boards, and the reference model for the Arduino platform; for a comparison with previous versions, see the [index of Arduino boards](#).

Summary

Microcontroller	ATmega328
Operating Voltage	5V
Input Voltage (recommended)	7-12V

Input Voltage (limits)	6-20V
Digital I/O Pins	14 (of which 6 provide PWM output)
Analog Input Pins	6
DC Current per I/O Pin	40 mA
DC Current for 3.3V Pin	50 mA
Flash Memory	32 KB (ATmega328) of which 0.5 KB used by bootloader
SRAM	2 KB (ATmega328)
EEPROM	1 KB (ATmega328)
Clock Speed	16 MHz

Schematic & Reference Design

EAGLE files: [arduino-uno-Rev3-reference-design.zip](#) (NOTE: works with Eagle 6.0 and newer)

Schematic: [arduino-uno-Rev3-schematic.pdf](#)

Note: The Arduino reference design can use an Atmega8, 168, or 328. Current models use an ATmega328, but an Atmega8 is shown in the schematic for reference. The pin configuration is identical on all three processors.

Power

The Arduino Uno can be powered via the USB connection or with an external power supply. The power source is selected automatically.

External (non-USB) power can come either from an AC-to-DC adapter (wall-wart) or battery. The adapter can be connected by plugging a 2.1mm center-positive plug into the board's power jack. Leads from a battery can be inserted in the Gnd and Vin pin headers of the POWER connector.

The board can operate on an external supply of 6 to 20 volts. If supplied with less than 7V, however, the 5V pin may supply less than five volts and the board may be unstable. If using more than 12V, the voltage regulator may overheat and damage the board. The recommended range is 7 to 12 volts.

The power pins are as follows:

- **VIN.** The input voltage to the Arduino board when it's using an external power source (as opposed to 5 volts from the USB connection or other regulated power source). You can supply voltage through this pin, or, if supplying voltage via the power jack, access it through this pin.
- **5V.** This pin outputs a regulated 5V from the regulator on the board. The board can be supplied with power either from the DC power jack (7 - 12V), the USB connector (5V), or the VIN pin of the board (7-12V). Supplying voltage via the 5V or 3.3V pins bypasses the regulator, and can damage your board. We don't advise it.
- **3V3.** A 3.3 volt supply generated by the on-board regulator. Maximum current draw is 50 mA.
- **GND.** Ground pins.

Memory

The ATmega328 has 32 KB (with 0.5 KB used for the bootloader). It also has 2 KB of SRAM and 1 KB of EEPROM (which can be read and written with the [EEPROM library](#)).

Input and Output

Each of the 14 digital pins on the Uno can be used as an input or output, using [pinMode\(\)](#), [digitalWrite\(\)](#), and [digitalRead\(\)](#) functions. They operate at 5 volts. Each pin can provide or receive a maximum of 40 mA and has an internal pull-up resistor (disconnected by default) of 20-50 kOhms. In addition, some pins have specialized functions:

- **Serial: 0 (RX) and 1 (TX).** Used to receive (RX) and transmit (TX) TTL serial data. These pins are connected to the corresponding pins of the ATmega8U2 USB-to-TTL Serial chip.
- **External Interrupts: 2 and 3.** These pins can be configured to trigger an interrupt on a low value, a rising or falling edge, or a change in value. See the [attachInterrupt\(\)](#) function for details.
- **PWM: 3, 5, 6, 9, 10, and 11.** Provide 8-bit PWM output with the [analogWrite\(\)](#) function.

- **SPI: 10 (SS), 11 (MOSI), 12 (MISO), 13 (SCK).** These pins support SPI communication using the [SPI library](#).
- **LED: 13.** There is a built-in LED connected to digital pin 13. When the pin is HIGH value, the LED is on, when the pin is LOW, it's off.

The Uno has 6 analog inputs, labeled A0 through A5, each of which provide 10 bits of resolution (i.e. 1024 different values). By default they measure from ground to 5 volts, though it is possible to change the upper end of their range using the AREF pin and the [analogReference\(\)](#) function. Additionally, some pins have specialized functionality:

- **TWI: A4 or SDA pin and A5 or SCL pin.** Support TWI communication using the [Wire library](#).

There are a couple of other pins on the board:

- **AREF.** Reference voltage for the analog inputs. Used with [analogReference\(\)](#).
- **Reset.** Bring this line LOW to reset the microcontroller. Typically used to add a reset button to shields which block the one on the board.

See also the [mapping between Arduino pins and ATmega328 ports](#). The mapping for the Atmega8, 168, and 328 is identical.

Communication

The Arduino Uno has a number of facilities for communicating with a computer, another Arduino, or other microcontrollers. The ATmega328 provides UART TTL (5V) serial communication, which is available on digital pins 0 (RX) and 1 (TX). An ATmega16U2 on the board channels this serial communication over USB and appears as a virtual com port to software on the computer. The '16U2 firmware uses the standard USB COM drivers, and no external driver is needed. However, [on Windows, a .inf file is required](#). The Arduino software includes a serial monitor which allows simple textual data to be sent to and from the Arduino board. The RX and TX LEDs on the board will flash when data is being transmitted via the USB-to-serial chip and USB connection to the computer (but not for serial communication on pins 0 and 1).

A [SoftwareSerial library](#) allows for serial communication on any of the Uno's digital pins.

The ATmega328 also supports I2C (TWI) and SPI communication. The Arduino software includes a Wire library to simplify use of the I2C bus; see the [documentation](#) for details. For SPI communication, use the [SPI library](#).

Programming

The Arduino Uno can be programmed with the Arduino software ([download](#)). Select "Arduino Uno" from the **Tools > Board** menu (according to the microcontroller on your board). For details, see the [reference](#) and [tutorials](#).

The ATmega328 on the Arduino Uno comes preburned with a [bootloader](#) that allows you to upload new code to it without the use of an external hardware programmer. It communicates using the original STK500 protocol ([reference](#), [C header files](#)).

You can also bypass the bootloader and program the microcontroller through the ICSP (In-Circuit Serial Programming) header; see [these instructions](#) for details.

The ATmega16U2 (or 8U2 in the rev1 and rev2 boards) firmware source code is available. The ATmega16U2/8U2 is loaded with a DFU bootloader, which can be activated by:

- On Rev1 boards: connecting the solder jumper on the back of the board (near the map of Italy) and then resetting the 8U2.
- On Rev2 or later boards: there is a resistor that pulling the 8U2/16U2 HWB line to ground, making it easier to put into DFU mode.

You can then use [Atmel's FLIP software](#) (Windows) or the [DFU programmer](#) (Mac OS X and Linux) to load a new firmware. Or you can use the ISP header with an external programmer (overwriting the DFU bootloader). See [this user-contributed tutorial](#) for more information.

Automatic (Software) Reset

Rather than requiring a physical press of the reset button before an upload, the Arduino Uno is designed in a way that allows it to be reset by software running on a connected computer. One of the hardware flow control lines (DTR) of the ATmega8U2/16U2 is connected to the reset line of the ATmega328 via a 100 nanofarad capacitor. When this line is asserted (taken low), the reset line drops long enough to reset the chip. The Arduino software uses this capability to allow you to upload code by simply pressing the upload button in the Arduino environment. This means that the bootloader can have a shorter timeout, as the lowering of DTR can be well-coordinated with the start of the upload. This setup has other implications. When the Uno is connected to either a computer running Mac OS X or Linux, it resets each time a connection is made to it from software (via USB). For the following half-second or so, the bootloader is running on the Uno. While it is programmed to ignore malformed data (i.e. anything besides an upload of new code), it will intercept the first few bytes of data sent to the board after a connection is opened. If a sketch running on the board receives one-time configuration or other data when it first starts, make sure that the software with which it communicates waits a second after opening the connection and before sending this data. The Uno contains a trace that can be cut to disable the auto-reset. The pads on either side of the trace can be soldered together to re-enable it. It's labeled "RESET-EN". You may also be able to disable the auto-reset by connecting a 110 ohm resistor from 5V to the reset line; see [this forum thread](#) for details.

USB Overcurrent Protection

The Arduino Uno has a resettable polyfuse that protects your computer's USB ports from shorts and overcurrent. Although most computers provide their own internal protection, the fuse provides an extra layer of protection. If more than 500 mA is applied to the USB port, the fuse will automatically break the connection until the short or overload is removed.

Physical Characteristics

The maximum length and width of the Uno PCB are 2.7 and 2.1 inches respectively, with the USB connector and power jack extending beyond the former dimension. Four screw holes allow the board to be attached to a surface or case. Note that the distance between digital pins 7 and 8 is 160 mil (0.16"), not an even multiple of the 100 mil spacing of the other pins.

APPENDIX G

DATASHEET OF VOLTAGE SENSOR



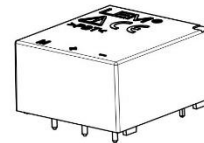
Voltage Transducer LV 25-P

For the electronic measurement of currents: DC, AC, pulsed..., with galvanic separation between the primary circuit and the secondary circuit.



$$I_{PN} = 10 \text{ mA}$$

$$V_{PN} = 10 \dots 500 \text{ V}$$



Electrical data

I_{PN}	Primary nominal rms current	10	mA
I_{PM}	Primary current, measuring range	0 .. ± 14	mA
R_M	Measuring resistance	$R_{M \min}$ $R_{M \max}$	
	with $\pm 12 \text{ V}$	@ $\pm 10 \text{ mA}_{\max}$	30 190 Ω
		@ $\pm 14 \text{ mA}_{\max}$	30 100 Ω
	with $\pm 15 \text{ V}$	@ $\pm 10 \text{ mA}_{\max}$	100 350 Ω
		@ $\pm 14 \text{ mA}_{\max}$	100 190 Ω
I_{SN}	Secondary nominal rms current	25	mA
K_N	Conversion ratio	2500 : 1000	
U_C	Supply voltage ($\pm 5 \%$)	$\pm 12 \dots 15$	V
I_C	Current consumption	10 (@ $\pm 15 \text{ V}$) + I_S	mA

Accuracy - Dynamic performance data

X_S	Overall accuracy @ I_{PN} $T_A = 25^\circ\text{C}$ @ $\pm 12 \dots 15 \text{ V}$	± 0.9	%
	@ $\pm 15 \text{ V}$ ($\pm 5 \%$)	± 0.8	%
ε_L	Linearity error	< 0.2	%
I_O	Offset current @ $I_P = 0$, $T_A = 25^\circ\text{C}$	Typ Max	
I_{OT}	Temperature variation of I_O	0 $^\circ\text{C}$.. + 25 $^\circ\text{C}$	± 0.06 ± 0.25 mA
	+ 25 $^\circ\text{C}$.. + 70 $^\circ\text{C}$	± 0.10 ± 0.35 mA	
t_r	Step response time ¹⁾ to 90 % of I_{PN}	40	μs

General data

T_A	Ambient operating temperature	0 .. + 70	$^\circ\text{C}$
T_S	Ambient storage temperature	- 25 .. + 85	$^\circ\text{C}$
R_p	Resistance of primary winding @ $T_A = 70^\circ\text{C}$	250	Ω
R_s	Resistance of secondary winding @ $T_A = 70^\circ\text{C}$	110	Ω
m	Mass	22	g
	Standards	EN 50178: 1997	
		UL 508: 2010	

Note: ¹⁾ $R_1 = 25 \text{ k}\Omega$ (L/R constant, produced by the resistance and inductance of the primary circuit).

Features

- Closed loop (compensated) current transducer using the Hall effect
- Insulating plastic case recognized according to UL 94-V0.

Principle of use

- For voltage measurements, a current proportional to the measured voltage must be passed through an external resistor R_1 which is selected by the user and installed in series with the primary circuit of the transducer.

Advantages

- Excellent accuracy
- Very good linearity
- Low thermal drift
- Low response time
- High bandwidth
- High immunity to external interference
- Low disturbance in common mode.

Applications

- AC variable speed drives and servo motor drives
- Static converters for DC motor drives
- Battery supplied applications
- Uninterruptible Power Supplies (UPS)
- Power supplies for welding applications.

Application domain

- Industrial.

Voltage Transducer LV 25-P

Insulation coordination

U_d	Rms voltage for AC insulation test, 50 Hz, 1 min	2.5 ¹⁾	kV
\hat{U}_W	Impulse withstand voltage 1.2/50 μ s	16	kV
		Min	
d_{cp}	Creepage distance	19.5	mm
d_{cl}	Clearance	19.5	mm
CTI	Comparative tracking index (group IIIa)	175	

Note: ¹⁾ Between primary and secondary.

Applications examples

According to EN 50178 and IEC 61010-1 standards and following conditions:

- Over voltage category OV 3
- Pollution degree PD2
- Non-uniform field

	EN 50178	IEC 61010-1
$d_{cp}, d_{cl}, \hat{U}_W$	Rated insulation voltage	Nominal voltage
Basic insulation	1600 V	1600 V
Reinforced insulation	800 V	800 V

Safety

This transducer must be used in limited-energy secondary circuits according to IEC 61010-1.



This transducer must be used in electric/electronic equipment with respect to applicable standards and safety requirements in accordance with the manufacturer's operating instructions.



Caution, risk of electrical shock

When operating the transducer, certain parts of the module can carry hazardous voltage (eg. primary busbar, power supply).

Ignoring this warning can lead to injury and/or cause serious damage.

This transducer is a build-in device, whose conducting parts must be inaccessible after installation.

A protective housing or additional shield could be used.

Main supply must be able to be disconnected.

UL 508:Ratings and assumptions of certification

File # E189713 Volume: 2 Section: 1

Standards

- CSA C22.2 NO. 14 - 10 INDUSTRIAL CONTROL EQUIPMENT - Edition 11 - Revision Date 2011/08/01
- UL 508 STANDARD FOR INDUSTRIAL CONTROL EQUIPMENT - Edition 17 - Revision Date 2010/04/15.

Parameter	Symbol	Unit	Value
Primary involved potential		V AC/DC	600
Max surrounding air temperature	T_A	°C	85
Primary current	I_P	mA	0 to 10
Secondary supply voltage	U_C	V DC	± 12 to ±15
Secondary nominal rms current	I_{SN}	mA	25

Conditions of acceptability

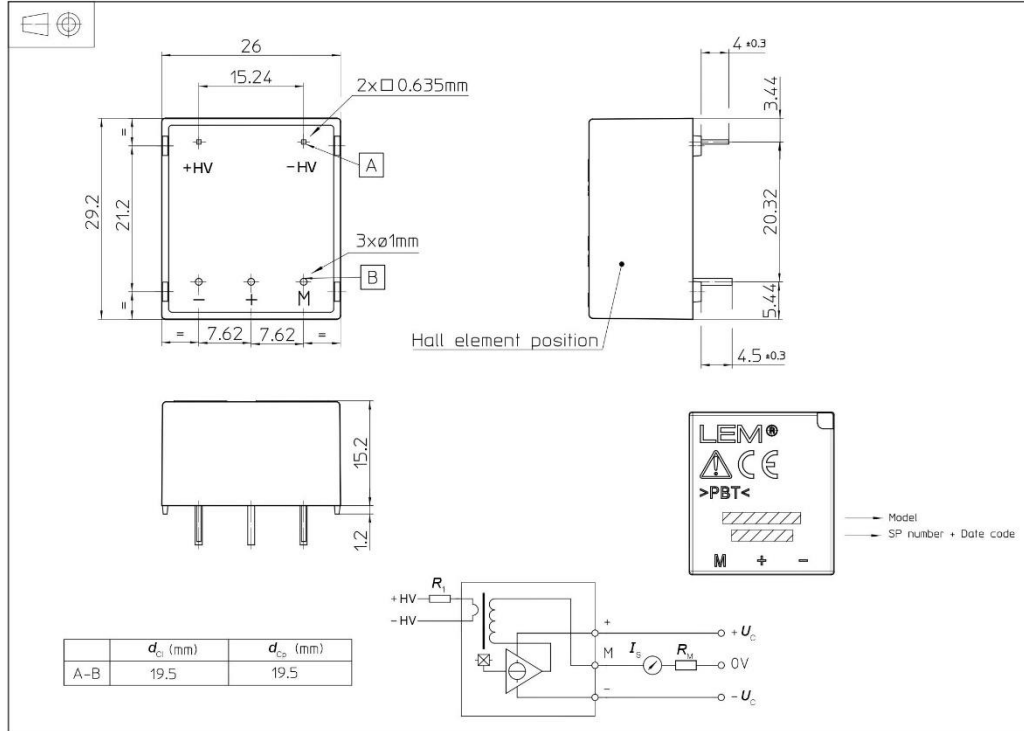
When installed in the end-use equipment, consideration shall be given to the following:

- 1 - *These devices must be mounted in a suitable end-use enclosure.*
- 2 - *The terminals have not been evaluated for field wiring.*
- 3 - *The LV 25-P series are intended to be mounted on the printed wiring board of the end-use equipment (with a minimum CTI of 100).*
- 4 - *The LV 25-P series shall be used in a pollution degree 2 environment when the Printed Wiring Board has not been coated.*
- 5 - *The LV 25-P series shall be mounted on the load side of line filters.*
- 6 - *Low voltage circuits are intended to be powered by a circuit derived from an isolating source (such as a transformer, optical isolator, limiting impedance or electro-mechanical relay) and having no direct connection back to the primary circuit (other than through the grounding means).*
- 7 - *Base on results of temperature tests, in the end use application, a maximum of 100 °C cannot be exceeded at soldering point between primary coil pin and soldering point of on the primary bus bar (corrected to the appropriate evaluated max. surrounding air).*

Marking

Only those products bearing the UL or UR Mark should be considered to be Listed or Recognized and covered under UL's Follow-Up Service. Always look for the Mark on the product.

Dimensions LV 25-P (in mm)



Mechanical characteristics

- General tolerance ± 0.2 mm
- Fastening & connection of primary 2 pins
0.635 x 0.635 mm
- Fastening & connection of secondary 3 pins $\varnothing 1$ mm
- Recommended PCB hole $\varnothing 1.2$ mm

Remarks

- I_s is positive when V_p is applied on terminal + HV.
- Installation of the transducer must be done unless otherwise specified on the datasheet, according to LEM Transducer Generic Mounting Rules. Please refer to LEM document N°ANE120504 available on our Web site: [Products/Product Documentation](#).
- This is a standard model. For different versions (supply voltages, turns ratios, unidirectional measurements...), please contact us.

Instructions for use of the voltage transducer model LV 25-P

Primary resistor R_1 : the transducer's optimum accuracy is obtained at the nominal primary current. As far as possible, R_1 should be calculated so that the nominal voltage to be measured corresponds to a primary current of 10 mA.

Example: Voltage to be measured $V_{PN} = 250$ V

a) $R_1 = 25$ k Ω / 2.5 W, $I_p = 10$ mA Accuracy = ± 0.9 % of V_{PN} (@ $T_A = +25$ °C)

b) $R_1 = 50$ k Ω / 1.25 W, $I_p = 5$ mA Accuracy = ± 1.5 % of V_{PN} (@ $T_A = +25$ °C)

Operating range (recommended): taking into account the resistance of the primary windings (which must remain low compared to R_1 , in order to keep thermal deviation as low as possible) and the insulation, this transducer is suitable for measuring nominal voltages from 10 to 500 V.

APPENDIX G

INDUCTOR DESIGN

We use the Area Product Approach to calculate various parameters of the Inductor.

Step 1: Ascertaining Inductor Value –

Based on the circuit design of the Non-Isolated Boost Converter, the Inductor that we wish to design is of the magnitude 1.3mH.

Step 2: Ascertaining the Magnetic Energy required to be stored in the Inductor-

$$E = \frac{1}{2}LI_m^2,$$

Step 3: Calculating the Area Product to calculate the size of the Core

$$Ap = Ac * Aw = \frac{2E}{K_w K_c J B_m},$$

Utilization Factor K_w , Crest Factor K_c , Current Density J , Flux Density B_m .

Step 4: Calculating the Number of Turns(N) that need to be wound on the Inductor

$$N = \frac{LI_m}{A_c B_m}$$

Step 5: Calculating the Wire Gauge for winding the Inductor

$$a_w = I/J \text{ where } I \text{ is } I_L \text{ (or avg. Input current)}$$

Step 6: Verifying & Cross- Checking the calculations

$$N \cdot a_w < K_w \cdot Aw,$$